# SINGLE-PHOTON DETECTORS FOR CHERENKOV RING IMAGING

by

**Bengt Lund-Jensen**



UPPSALA UNIVERSITY 1988

ACTA UNIVERSITATIS UPSALIENSIS
*Comprehensive Summaries of Uppsala Dissertations from the Faculty of Science*
172

# SINGLE-PHOTON DETECTORS FOR CHERENKOV RING IMAGING

by

**Bengt Lund-Jensen**


UPPSALA 1988

Doctoral dissertation at Uppsala University 1988.

ISBN 91-554-2305-1
ISSN 0282-7468

ABSTRACT

Lund-Jensen, B. 1988. Single-photon Detectors for Cherenkov Ring Imaging. Acta Univ. Ups., Comprehensive Summaries of Uppsala Dissertations from the Faculty of Science 172. 20 pp. Uppsala. ISBN 91-554-2305-1.

Single-photon gaseous detectors have been developed and used for observation of Cherenkov Ring Images. The UV photons of the Cherenkov light ionize molecules of Tri Ethyl Amine or Tetrakis diMethyl Amino Ethylene which are added as a vapour to the hydrocarbon gas of the detector. The photoelectrons produced in the gase move in a uniform electric field towards the anode wires of a multiwire proportional chamber. Each photoelectron gives rise to a shower of electrons which results in an induced fast signal on the wire.

The accelerated electrons near an anode wire excite atomic states in the hydrocarbon gases. Their decay results in the emission of UV photons which ionize the photosensitive vapour generating feedback photoelectrons. The implications of these feedback photoelectrons on the detector resolution and on the maximum attainable gain have been studied.

Optical screens between the anode wires were used to limit the creation of feedback photoelectrons. When operating detectors with optical screens in a magnetic field directed along the anode wire, the electron collection efficiency would be reduced if the electrons were deflected into the screens. This effect has been studied and fully efficient operation demonstrated at magnetic fields up to 1.3 T.

A Ring Imaging Cherenkov counter with this type of photon detection was built and used in an experiment at the CERN proton-antiproton collider where prompt electron production at transverse momenta between 1 to 3 GeV/c was measured.

Bengt Lund-Jensen, Department of Radiation Sciences, Uppsala University, Box 535, S-751 21 Uppsala, Sweden.



Printed in Sweden 1988 by
Reprocentralen, HSC.

One Ring to rule them all, One Ring to find them,
One Ring to bring them all and in the darkness bind them.

(J.R.R. Tolkien, The Lord of the Rings)

*To Gaynor.*

This thesis is based on the following publications:

I. E. Barrelet, T. Ekelöf, B. Lund-Jensen, J. Séguinot, J. Tocqueville, M. Urban and T. Ypsilantis.
A two dimensional, single-photoelectron drift detector for Cherenkov Ring Imaging. Nucl. Instr. Meth. 200 (1982) 219-236.

II. B. Lund-Jensen, T. Ekelöf, A. Hallgren, J. Séguinot, J. Tocqueville, T. Ypsilantis, R. Arnold, J.L. Guyonnet and P. Petroff.
Photosensitive Molecules for Cherenkov Ring Imaging Detectors: Tri Ethyl Amine and Tetrakis diMethyl Amino Ethylene.
TSL-ISV 17 (1988). To be submitted to Nucl. Instr. Meth.

III. L.O. Eek, T. Ekelöf, K. Fransson, A. Hallgren, P. Kostarakis, G. Lenzen, B. Lund-Jensen, J. Séguinot, J. Tocqueville and T. Ypsilantis.
The Time-Projection Ring Imaging Cherenkov (RICH) counter - New experimental results. IEEE Trans. Nucl. Sci. NS-31 (1984) 949-954.

IV. W. Dulinski, L.O. Eek, T. Ekelöf, K. Fransson, A. Hallgren, P. Kostarakis, G. Lenzen, P. Lorenz, B. Lund-Jensen, J. Michalowski and M. Turala.
Operation of RICH single-photon detectors with optically shielded wires in transverse magnetic fields.
Nucl. Instr. Meth. A252 (1986) 418-422.

V. O. Botner, L.O. Eek, T. Ekelöf, K. Fransson, A. Hallgren, P. Kostarakis, G. Lenzen and B. Lund-Jensen.
Preliminary analysis of the performance of a RICH counter for low-$p_T$ electron identification at the CERN $\bar{p}p$ collider.
Nucl. Instr. Meth. A257 (1987) 580-586.

# 1. Introduction.

In a typical high energy physics experiment particles collide at high energies producing a large number of secondary particles covering a whole spectrum of masses and quantum numbers. The more details that are known about the secondary particles the better is our understanding about the interactions in matter, be it strong or electroweak.

With Ring Imaging Cherenkov (RICH) detectors, which have been developed during the last decade, particle velocities are measured. If the momentum of the particles are known from a measurement of the curvatures of their trajectories in a magnetic field, their masses can be determined and the particles are consequently identified.

This thesis concerns the development of RICH counters with drift-type single-photon detectors. The work spans from investigations of the imaging properties of the photon detector (paper I) over the observation of the first Cherenkov ring images obtained with this type of photon detector (paper II), to a RICH counter used for a measurement of prompt electron production at the CERN $S\bar{p}pS$ collider (paper V). Cherenkov light emission and the principles behind some of the commonly used types of Cherenkov counters are described in section 2 together with the design criteria for RICH detectors. A general description of gaseous single photon detectors follows in section 3 where the papers I-IV are summarized and some aspects of the drift-type single-photon detector are described. Finally, a description of a RICH detector used for identification of prompt electrons and a summary of paper V are given in section 4.

# 2. Cherenkov counters.

## 2.1 Cherenkov light.

When a fast moving charged particle passes through a dielectric medium each track element radiates a brief electromagnetic pulse (wavelet). Normally these pulses will interfere destructively; however, when the velocity of the particle is higher than the phase velocity of light in the medium the wavelets produced along the track will for a certain direction be in phase resulting in the emission of light. This electromagnetic shock-wave is analogous to the more familiar shock-wave phenomena such as the bow-wave produced by a speeding boat or the acoustic bang from a supersonic aeroplane. This shock-wave light which was discovered by Cherenkov [1] in 1934, is emitted at a constant angle with respect to the particle trajectory as illustrated in figure 1. During a time interval $\Delta\tau$ the particle travels a distance $AB = \Delta\tau \cdot \beta \cdot c$ where the velocity of the particle is $\beta \cdot c$, c being the velocity of light in vacuum. In the same time interval the light

travels the distance AC = $\Delta\tau\cdot(c/n)$ where n is the refractive index of the medium.

This gives an emission angle $\theta$ :

$$\cos\theta = \frac{1}{\beta n} \qquad (1)$$

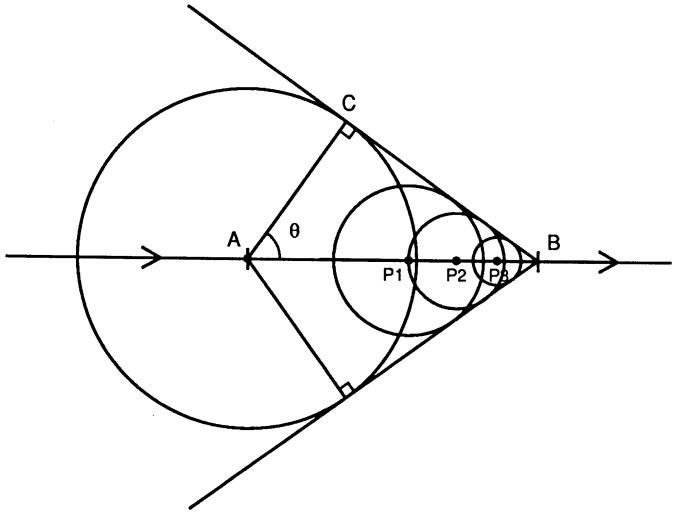


*Figure 1. Huygen's principle illustrating coherence of the wavelets.*

The average number of Cherenkov photons $N_e$ emitted within the photon energy range $E_1$ to $E_2$ in a radiator of length L is given by

$$N_e = L\cdot\left(\frac{Ze}{\hbar c}\right)^2 \int_{E_1}^{E_2}\left(1 - \frac{1}{\beta^2 n(E)^2}\right)dE = L\cdot\left(\frac{Ze}{\hbar c}\right)^2 \int_{E_1}^{E_2} \sin^2\theta(E)\, dE \qquad (3)$$

where Ze is the particle charge.

## 2.2 Threshold Cherenkov counters.

The particle "velocity" $\beta$ must exceed 1/n for the emission of Cherenkov radiation to occur. This is used in the so called threshold Cherenkov counters. At a given momentum, particles with low mass giving Cherenkov light can be separated from heavier particles which have a velocity below threshold for light emission. By using different media (e.g. gases at various pressures) the refractive index can be varied, selecting the threshold to suit the given separation requirements. Threshold Cherenkov counters, where

the presence of light is detected with photomultiplier tubes (PMs), have been used for particle identification since the beginning of the 1950s. A review about Cherenkov light and early threshold counters is found in reference [2].

The cone of Cherenkov light emitted in a radiator of finite length forms an annulaus when projected onto a surface some distance away from the radiator. It is therefore possible to make differential counters where only photons from an annulus of a certain diameter are collected by the PMs. Such a Cherenkov counter was used in the experiment which discovered the antiproton [3]. This detector, shown schematically in figure 2, only gave signals for particles which had velocities in the range $0.75<\beta<0.78$. This kind of projection technique is only practical for dense radiators such as liquids and solids, since they produce a sufficient quantity of light in a short radiator.

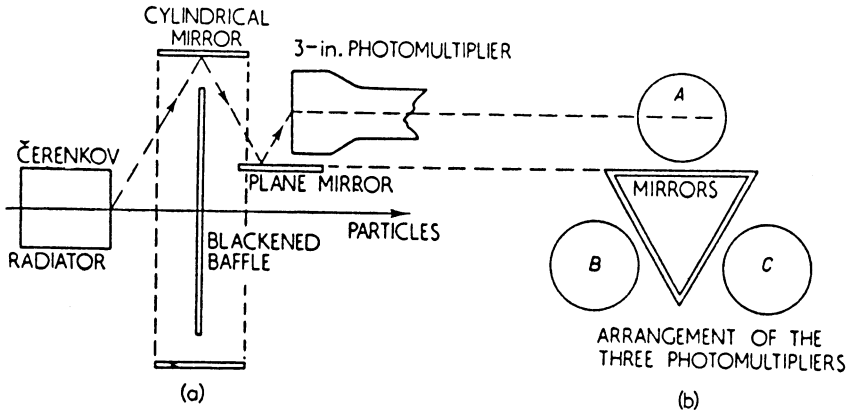


*Figure 2. The differential Cherenkov counter used for the discovery of the antiproton [3].*

If the Cherenkov light emitted at a small angle along the trajectory of a charged particle is reflected by a spherical mirror (radius R), the light is focused into a circular ring image at the mirror focal-surface. In an approximation valid for small angles the radius of the ring image is

$$r = f \cdot \tan\theta \qquad (4)$$

where f is the mirror focal length, f= R/2.

In "differential isochronous self collimating" (DISC) counters an annular diaphragm of radius $r$ located in the focal plane of the mirror is used to obtain the angle determination, as shown in figure 3. The transmitted photons are detected with photomultipliers located behind the diaphragm. Additional optical elements correcting for the chromatic

dispersion are used to improve the resolution. For such counters a resolution $\Delta\beta/\beta \approx 10^{-7}$ can be achieved [4].

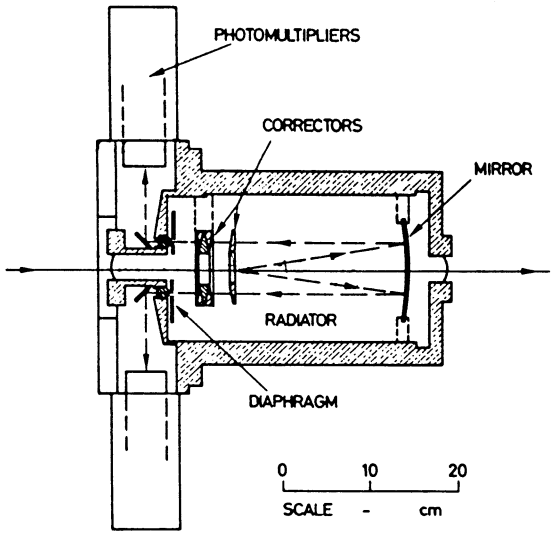


*Figure 3. A gas DISC counter used at the 20-GeV charged hyper beam at CERN [5]. (The figure is taken from Litt and Meunier [4]).*

The differential counters respond to Cherenkov light passing through the annular diaphragm i.e. particles within a preselected velocity range. The small phase-space acceptance make these counters mainly suitable for mass selection in collimated, momentum-analyzed beams.

### 2.3 Cherenkov Ring Imaging.

Séguinot and Ypsilantis [6] suggested making a Ring Imaging Cherenkov (RICH) counter where a photon detector capable of spacial localization of single photons is placed in the focal plane of a spherical mirror. A schematic view of a RICH counter where ring images are obtained both from a thin liquid radiator with the annular projection technique ("proximity" focusing)* and from a gaseous radiator by means of a spherical mirror, is shown in figure 4. Some of the desired properties of the photon detectors are high resolution (typically some $mm^2$), good detection efficiency and a sufficiently low price to make large surface area detectors (10's of $m^2$) feasible. These properties can be obtained with detectors utilizing the photoionization process in gases in combination with charge multiplication due to electron avalanche generation in strong electric fields.

*Although images from a thin liquid radiator were obtained with the proximity focusing method during the work for the present thesis, the observations of these images are not yet published and will not be discussed further in this summary.

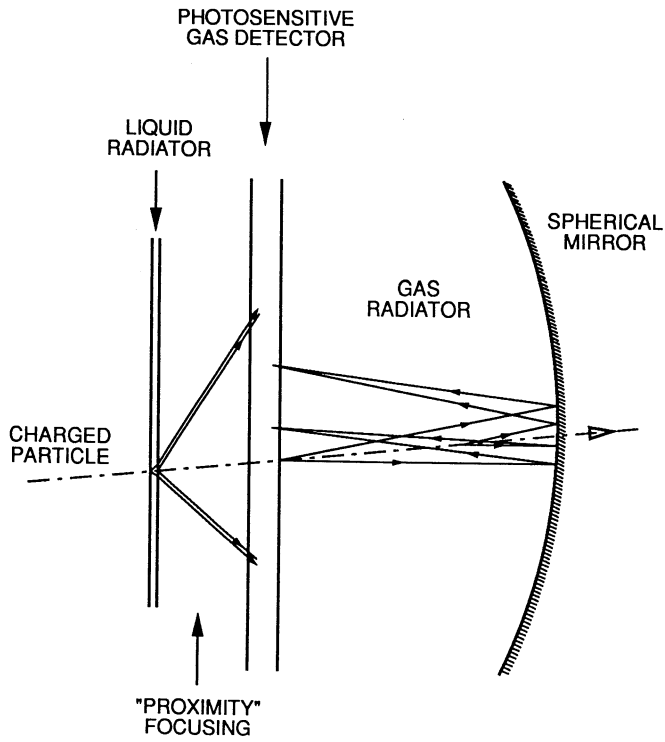


*Figure 4. A schematic view of a RICH counter.*

Using equation 3, the average number of detected photoelectrons ($N_{pe}$) can be written

$$N_{pe} = N_0 \cdot L \cdot \sin^2\theta \qquad (5)$$

where

$$N_0 = \left(\frac{Ze}{\hbar c}\right)^2 \int_{E_1}^{E_2} Q(E) \prod_i \varepsilon_i(E)\, dE \qquad (6)$$

is the merit factor of the photon detector. Q(E) is the photoionization quantum efficiency and $\varepsilon_i(E)$ are the transfer efficiencies of photons and photoelectrons i.e. mirror reflectivity, window and radiator gas transmission and photoelectron detection efficiency. $E_1$ is the lower photon energy limit which is normally given by the photoionization threshold, while the upper limit $E_2$ is generally given by the transmission cut-off.

The relative error in the measurement of the particle Lorentz factor ($\gamma=1/\sqrt{1-\beta^2}$) has been shown [6] to be:

$$\frac{\Delta\gamma}{\gamma} = \frac{\gamma^2 \beta^2 n}{\sqrt{N_0 L}} \Delta\theta \qquad (7)$$

where $\Delta\theta$ is the error in the measurement of the Cherenkov angle. The factors contributing to $\Delta\theta$ are analyzed in reference [7] and will only be summarized here.

The factor ultimately limiting the performance of RICH counters is the error from the chromatic dispersion in the radiator, i.e. the variation of the refractive index with the photon energy which gives

$$\Delta\theta_{chrom} = \frac{dn}{dE}\left(\gamma_t - \frac{1}{\gamma_t}\right)\Delta E \qquad (8)$$

with $\gamma_t$ the Lorentz factor at the threshold for emission of Cherenkov light and $\Delta E$ the root mean square of the energy acceptance distribution A(E):

$$A(E) = \left(1 - \frac{1}{n^2(E)}\right) \cdot Q(E) \prod_i \varepsilon_i(E) \qquad (9)$$

To avoid the Cherenkov angle resolution being limited by the photon detector granularity, the pixel size ($s^2$) should be such that

$$\Delta\theta_{geom} = \frac{s}{\sqrt{12}} \cdot \frac{1}{f} < \Delta\theta_{chrom} \qquad (10)$$

where f is the distance between the mirror and the photon detector (i.e. the mirror focal length). For a detector with a mirror focal length f=1 m and a $C_2F_6$ gaseous radiator ($dn/dE \approx 2.25 \cdot 10^{-5}$ $eV^{-1}$, $\gamma_t=25$), using TMAE (see section 3) as photoionizing agent ($\Delta E=0.5$), equation (3) gives $s < 1$ mm.

For a particle passing at a distance y from the centre of curvature of the mirror the impact parameter is defined as y/R where R is the radius of the mirror. For small Cherenkov angles and for small impact parameters (< 16%) [6] the optical imaging errors are small compared to $\Delta\theta_{chrom}$.

Errors caused by deviations of the particle trajectory in the radiator from a straight line, due to multiple scattering, are small in all the measurements described in this thesis.

# 3. Photon detection in gases.

## 3.1 Photosensitive organic vapours.

It was shown by Séguinot and Ypsilantis [6] that efficient single UV photon detection can be achieved by using organic vapours as gaseous photocathodes. The vapours they used, however, have very high photoionization thresholds, e.g. Benzene ($C_6H_6$) with $E_{tresh}$=9.25 eV, which necessitates the use of expensive windows like $MgF_2$ (transparent below 10.8 eV) or LiF (11.8 eV) to separate the photosensitive gas from the Cherenkov radiator medium. Although the much lower threshold energy for Tri Ethyl Amine (TEA) [8], $E_{thresh}$=7.5 eV allowed a wider choice of window material, single crystal windows such as $CaF_2$ (10 eV) or NaF (9.8eV) were still required. With the introduction of Tetrakis-(di-Methyl Amino)-Ethylene (TMAE) [9,10] a vapour became available which has a sufficiently low photoionization threshold energy ($E_{thresh}$=5.4 eV) to allow the use of quartz windows (transmission below 7.6 eV). Since fused quartz is relatively cheap, this made the construction of large-surface detectors feasible. The quantum efficiencies of TEA and TMAE are shown as functions of photon energy in figure 5 taken from [II]. The transmissions of the quartz and $CaF_2$ windows are also shown, as are the Lorentz factors at threshold for Cherenkov light ($\gamma_t$) for various radiator media and their transmission limits. Both TEA and TMAE have been used in the work for the present thesis.

A disadvantage of TMAE is its low vapour pressure (≈0.35 torr at 20°) which results in a long photon mean free path $l_{ph}$≈30mm at NTP. In order to obtain a shorter $l_{ph}$ heating of the liquid TMAE is required which in turn necessitates a heated detector to prevent condensation of the TMAE. To obtain, for example, $l_{ph}$=15 mm, liquid TMAE at 30 °C with the detector at ~35 °C is required. The detector heating needs to be carefully regulated to avoid variations in the refractive index of the gaseous radiators. Another disadvantage is that TMAE oxidizes violently when exposed to air requiring certain precautions in its handling to be observed. Contrary to TMAE, the mean free path for UV photons in TEA is short (0.6 mm at NTP) [II]. TEA is stable in air but has a different practical disadvantage. Since oxygen has high photoabsorption at the photon energies of the TEA quantum efficiency peak, the $O_2$ content in a typical Cherenkov radiator of 1 meter length needs to be kept below 1 ppm to obtain more than 95 % transmission. A review of the physical properties of TEA and TMAE can be found in [II].

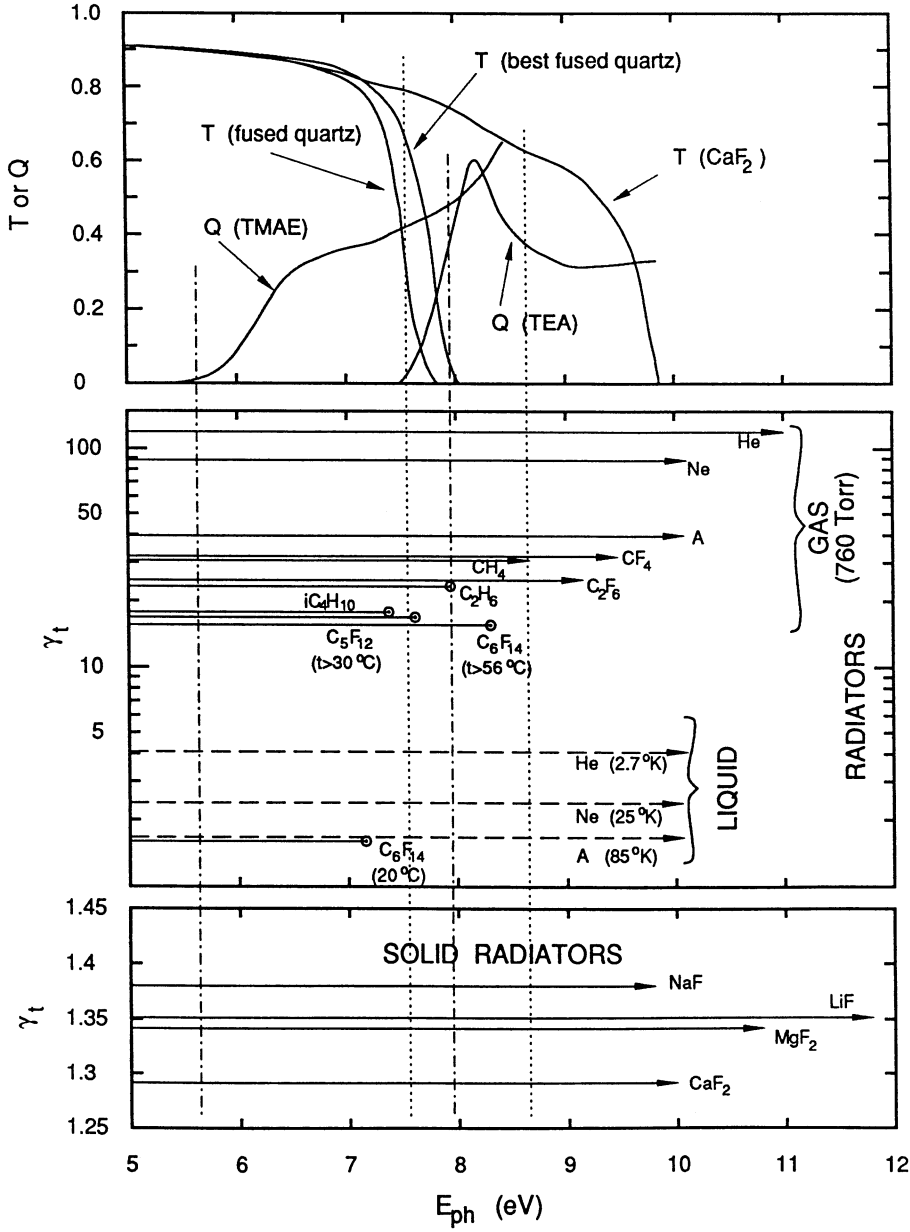


*Figure 5. Quantum efficiencies for TMAE and TEA and window transmissions together with transparency range and Lorentz factor ($\gamma_t$) at the Cherenkov threshold for different radiating media. The medaia that have a sufficiently high transparency limit to be used with TEA are marked with arrows. $\gamma_t$ for the solid radiators are calculated from the refractive index for 8.2 eV energy photons. The dotted lines show the photon energy range for TEA in methane gas, while the dashed lines show the limits for TMAE with fused quartz.*

### 3.2 Gaseous single-photon detectors.

The photon detector consists of a conversion gap, i.e. a volume filled with the photosensitive gas having a thickness of at least $3 \cdot l_{ph}$ in order to obtain >95 % photoabsorption efficiency, coupled to a detector for single photoelectrons. The single-photoelectron detector can be of several types.

In the multiwire proportional chamber (MWPC) shown in figure 6, the gas amplification takes place around thin wires. Typical operational gains are ~$10^5$-$10^6$. The wire address gives one coordinate and a second coordinate can be obtained by, for example, readout of cathode strips or charge division. Since the cathode strips cover more than one wire this method of obtaining a two dimensional coordinate may suffer from reconstruction ambiguities when a large number of signals are recorded. In charge division, the pulse heights at both ends of the resistive anode wire are read out and compared to obtain the second coordinate. For this method to be unambiguous with more than one signal on the same wire, very fast analogue readout is required.

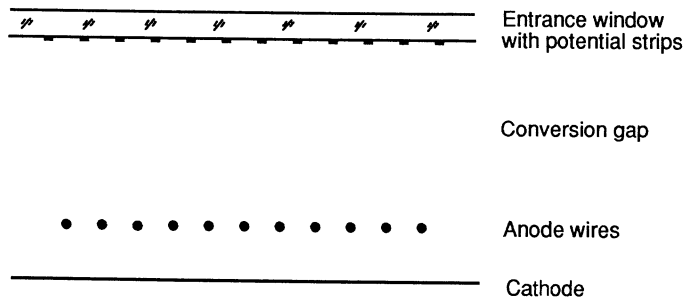


*Figure 6. Schematic view of a multi-wire proportional chamber.*

In the multistep avalanche chamber (MSAC) [11] the amplification takes place in two stages. The principle of this detector is shown in figure 7. The photoelectrons are first drifted into the parallel-plate preamplification gap (PA) with good transfer efficiency since the field in PA is much higher than in the conversion gap C. In the high field, a limited charge multiplication occurs. Part of the avalanche is transferred via the transfer gap (T) into the second stage, for further amplification and detection. The second stage can be a multiwire proportional chamber as previously described. The thickness of the transfer gap has to be several photon absorption lengths for reasons of photon feedback that will be discussed later. This kind of detector has been used in a Fermilab experiment [12]. The second stage of the MSAC can also consist of a spark-chamber [13] or a parallel-plate amplification gap [8]. Optical readout with an image intensifier and a CCD camera has also been tried [14].

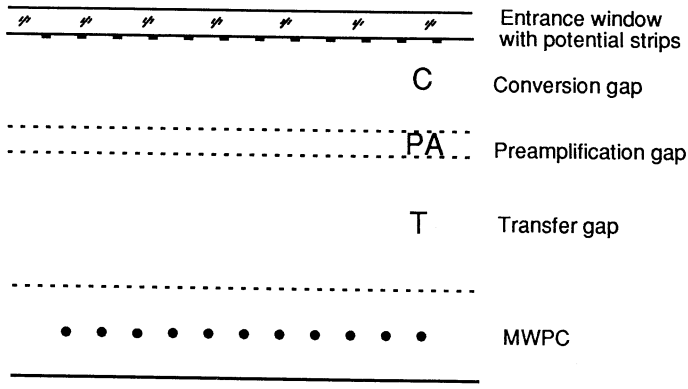


*Figure 7. Schematic view of a multi-step avalanche chamber.*

In the drift-type single-photon detector (figure 8), which is the subject of this thesis, one coordinate of the photon conversion point is given by the wire address in the MWPC. A second coordinate is given by the time spent by the electron to drift to the MWPC wire, using the knowledge of the electron drift velocity in the detector gas. This method is presently preferred for large area RICH detectors e.g. in the DELPHI experiment at LEP [15] and in the SLD at SLAC [16] since it has been demonstrated that electron drift over long distances (~1.5 m) is possible. The drift method gives an ambiguity-free two-dimensional coordinate. The remaining coordinate, i.e. the conversion depth, can be determined either with the charge-division method or by cathode readout. This coordinate is only used to avoid parallax errors from photons converting at different depths. The main disadvantage of the drift-technique is in experiments with very high event rates where two or more events would overlap within the drift time of the detector.

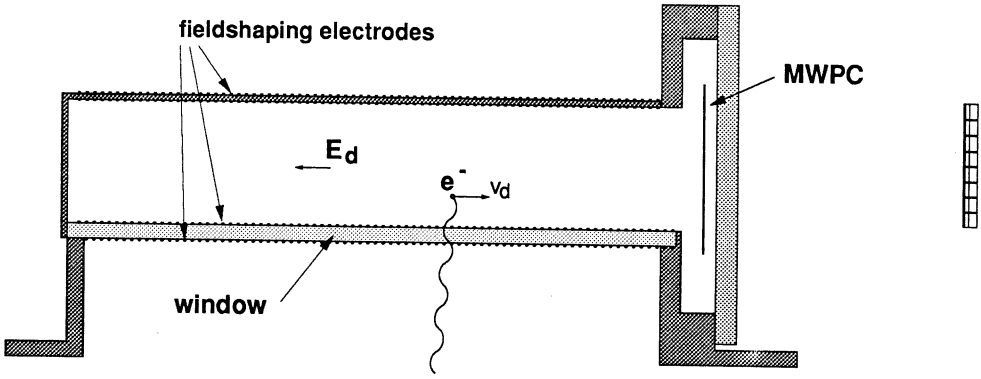


*Figure 8. Principle of the drift-type single-photon detector. The Cherenkov photons enter through the window which separates the photosensitive gas from the Cherenkov radiator medium. Field-shaping electrodes define an electric field parallel to the window. The created photoelectrons drift in this field to a multiwire proportional chamber where they are amplified, detected and timed.*

The drift properties of a conversion gap for a drift-type photon detector is studied in paper [I]. It was found that field shaping electrodes were required on both sides of the window separating the photosensitive gas from the radiator medium, in order to completely polarize the window dielectric with the same electric field as in the drift volume. Otherwise, charge build-up on either side of the window would cause distortions to the drift field.

Measurements of the drift properties were made using the ionization from charged particles traversing the drift volume in a plane parallel to the window. The particle trajectory had a slight slope with respect to the wire-plane of the MWPC in order to prevent the ionization electrons from reaching all wires at the same time. Assuming that the number of primary ionization electrons that are detected on a single wire follow a Poisson distribution with average $N_{pe}$, the probability of having no signal is $P(0)=e^{-N_{pe}}$, hence $N_{pe}= - \ln(P(0))$. The average number of primary electrons thus obtained is shown in figure 9, as a function of drift distance with and without window polarization.

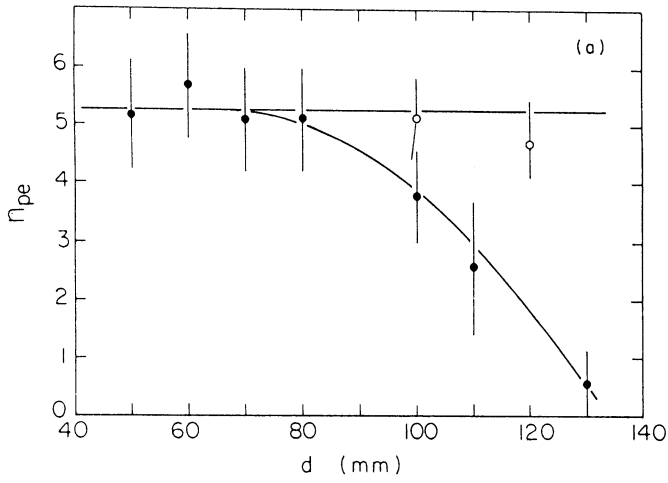


*Figure 9. The average number of primary electrons $n_{pe}$ collected on each wire with the window polarized (open circles) and unpolarized (closed circles) as a function of drift distance d [I].*

Straight lines were fitted to the charged particle tracks. The drift time variance of these tracks, as a function of drift distance, was used to obtain the longitudinal diffusion (in the drift direction). The measured variance had one component which was independent of drift distance. The dominant contribution to this component was drift field inhomogenities between the first field-shaping electrode in the drift volume and the MWPC. In an improved drift cage this error was reduced by a factor 2. A second component, which is due to the randomness of the collisions between the electrons and the molecules of the detector gas, is proportional to the square root of the drift distance. The proportionality constant, the longitudinal diffusion coefficient, was measured to be $\sigma_l$=235 $\mu m/cm^{-1/2}$ for gas mixtures containing predominantly methane.

### 3.3 Feedback photoelectrons.

It has been shown that single photoelectron detection can be achieved with a single-stage multiwire proportional chamber using either methane, ethane, isobutane or mixtures thereof [17].

During the charge multiplication around the anode wires of the MWPC, excitation of atomic states of carbon and hydrogen is caused by the impact of

electrons produced and accelerated near the wire. The de-excitation of the atoms results in emission of UV photons which can ionize the photosensitive vapour, creating feedback photoelectrons at distances described by the photon mean-free-path. The feedback photoelectrons drift back to the same or adjacent wires causing new avalanches. Photons due to the carbon lines at 6.42, 7.48 and 7.94 eV energy can all ionize molecules of TMAE while TEA is only ionized by the 7.94 eV line. The amount of feedback photoelectrons produced has been found to be proportional to the charge developed in the avalanche [17]. Instability sets in at large detector gains where the average number of created feedback photoelectrons per avalanche becomes larger than 1. The implications of feedback photoelectrons on the detector resolution and on the maximum attainable gain are studied in [II] for both TEA and TMAE.

It was found [II] that the MWPC could be operated at ~3 times higher gain with methane - TEA at $l_{ph}$=6 mm (maximum gain $\bar{g}$=1.9·10$^6$) than with methane - TMAE at $l_{ph}$=15 mm ($\bar{g}$=7·10$^5$). Monte-Carlo simulations show a good agreement with the experimental data for both TEA and TMAE over more than one order of magnitude in gain (1.5·10$^5$ - 1.9·10$^6$). The amount of feedback photoelectrons produced ($N_{pfb}$) and detected ($N_{dfb}$) per Cherenkov photoelectron is calculated by Monte-Carlo for the detector in [II], and shown in figure 10 as a function of detector gain. The rise of the number of detected feedback photoelectrons is very sharp for TMAE. To optimize the detector resolution, a detector with TMAE should be operated at as low a gain as possible, still giving an acceptable detection efficiency considering the threshold of the available electronics. With the electronics used for the tests reported in [II] this condition could not be satisfactorily met. For TEA, stable operation at full detection efficiency with sufficiently low background from feedback photoelectrons was possible.

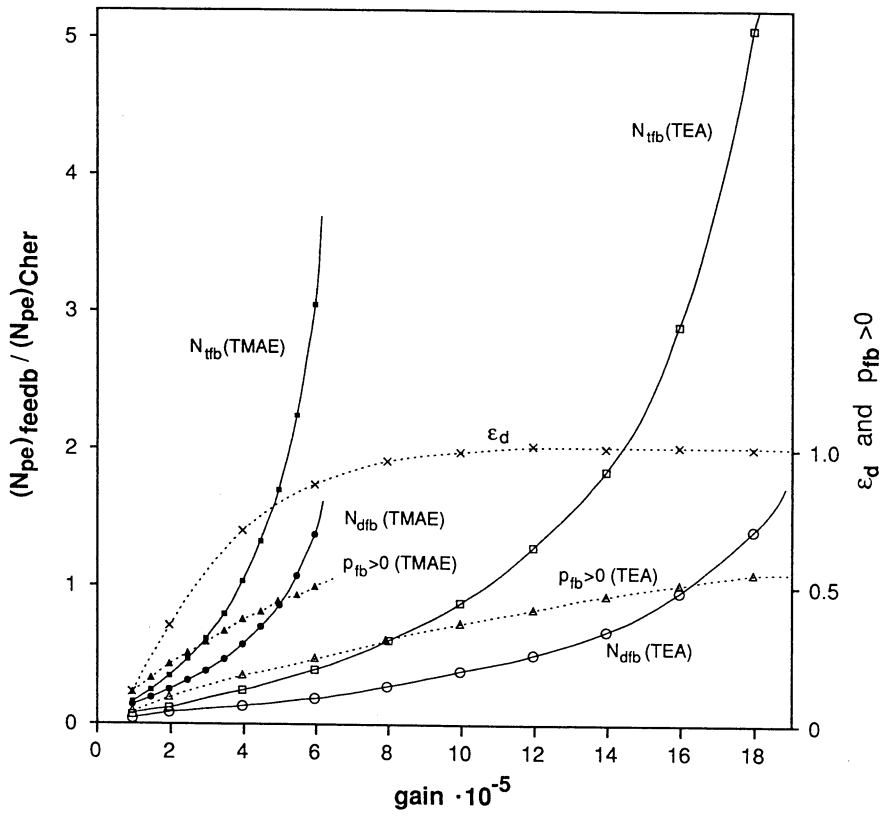


*Figure 10. The number of produced ($N_{pfb}$) and detected ($N_{dfb}$) feedback photoelectrons per Cherenkov photoelectron for TEA and TMAE, estimated by Monte-Carlo simulations, as function of the detector gain. The probabilities of having at least one feedback photoelectron ($p_{fb}$) and the detection efficiency are also shown.*

To limit the creation of feedback photoelectrons, optical screens can be placed between the anode wires as shown in figure 11. The screens are made of printed circuit-board or Kapton® foil with fieldshaping electrodes. The voltages on the electrodes are selected such as to avoid electrons drifting into the screens [III]. The screens are necessesary when charged particles traverse the photosensitive volume since the several hundreds of ionization electrons would otherwise create a large feedback background on adjacent wires. Such background interferes with the ring image and degrades the Cherenkov angle resolution.

® Kapton is a registered trade mark of DuPont deNemour.

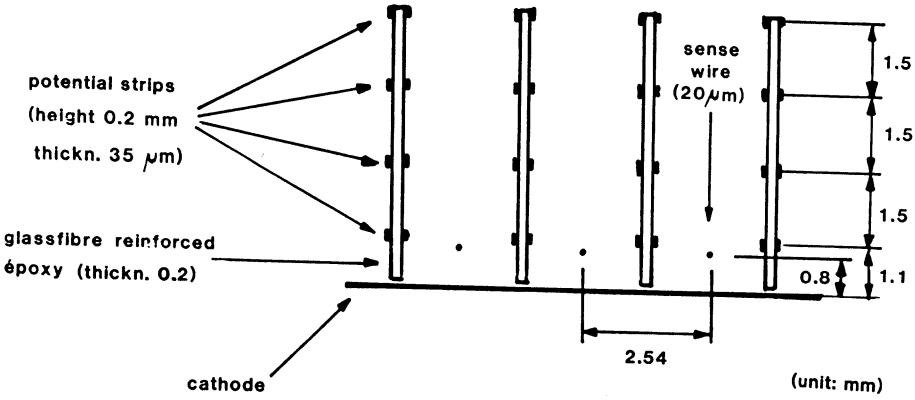


*Figure 11. Cell layout for a MWPC with optical screens made of PC-boards.*

The optical screens may, however, cause problems when the MWPC detectors are used in high magnetic fields directed parallel to the anode wires, e.g. for the Forward RICH in the DELPHI detector at LEP [16]. In such magnetic fields, photo-electrons can be lost by drifting into the screens. This effect was studied [IV] with a photon detector placed inside a magnet. Single photoelectrons were created with a hydrogen flash lamp shining through a mask with 1 mm diameter holes. The measurements were made using ethane, isobutane and a mixture thereof with a small addition of TMAE vapour. For the MWPC with printed-circuit board screens that is schematically shown in figure 11, full detection efficiency was maintained in transverse magnetic fields of up to 1.3 T.

## 4. The UA2 RICH experiment.

A RICH counter was used to measure the prompt electron production at the CERN $S\bar{p}pS$ ($\sqrt{s}$= 630 GeV) in the $p_T$ region 1-3 GeV/c in an experiment together with the UA2 collaboration [V]. The measurement determines the electron to pion ($e/\pi$) ratio which judging from measurements at the ISR ($\sqrt{s}$~60 GeV), could be as low as ~$10^{-4}$. For such $e/\pi$ ratios it is essential that pions are not misidentified as electrons. The main part of the required $\pi$ - e separation has to come from the RICH as other available elements of the UA2 detector have a more limited $\pi$ rejection. The experiment was carried out in 1984-1985. The physics analysis is in progress and the first results are about to be published.

### 4.1 The UA2-RICH.

The radiator vessel, which was filled with gaseous freon ($C_2F_6$) at atmospheric pressure, was tailored to fit into a section of the UA2 endcap. The Cherenkov light was focused into ring images in the photon detector by a 60 cm focal length spherical mirror.

The 20 x 20 $cm^2$ entrance window of the photon detector was made of 5 mm thick $CaF_2$. The 4 cm deep photosensitive gas volume was filled with methane with an admixture of TMAE, resulting in a photon mean free path of 12 mm. The photoelectrons drifted parallel to the window in an electric field of 0.5 kV/cm, with a speed of 9.5 cm/$\mu$s, to the MWPC.

The MPWC is shown schematically in figure 12. It has 80, 20$\mu$m diameter, anode wires with 2.54 mm spacing, directed perpendicular to the window. The stainless steel cathode has a tubular structure cut out by electro-erosion. The photoelectrons enter through a 0.5 mm wide slit, guided by potential wires on both sides of the slit. The cathode is divided into eight 5mm wide bars providing for readout of the conversion depth coordinate. The two other coordinates are obtained from the anode wire address and the drift time.

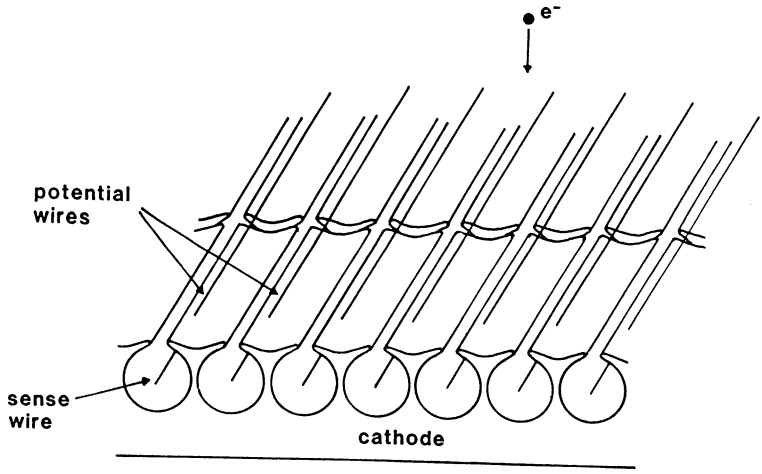


*Figure 12. Schematic view of the MWPC.*

On average 4.5 photoelectrons were detected for a ring from a $\beta=1$ particle with a corresponding ring image radius of 24 mm. This gives a merit factor $N_0=47$ cm$^{-1}$ in agreement with Monte-Carlo simulations. The radius resolution is estimated from the width of the radius distribution to be $\sigma = 1.3$ mm.

The $\pi$ rejection power was measured in a high statistics run with a $\pi^-$ beam at the CERN PS . Two 4 meter long threshold Cherenkov counters placed in front of the RICH detector were used to identify electrons. The probability that an incoming electron was misidentified as a pion (i.e. absence of signal in both threshold counters) was less than $2{\cdot}10^{-7}$. Muons were tagged in a large veto scintillator down-stream from the RICH behind ~3 absorption lengths of iron. The measured probabilty of misidentifying a pion as an electron is shown as a function of beam momentum in figure 13. The rejection becomes rapidly worse for momenta above the $\pi$ threshold. The electron identification efficiency was found to be ~60% independent of momentum.

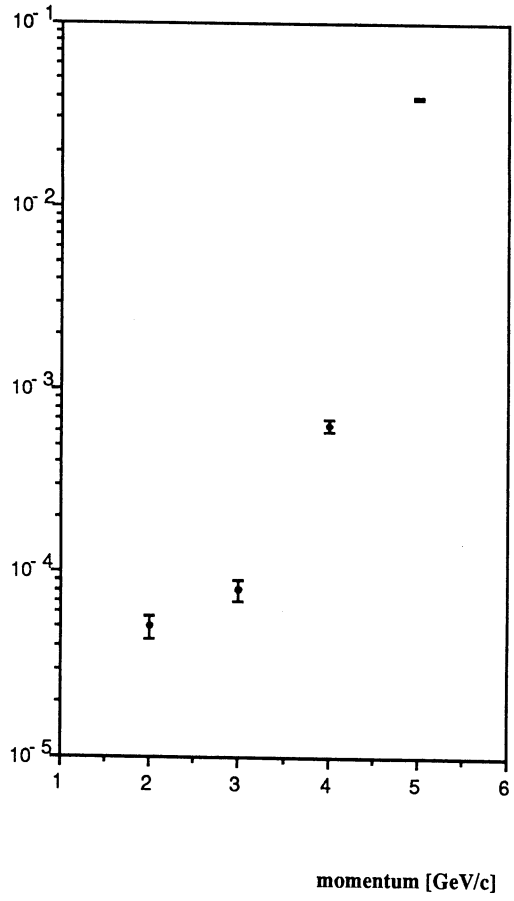


*Figure 13. The measured probability of misidentifying a pion as an electron, as a function of beam momentum.*

## Conclusions.

The RICH technique has gradually became an accepted tool in high energy physics experiments. During the work for the present thesis it was demonstrated that a RICH detector can be operated succesfully in a collider environment. The developments for future high luminosity machines are underway.

## Acknowledgements.

I would like to take the opportunity to express my thanks to all the people who have helped to make this thesis possible.

Special thanks must be given to dr Jacques Séguinot and professor Thomas Ypsilantis who inspired my intrest in high energy physics by their willingness to share their skill and experience with me. Also to dr Allan Hallgren, dr Olga Botner and doc Tord Ekelöf for their invaluable advice and patient guidance. Special thanks also to professor Sven Kullander.

I would also like to thank my fellow students Lars-Owe Eek and Kjell Fransson for fruitful collaboration and lots of fun.

The work done by the institute workshop has been very important for this thesis and I am very grateful for the help I recieved.

Finally I would like to thank all the people at the Department of Radiation Science in Uppsala (ISV) for the productive and friendly atmosphere.

## References.

[1] P.A. Cherenkov, 1934. Dokl. Akad. Nauk SSSR 2:451.

[2] J.V. Jelley. Cherenkov Radiation and its Applications. Pergamon Press, London.

[3] O. Chamberlain, E. Segrè, C. Wiegand and T. Ypsilantis. Phys Rev 100 (1955) 947.

[4] J. Litt and R. Meunier. Ann. Rev. Nucl. Sci. 23 (1973) 1

[5] J. Badier, R. Bland, J.C. Chollet, T. Devlin, J.-M. Gaillard, J. LeFrancios, B. Merkel, R. Meunier, J.-P. Repillin, G. Sauvage and R. Vanderhaghen Phys. Lett. B 39 (1972) 414.

[6] J. Séguinot and T. Ypsilantis. NIN 142 (1977) 377.

[7] T. Ypsilantis. Physica Scripta 23 (1981) 371.

[8] G. Charpak, S. Majewski, G. Melchart, F. Sauli and T. Ypsilantis. NIM 164 (1977) 419.

[9] B. Cetinkaya, G. H. King, S. S. Krishnamurthy, M. F. Lappert and J. B. Pedley. Chem. Comm. (1971) 1370.

Y. Nakato, M. Ozaki, A. Egawa and H. Tsubomura. Chem. Physics Letters 9 (1971) 615.

Y. Nakato, M. Ozaki and H. Tsubomura. Bull. Chem. Soc. Japan 45 (1972) 1299.

Y. Nakato, T. Chiyoda and H. Tsubomura. Bull. Chem. Soc. Japan 47 (1974) 3001.

[10] D.E. Anderson. NIM 178 (1980) 125 and IEEE Trans. Nucl. Sci. NS-28 (1981) 842.

[11] G. Charpak and F. Sauli. Phys. Lett. 78B (1978) 523.

[12] G. Coutrakon, M. Cribier, J.R. Hubbard, Ph. Mangeot, J. Mullie, J. Tichit, R. Bouclier, A. Breskin, G. Charpak, J. Million, A. Peisert, J.C. Santiard, F. Sauli, C.N. Brown, D. Finley, H. Glass, J. Kirz and R.L. McCarthy. IEEE Trans. Nucl. Sci NS-29 (1982) 323.

[13] P. Fisher, A. Drees, P. Glässel, G. Lamade, H. Ries, H. Specht, A. Breskin, R. Chechik, Z. Fraenkel, D. Sauvage, V. Steiner, I. Tserruya and R. Horrisberger. IEEE trans. Nuc. Sci. NS-35 (1988) 432.

[14] A. Breskin, R. Chechik, Z. Fraenkel, D. Sauvage, V. Steiner, I. Tserruya, G. Charpak, W. Dominik, J.P. Fabre, J. Gaudean, F. Sauli, M. Suzuki, P. Fisher, P. Glässel, H. Ries, A. Schön and H.J. Specht. "A highly efficient low-pressure UV-RICH detector with optical avalanche recording". Presented at the London conf. on Position Sensitive Detectors Sept. 1987. NIM in press.

[15] Delphi Technical Proposal. Delphi 83-66, CERN, May 1983.

[16] SLD Design Report, SLAC report 274 (1984).

[17] T. Ekelöf, J. Séguinot, J. Tocqueville and T. Ypsilantis. Physica Scripta 23 (1981) 718.

[18] R. Arnold, P. Baillon, H.J. Besch, M. Bosteels, E. Christophel, M. Dracos, Y. Giomataris, J.L. Guyonnet, G. Passardi, P. Pétroff, J. Séguinot, D. Toet, J. Tocqueville and T. Ypsilantis. NIM A270 (1988) 255.

ACTA UNIVERSITATIS UPSALIENSIS
*Comprehensive Summaries of Uppsala Dissertations from the Faculty of Science*
Editor: The Dean of the Faculty of Science

A doctoral dissertation from the Faculty of Science, Uppsala University, is usually a summary of a number of papers. A few copies of the complete dissertation are kept at major Swedish research libraries, while the summary alone is distributed internationally through the series *Comprehensive Summaries of Uppsala Dissertations from the Faculty of Science.* (Prior to July, 1985, the series was published under the title "Abstracts of Uppsala Dissertations from the Faculty of Science".)

Distributor:
Almqvist & Wiksell International
Stockholm — Sweden

UPPSALA UNIVERSITET
REPROC. HSC 1988

ISBN 91-554-2305-1
ISSN 0282-7468

Nuclear Instruments and Methods 200 (1982) 219–236
North-Holland Publishing Company



# A TWO-DIMENSIONAL, SINGLE-PHOTOELECTRON DRIFT DETECTOR FOR CHERENKOV RING IMAGING

E. BARRELET [1], T. EKELÖF [2], B. LUND-JENSEN [3], J. SÉGUINOT [1], J. TOCQUEVILLE [4], M. URBAN [1] and T. YPSILANTIS [1]

[1] *Ecole Polytechnique, Palaiseau, France*
[2] *CERN, Geneva, Switzerland*
[3] *Univerity of Uppsala, Uppsala, Sweden*
[4] *Collège de France, Paris, France*

Received 3 February 1982

A detector capable of imaging single photoelectrons has been constructed and tested. UV photons ($\geq 5.4$ eV) are converted to electrons with high quantum efficiency by photoionization of a small admixture ($\sim 1$ Torr) of an organic vapour TMAE in a predominantly methane drift and amplifying gas at atmospheric pressure. The produced photoelectrons drift in a uniform applied electric field to a picket fence of proportional wires where each electron is amplified, counted and timed. The two-dimensional source point of each photoelectron is uniquely determined by the hit wire address and the arrival time.

The detector has been tested by measuring ionization electrons produced in the drift gas be relativistic charged particles. The limiting precision to which the electron source point can be determined has been measured to be 300 $\mu$m (r.m.s.) in the drift direction and 370 $\mu$m in the wire plane direction. Additional independent error sources due to electron diffusion in the drift gas have been measured to be proportional to the square root of the drift distance with a proportionality constant of 235 $\mu m/cm^{1/2}$ in both directions. Drift velocities of electrons in various predominantly methane gas mixtures have been measured as a function of the applied electric field.

The utilization of such a two-dimensional single electron drift detector for Cherenkov ring imaging is presented with a discussion of the advantages and limitations of the drift method for imaging.

## 1. Introduction

The Cherenkov light emitted by a high-energy particle traversing a dielectric medium may be focused to a ring image with the aid of a spherical mirror. The focus of the image is situated half-way between the mirror and its centre of curvature. The focal surface thus has the shape of a spherical shell with a radius half of that of the mirror, as illustrated in fig. 1.

The measurement of the radius of the Cherenkov ring allows a determination of the angle of emission of the Cherenkov light and thus of the particle velocity. If the particle momentum is also measured, this enables a determination of the mass of the particle and thereby its identity. A detailed analysis of the ring image optical quality and the concomitant resolution obtainable may be found elsewhere [1].

The basic technical problem in the utilization of this method is the detection of the position of single ultraviolet (UV) photons in the focal surface with good two-dimensional position resolution ($\sim 1$ mm), high conversion ($\sim 50\%$) and counting efficiency ($\sim 90\%$). The conversion of photons to electrons is effected via the photoionization mechanism

$$h\nu + M \rightarrow M^+ + e^- , \qquad (1)$$

where $M$ is a suitable photosensitive molecule admixed with the detector gas. This process has been shown [2] to have a large quantum efficiency ($\sim 50\%$) for photons above the threshold energy $E_t$ which is, for the molecules so far utilized, well into the UV region of the electromagnetic spectrum (i.e. $E_t \geq 5.4$ eV). High single-electron counting efficiency ($\geq 90\%$) has been achieved [3] by using pure methane ($CH_4$) as an amplifying gas in a multiwire proportional chamber (MWPC) geometry. As shown in fig. 2, we achieve unique two-dimensional determination of the photon conversion point by the use of a drift gap in which the photons are converted and drift to a MWPC array where they are detected and timed [3]. In an experimental situation where several radiating particles are expected to emerge together in collimated jets, it is essential that the many near-by photon points in the focal surface can be reconstructed unambiguously in order to allow the pattern recognition of the circular images.

We have constructed a photon drift detector (type: time projection chamber), in accordance with the above criteria, which has a circular transmitting window of

0167-5087/82/0000–0000/$02.75 

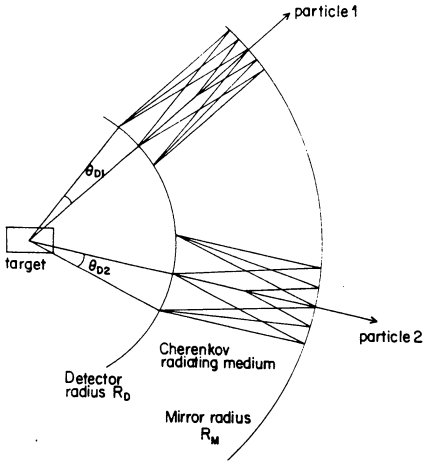


Fig. 1. Schematic diagram of ring-imaging geometry. The outer spherical surface is a mirror and the inner surface a detector. Photons emitted when two particles emerge from the interaction region, near the mirror centre of curvature, will be focused by the mirror into two separate rings with half-angles $\theta_{D1}$ and $\theta_{D2}$. These ring radii are related to the particle velocity $\beta_i$ by the relation $\theta_{D_i} = \cos^{-1}(1/n\beta_i)$ where $n$ is the refractive index of the gas (or liquid) radiating medium.

127 mm diameter (open diameter 100 mm) sitting above a square drift gap of $140 \times 140$ mm$^2$ in area and 15 mm (or 45 mm) in depth. In this paper we describe the construction of the photon detector and the results of test measurements, performed in a 5–20 GeV/$c$ $\pi^-$ beam from the CERN Proton Synchrotron (PS), to detect the ionization electrons produced in the drift gap by through-going beam tracks. The parameters which affect the precision of spatial localization of the electrons, such as wire spacing, time binning, drift velocity, and diffusion, have been investigated. In addition, an unexpected non-uniformity in the drift field, due to incomplete polarization of the entrance window, has been observed and corrected. In a forthcoming paper we describe the ring images obtained with this detector, with triethylamine (TEA) and tetrakis (dimethylamine) ethylene (TMAE) as the photoionizing gases.

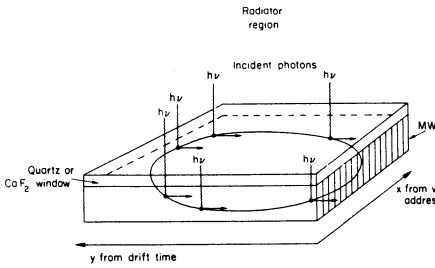


Fig. 2. Schematic of the photon drift detector. The UV photons produced by a charged particle in the radiator are reflected by a spherical mirror and form a ring image, in the focal plane of the mirror, just below the entrance window (quartz or $CaF_2$). The photons are converted to photoelectrons by photoionization of molecules in the drift volume. A uniform electric field parallel to the entrance window and perpendicular to the MWPC plane causes the electrons to drift to the MWPC plane where they are amplified, counted and timed. The carrier drift gas is methane plus TEA or TMAE.

One of the aims of the present work is to explore the possibility of using this drift technique for UV photon ring-imaging over large, spherically shaped, detector areas (several m$^2$), as would be needed for ring-imaging Cherenkov (RICH) counters made to cover large solid angles (several steradians). On the bases of the experience gained with the photon drift detector discussed in this paper, we have designed and constructed a large modular counter unit having a large ratio of active to total area ($\sim 85\%$) and small matter density ($\sim 2$ g/cm$^2$). Several such units can be mounted side by side at a slight angle to cover a large, approximately spherical surface.

## 2. Principle of the single-photoelectron drift detector

The basic idea of the drift detector is illustrated in fig. 2. Photons generated in the Cherenkov radiator enter the photosensitive drift region of the detector through a transparent window and converge to a ring image on the focal surface situated just behind this window. The drift region is filled with a suitable drift chamber gas such as methane, with a small admixture of a photoionizing vapour such as TEA or TMAE. These molecules may absorb a photon of energy $E$ and produce a single photoelectron with probability $Q(E)$, i.e. the quantum efficiency for the process. The probability $Q(E)$ is null if $E < E_t$ with $E_t = 7.5$ eV for TEA and $E_t = 5.4$ eV for TMAE. The electron thus produced drifts in a uniform electric field, parallel to the window, into a MWPC plane where, after amplification in the intense electric field around a wire, the time of arrival (relative to an external trigger) of each electron is measured on the wire which it hits. The two coordinates $(x,y)$ of the conversion point in the focal surface can thus be obtained for each detected photon, without ambiguity, from the measured drift time $t$ ($y = v_D t$, where $v_D$ is the electron drift velocity) and the corresponding wire address ($x$). Fig. 3 shows the photon detector in two projections (side and top). The field-shaping electrodes are indicated by black dots and full lines, with the direction of the uniform electric field also indicated. A double entrance window is shown with

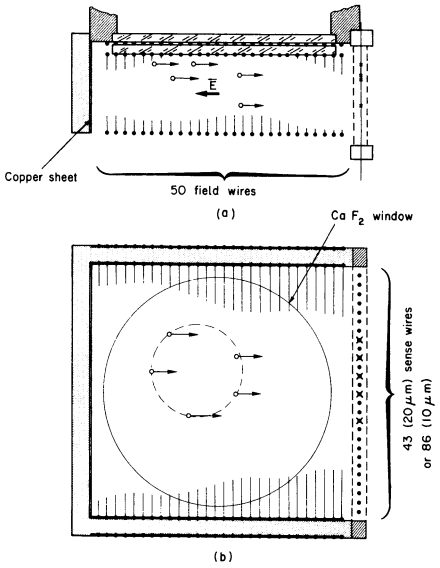


Fig. 3. A schematic side view (a) and top view (b) of the photon drift detector. A double entrance window is shown with field-shaping electrodes (full dots and lines) on both sides of the inner window as explained in section 3.3. Photons coming through the entrance windows are converted in the drift volume at points represented by open dots and drift in the uniform electric field $\boldsymbol{E}$ to the MWPC plane, where the impact points are shown by crosses. The cathodes of the MWPC are also shown (dotted lines). The large full circle in (b) shows the extent of the circular entrance window relative to the larger square drift volume. In a later design (Mark II) the entrance window is square (or rectangular) and covers the full drift volume.

field-shaping electrodes mounted on both sides of the inner window. The reason for this double window will be discussed in section 3. Also shown in fig. 3 are open dots corresponding to photon conversion points in the drift volume, and the direction of drift of these electrons towards the MWPC plane where the corresponding impact points are indicated by crosses. The depth of the conversion point in the detector depends on the photon mean free path for absorption in the detector gas. Typically, this absorption mean free path was 5 mm for TEA and 15 mm for TMAE; thus the drift gap depths were 15 mm and 45 mm, respectively, so as to ensure essentially complete (95%) photon absorption. Fig. 4 shows a cross-section of the mechanical construction of the detector and shows its mounting relative to the Cherenkov radiator gas volume.

### 2.1. The photosensitive drift region

The parallel electric field in the drift region is defined by wires stretched between the two legs of a U-shaped Stesalite frame as illustrated in fig. 5. There are two layers of 50 equidistant wires, each of 140 mm length and 100 $\mu$m diameter, mounted with a pitch of 2.54 mm. The wires are interconnected through 1 M$\Omega$ resistors (tolerance 1%) in a voltage divider chain, as shown in fig. 6. The photoelectrons drift in the space between the legs and the wire planes towards the open side of the U-frame where the MWPC is placed. The thickness of the frame, which determines the depth of the photoabsorption region, was either 15 mm or 45 mm, depending on the absorption length of the photo-ionizing agent used (TEA or TMAE).

The connection between opposite equipotential wires, one in each wire plane, is made through parallel conductive lines deposited on a 100 $\mu$m thick Kapton foil using the printed-circuit technique. These foils are wrapped around the legs of the U-frame, thus making contact between the wire planes, on both the inside and the outside of each leg. This was done in order to avoid having a part of the surface of the U-frame where the

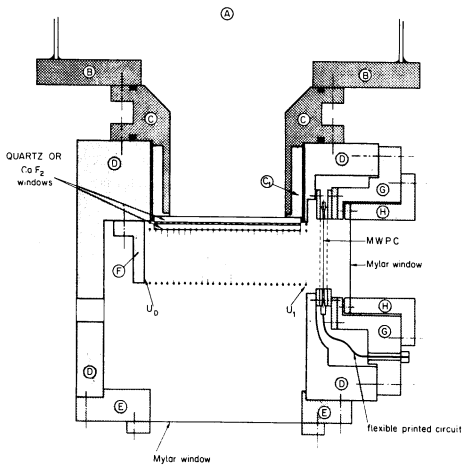


Fig. 4. Details of the photon drift detector: A – gas radiator volume; B – end flange of gas container (stainless steel); C – extension of gas container (stainless steel) in contact with radiator gas; $C_1$ – araldite extension (glued to C) onto which the outer entrance window is glued; D – support box (araldite) for drift gap and MWPC; E – rear closure for support box with Mylar window; F – drift volume with field-shaping electrodes and inner entrance window. Potential applied at the far side in $U_D$ and the near side to the MWPC in $U_1$; G – MWPC array with wire mesh cathodes and wire anodes; H – closure of MWPC array with Mylar window.

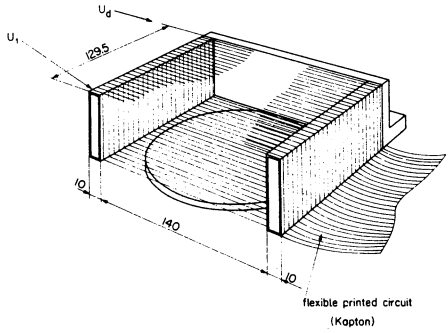


Fig. 5. View of the drift gap (F in fig. 4) with field-shaping electrode wires and Kapton printed-circuit channels covering the U arms. Also shown is the inner entrance window which abuts on the entrance field-shaping electrode wires. Not shown is a second plane of field-shaping wire electrodes which sandwich the inner entrance window.

potential would be undefined and where accumulation of electric charge leads to a transverse polarization of the frame material which gives rise to distortions of the electric field. This problem will be discussed in detail in a subsequent section (section 3).

The U-frame is mounted with one of its wire planes touching one of the entrance windows that are placed between the radiator gas volume and the detector gas volume. In order to have the same electric field on both sides of this window, a second field-shaping electrode wire plane is used on the outside of the window, as shown in fig. 3. As a high-voltage connection is needed between corresponding wires on either side of the window, it was technically a problem to have this window also providing the gas-tight separation needed between the detector gas and the radiator gas. Although a solution to this technical problem of using only one window exists (Mark II), we have first used the simple method of adding a second window outside the first one. This outer window is glued with Araldite onto an extension tube ($C_1$ in fig. 4) mounted on the radiator gas container so as to ensure gas tightness between detector and radiator gases. An obvious disadvantage of this solution is that, because of the limited transmission of the windows in the UV, the second window reduces somewhat the overall photon detection efficiency. In fig. 7 is shown the transmission of 5 mm thick fused quartz (Corning 7940) and calcium fluoride (Harshaw) entrance windows measured in the laboratory with a UV monochromator. We note that at the peak of TEA photoionization response (8.2 eV) the $CaF_2$ crystal has 68% transparency, whereas at the centre of TMAE response with fused quartz (6.7 eV) the quartz has 83% transparency. An advantage of this solution, at this

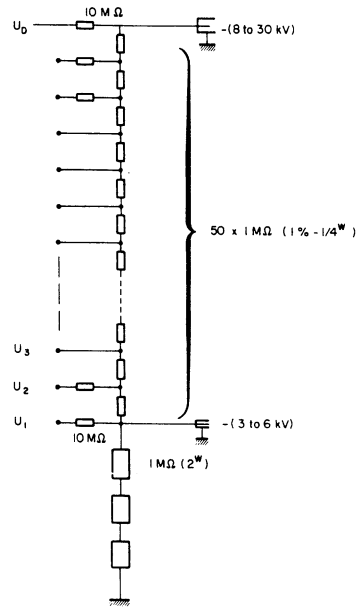


Fig. 6. Voltage resistor chain for field-shaping electrodes. The negative potentials $U_D$ and $U_1$ are defined by external supplies. The black dots correspond to the wires of the field-shaping electrodes.

stage of experimentation, is that of flexibility. For example, we were able to vary the domain of spectral transmission of the detector by changing the inner window from $CaF_2$ to quartz when the photoionizing molecule was changed from TEA to TMAE. This provisional solution furthermore avoided the problem of

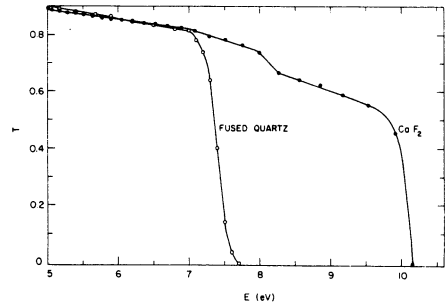


Fig. 7. The photon transmission vs photon energy of fused quartz (Corning 7940) and a $CaF_2$ (Harshaw) single crystal windows. Both windows are 5 mm thick and 127 mm in diameter.

field-shaping electrode wire planes in the argon radiator gas, which would cause a glow discharge when the electric field exceeds 1 kV/cm.

The detector volume is closed, on the side away from the entrance window, by a Mylar foil (see E in fig. 4). This foil is far enough away (7cm) from the drift volume to cause a negligible influence on field uniformity in the gap. The third side of the U-frame is covered with a copper sheet, which is connected to the potential $U_D$ defining the high-voltage end of the drift field. The U-frame is mounted inside the Araldite support box (see D in fig. 4). This support box contains the gas inlets and outlets, the high-voltage connections, the voltage division resistor chain, and the MWPC array (see G in fig. 4). The support box itself is mounted on an extension tube (see C in fig. 4) of the Cherenkov gas radiator.

### 2.2. The multiwire proportional chamber

The MWPC detects the lateral positions and the arrival times of the photoelectrons as they drift to the end of the electric field volume and into the MWPC array. Two different chambers were used, one having 43 anode wires of 20 $\mu$m diameter mounted with a pitch of 2.54 mm, the other having 86 anode wires of 10 $\mu$m diameter with a pitch of 1.27 mm. In both cases the wires are made of gold-plated tungsten, and the wire length is 6 cm. The cathode planes, placed 3.2 mm away on either side of the anode, consist of a woven stainless-steel mesh made of 50 $\mu$m wires with 500 $\mu$m spacing.

The MWPC chamber is mounted at position G as shown in fig. 4. In this position the chamber covers the end of the drift region, with the anode wires perpendicular to the entrance window plane and to the direction of the electric field.

The gap between the last wire of the field-shaping electrode ($U_1$) and the MWPC cathode was 14 mm, and it had been foreseen to insert two additional wire-mesh planes into this gap. This would have enabled the detector to be operated with gaseous preamplification [4]. The gap between the first and second additional meshes was to be used to cause a discharge avalanche, and the gap between the second additional mesh and the MWPC cathode as a transfer gap. However, the measurements reported in this paper were made without the preamplification and transfer stages, as sufficient amplification was obtained using methane as the amplifying gas coupled with very sensitive detection electronics. This left, however,a rather large gap (14 mm) between $U_1$ and the cathode of the MWPC, which has repercussions on the time resolution of the detector as will be discussed in section 5.

The MWPC is closed to the outside air by a Mylar foil mounted behind the outside cathode grid (see H in fig. 4). The electric potentials of the closest drift-gap wire ($U_1$) and the MWPC cathode have separate high-voltage leads and can thus be adjusted independently of each other. This allows us to maintain the same electric field in the drift region and in the gap between $U_1$ and the cathode when the MWPC voltage is varied.

### 2.3. The electronics and data-acquisition system

The basic layout of the electronics for the processing of the pulses from the anode wires of the MWPC is shown in fig. 8. The anode pulses are led through a 10 cm long flexible printed circuit-board conductor to the preamplifiers which are mounted outside on the support box. The detector electronics shown in fig. 9 are composed of fast MECL 10000 series amplifiers having a 100 MHz bandwidth. The preamplifiers (voltage gain of 50) are mounted on the detector and are connected to the anode (sense) wires of the MWPC by a flexible Kapton printed circuit, 10 cm in length. Every other channel on this circuit is connected to ground so as to minimize cross-talk between neighbouring wires. The resistance to ground on the sense wire is 1.5 k$\Omega$, with a measured stray capacity of 16 pF and thus an entrance filter time constant of 24 ns. The preamplifiers are protected against sparking in the MWPC by a 270 $\Omega$ resistance in series with two back-biased diodes.

The preamplified analog signals are transferred to the counting area via 20 m lengths of 120 $\Omega$ impedance twisted-pair cable, which reduces the bandwidth to about 80 MHz. In the counting area the analog signals are further amplified (voltage gain 60) by the first two stages of MC 10116 amplifiers (rated gain $12 \times 12$) with feedback, and discriminated in the third stage by a Schmitt trigger which gives 60 dB rejection of positive pulses induced on neighbouring wires. The discriminator has a hysteresis of 200 mV, which aids in noise rejection and allows for adjustment of the voltage threshold level by means of an external dc bias voltage. This threshold is adjustable for between 50 $\mu$V and 5 mV signals on the anode wire. The r.m.s. noise level at the entry to the preamplifier (when not connected to the MWPC wire) is 50 $\mu$V. When operating with the MWPC, this noise gives rise to a random counting rate of $10^2$ Hz per wire when the discriminator level is set for a 150 $\mu$V signal on the wire (i.e. 0.1 $\mu$A on 1.5 k$\Omega$), which for a capacity of 16 pF corresponds to a charge of 2.4 fC or $1.4 \times 10^4$ electrons.

The voltage response of the MWPC and preamplifier entry filter is, for one photoelectron, given by the relation

$$v(t) = \frac{eAC}{C_i} \int_0^t \frac{e^{-\tau/R_iC_i}}{t + t_0 - \tau} d\tau$$

$$= \frac{eAC}{C_i} e^{-(t+t_0)/R_iC_i} \left[ \ln\left( \frac{t+t_0}{t_0} \right) + \frac{t}{R_iC_i} + \frac{(t+t_0)^2 - t_0^2}{4R_i^2C_i^2} + \frac{(t+t_0)^3 - t_0^3}{18R_i^3C_i^3} + \cdots \right] \quad (2)$$

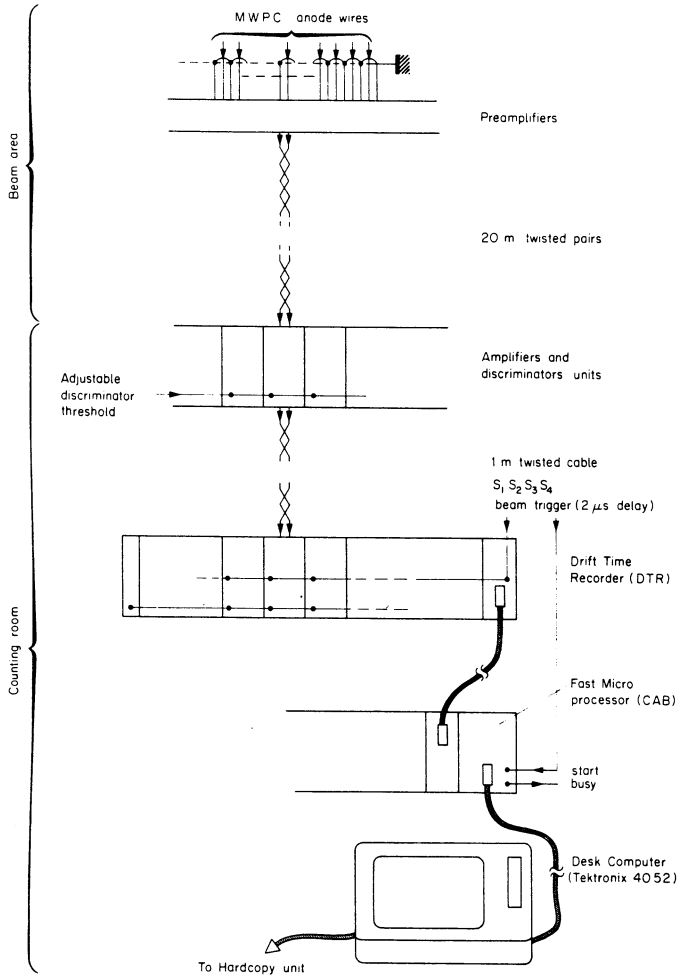


Fig. 8. Schematic diagram of drift detecor read-out.

where $A$ is the MWPC gain, $C = s/2\pi a$ is the capacity of a MWPC wire per unit distance ($s$ is the wire spacing, $a$ the cathode–anode distance), $R_i = 1.5$ kΩ and $C_i = 16$ pF, and $t_0$ is a constant:

$$t_0 = \frac{s^2}{2CV\pi^2\alpha}\ln\left[1+\frac{\pi^2 d^2}{8s^2}\right]$$
$$= \frac{d^2}{16CV\alpha}\left[1-\tfrac{1}{2}\left(\frac{\pi^2 d^2}{8s^2}\right)+\tfrac{1}{3}\left(\frac{\pi^2 d^2}{8s^2}\right)^2-\cdots\right], \quad (3)$$

where $V$ is the cathode–anode potential, $d$ the wire diameter, and $\alpha$ the mobility of the positive ions ($cm^2/V \cdot s$). In the parameters of the detector ($R_i = 1.5$ kΩ, $C_i = 16$ pF, $s = 0.127$ cm, $d = 0.001$ cm, $V = 3.5$ kV, $a = 0.32$ cm, $\alpha = 2.26$) we find $v_{max}(\mu V) = 21 \times 10^{-4} A$ at $t = 7$ns, which decreases slowly to 10% of this value in about 150 ns. Taking 150 μV as the operating threshold level thus requires a gain $A = 7.0 \times 10^4$ so as to be sensitive to a single electron. Another operating condition of the detector was ($s = 0.254$ cm, $d = 0.002$

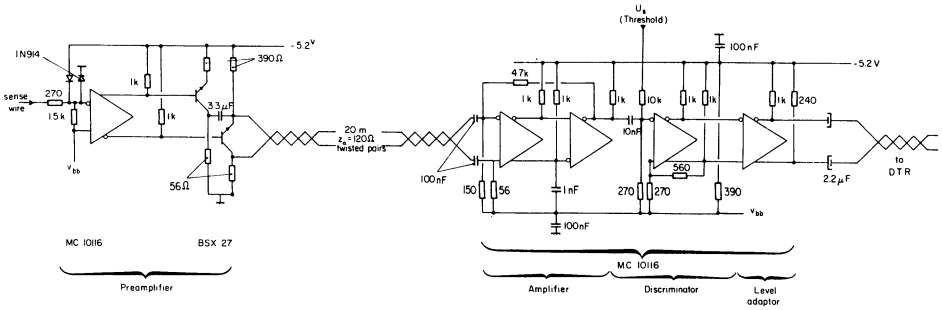


Fig. 9. Preamplifier, amplifier and discriminator circuits.

cm) which gives $v_{max}(\mu V) = 29 \times 10^{-4} A$ at $t = 10$ ns, hence single-electron sensitivity (150 $\mu$V threshold) when the gain $A = 5.2 \times 10^4$. The gain $A$ of the methane-filled MWPC has been measured to be $\sim 1.8 \times 10^5$ by observing an extrapolated 5 V signal out of the preamplifier when the chamber was irradiated with 5.9 keV X-rays from a $^{55}$Fe radioactive source. Since the voltage gain of the preamplifier is 50, this corresponds to a 100 mV signal on the wire. A converted X-ray in methane produces about 200 electrons. Thus the signal on the wire due to a single electron is 500 $\mu$V, which should be set equal to $28.6 \times 10^{-4} A$, hence the value $A = 1.8 \times 10^5$. This value may be a lower limit because of saturation effects due to such large signals. The chamber gain is thus 2 to 3 times bigger than necessary for single-electron sensitivity. This additional gain is important because of the large fluctuations in pulse height for single electrons (causing a loss in counting efficiency), and to minimize the slewing error in the arrival time measurement. This latter factor can be estimated to give rise to an r.m.s. error in the measured arrival time of $\sim 8.5$ ns$/\sqrt{12} = 2.5$ ns for a uniform pulse-height distribution.

The discriminated output (see figs. 8 and 9) for each wire is connected to a Drift Time Recorder (DTR Type 247 CERN) which digitizes the detection time of the input pulse, relative to a trigger pulse, at a frequency of 125 MHz. The DTR has 8 bits per channel and a memory which permits acceptance of up to 256 pulses on 16 wires (i.e. multi-hit capability). A time binning in 4 ns buckets is obtained by interpolation of the 8 ns period clock with a maximum time range of 2048 ns. The DTR modules are read via a standard CAMAC dataway by a fast microprocessor, called CAB (CAMAC Booster), developed at the Ecole Polytechnique. The microprocessor is based on the AM 2900 series (4-bit slices with 160 ns cycle time) and has a programming memory of 4K 24-bit words, a data memory of 4K 16-bit words controlled by an index register of 12 bits, a hard-cabled TRW multiplier/adder block of $16 \times 16$ bits, and an arithmetic and logic block ALU (AM 2901 series). The digitized data from the DTRs are transferred to CAB, where appropriate calculations are performed for each event. The resultant histograms are transferred to a Tektronix 4052 calculator for display on a cathode-ray screen and printed out on an associated hard-copy printer with the additional option of transfer of the data to 3M cassettes for later analysis off line. As an example of the calculations performed in CAB for straight-line beam tracks passing through the drift volume, the time digitizations $t_i$ from the $i$th wire (wire position $x_i$) for $N$ wires hit ($i = 1, ..., N$) are summed to give the moments $N\bar{x} = \Sigma x_i$, $N\bar{t} = \Sigma t_i$, $N\overline{x^2} = \Sigma x_i^2$, $N\overline{t^2} = \Sigma t_i^2$, and $N\overline{tx} = \Sigma t_i x_i$. We fit the straight-line hypothesis $t = ax + b$ using least-squares analysis to obtain

$$a = \frac{\overline{xt} - \bar{x}\bar{t}}{\overline{t^2} - \bar{t}2} \quad \text{and} \quad b = \bar{t} - a\bar{x}. \tag{4}$$

We calculate also the variance $\sigma$ of the straigth-line fit as

$$\sigma^2 = \frac{1}{N} \sum_{i=1}^{N} (t_i - ax_i - b)^2$$
$$= \overline{t^2} + a^2\overline{x^2} + b^2 - 2a\overline{tx} - 2b\bar{t} + 2ab\bar{x}, \tag{5}$$

which gives an estimate of r.m.s. error in a single point-time measurement. For each event (trigger) we calculate and histogram $\sigma$, $N$, $N(x_i)$, $N(t_i)$, where the latter two quantities are the number of times the $i$th wire is hit or fills the $t_i$th time bin. The probability that the $i$th wire is hit is then $N(x_i)/N$, which allows an estimate of the number of primary $dE/dx$ electrons produced in distance $s$ (wire spacing), as will be discussed in section 3.1. We have tested this complete read-out chain by pulsing the cathodes of the MWPC, which induced an equal time signal on each wire (hence simulating a horizontal beam track $t$ = constant). A fit to these simulated tracks gave $\sigma = 3$ ns, which indicates the intrinsic time resolution of the electronics and binning. The $\sigma$ expected with 4 ns time buckets is only 1.2

ns, the difference, in quadrature, of 2.7 ns being due to dispersion in the electronics.

## 3. Measurements of straight beam tracks

There are several potential difficulties connected with the operation of a drift chamber that has a long drift ($\geq 10$ cm), such as drift-field inhomogeneities causing image distortion and loss of drifting electrons, electron absorption by electronegative impurities in the drift gas, and electron diffusion, resulting in a decrease in the measurement precision. These problems were investigated by making measurements of the ionization created by relativistic charged beam particles traversing the drift region. The experimental layout is shown in fig. 10. The detector is oriented in the beam so that particles pass through the drift region between the two field-shaping electrode planes in a direction parallel to these planes and perpendicular to the MWPC wires. When oriented in position (a) of fig. 10, the charged particle produces ionization on all MWPC wires at equal times, whereas when tilted slightly to position (b) of fig. 10 the trajectory has a slight slope.

The measurements were made in the $c_{13}$ test beam of the CERN PS. This beam is a secondary beam derived from an extracted 24 GeV/$c$ proton beam. The beam momentum could be varied between 5 and 20 GeV/$c$, with beam intensity between $5 \times 10^3$ and $5 \times 10^4$ negative particles (mostly pions) per 300 ns spill. The tests described here were done at 10 GeV/$c$ with about $10^4$ particles per burst. The trigger was defined by a fourfold coincidence between two pairs of scintillators, placed upstream and downstream of the detector; this corresponds to a beam of about 5 mm diameter, with a maximum divergence of 1.7 mrad (see fig. 10). The fourfold coincidence gave about 50 triggers/burst.

### 3.1. Measurements without the calcium fluoride window

Measurements were first made without the $CaF_2$ entrance window in the detector. A Mylar window, mounted at a distance of 7 cm from the closest field-shaping electrode plane, was used to close off the detector gas volume. The detector was aligned as described above, and the charge collection efficiency of different parts of the drift region was investigated by varying the position of the drift gap-width $w$ relative to the beam, and the distance $d$ of the beam from the MWPC wire plane. The measurements were performed using a 15 mm thick drift gap with an argon (70%) + methane (29%) + TEA (1%) gas mixture (volume flow ratios corrected by $\sqrt{M_A/M}$, where $M_A$ and $M$ are the molecular weights of air and the flowing molecule) and a 1 kV/cm drift field. The indicated argon purity was 99.995%, while the methane was 99.95%. Both gases were further purified by passage through oxisorb and dryer chemical purifiers. The TEA liquid purity was 99.5%. The predominantly argon filling was chosen in order to produce a large number ($\sim 5$) of primary ionization electrons on each wire. The MWPC used had 43 wires at 2.54 mm pitch. Examples of data from two superimposed single tracks are shown in fig. 11. Note that the tracks have a slight slope and that every wire except the first two and the last one are hit. This is because the first and last wires of the MWPC are 100 $\mu$m in diameter (rather than 20 $\mu$m) and hence have negligible gain. The straight lines shown are from the least-squares fit (see subsection 2.3) and give a variance $\sigma = 6$ ns (using only wires 5 to 39 to minimize edge effects).

For $N$ through-going beam tracks the number of digitizations $N_i$ of the $i$th wire was measured to obtain a counting efficiency $\epsilon_i = N_i/N$. Assuming that the number of primary ionization electrons that are detected by the $i$th wire is Poisson distributed with a mean value $n_i$,

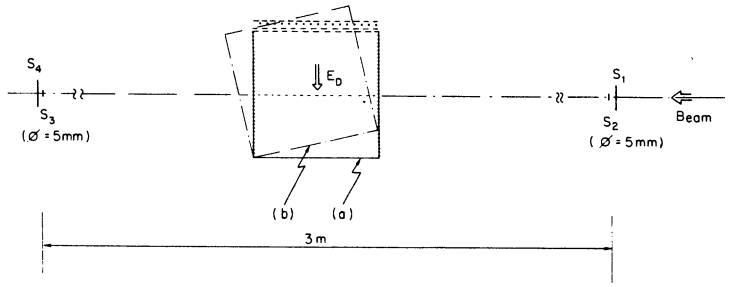


Fig. 10. Orientation of the drift detector to observe through-going beam tracks; (a) flat tracks at equal time; (b) sloping tracks at variable time.

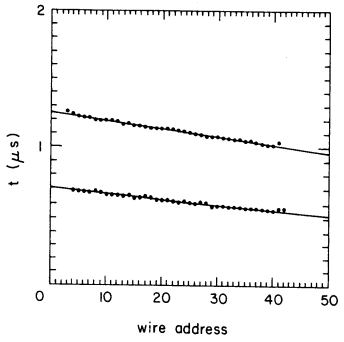


Fig. 11. Examples of two superimposed sloping tracks produced by 10 GeV/$c$ pions passing through the drift detector.

then the probability of not counting is $P(0) = e^{-n_i} = 1 - \epsilon_i$, hence

$$n_i = -\ln(1 - \epsilon_i). \quad (6)$$

If the efficiencies $\epsilon_i$ for 35 wires ($i = 5, \cdots, 39$) are reasonably uniform, we average the $n_i$ values to obtain the average number of primary ionization electrons $n_{pe} = \bar{n} = (1/35)\Sigma n_i$ and its variance $\sigma_n = \sqrt{\overline{n^2} - \bar{n}^2}$. In fig. 12a we see the values of $n_{pe}$ (error bars $\sigma_n$) versus the position $w$ of the beam relative to the drift gap at a drift distance $d = 100$ mm. This scan shows $n_{pe} = 5.4$ in the centre of the gap, with a linear fall-off when approaching the field-shaping electrodes that is compatible with an increasing fraction of the 5 mm diameter beam passing outside the drift gap. The value $n_{pe} = 5.4$ corresponds to the number of primary electrons collected on one wire spacing (2.54 mm); hence we find a value 21.3/cm. In fig. 12b are shown the measured values of $n_{pe}$ versus the drift distance $d$(when the beam is centred in the middle of the gap, i.e. $w = 7.5$ mm); this shows a plateau at $n_{pe} = 5.4$ with a similar fall-off when approaching the borders of the drift region as defined by the first ($U_1$) and last ($U_D$) field-shaping electrode wires. There is no indication of electron loss after a drift of up to 12 cm. In fig. 12c is plotted the recorded drift time (for flat equal-time tracks) as a function of the drift distance $d$. The drift time increases linearly with $d$, indicating a drift velocity which is independent of $d$, with a slope corresponding to a drift velocity of 5.6 cm/μs.

The data shown in fig. 12 indicate that the drift field is homogeneous throughout the drift region when the field strength $E_D = 1$ kV/cm. Varying the drift field strength, the collection efficiency remains constant from 1 kV/cm down to 0.2 kV/cm, as shown in fig. 13a for a drift distance $d = 100$ and $w = 7.5$ mm (closed circles). In fig. 13b the measured variation of the drift time with $E_D$ is plotted, showing that the maximum drift velocity occurs between 0.4 and 0.5 kV/cm in the argon (70%)

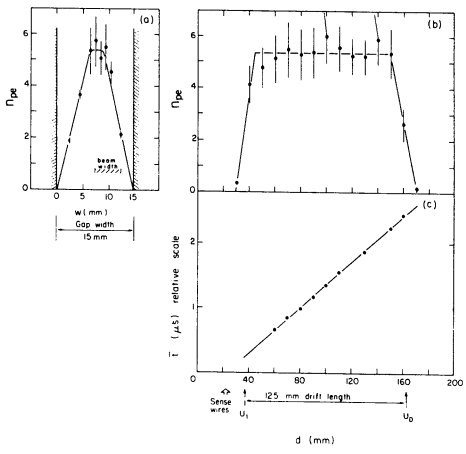


Fig. 12. (a) The average number of primary electrons $n_{pe}$ collected on each wire when the beam is scanned across the drift gap $w$ at a fixed drift distance $d = 100$ mm. (b) $n_{pe}$ vs drift distance $d$ when the beam is positioned in the gap centre $w = 7.5$ mm. (c) Relative drift time vs drift distance $d$ at $w = 7.5$ mm.

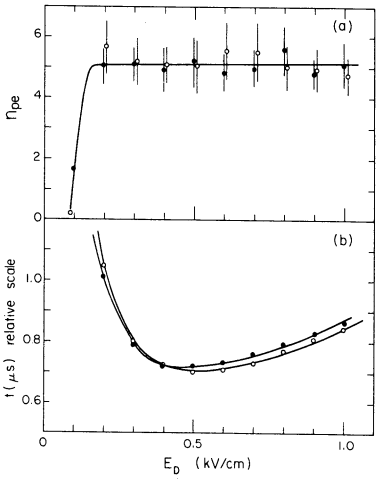


Fig. 13. (a) The average number of primary electrons $n_{pe}$ collected on each wire vs the drift field $E_D$ when the beam is centred in the gap $w = 7.5$ mm at a distance $d = 100$ mm. Closed circles are with no entrance window and open circles for a polarized $CaF_2$ entrance window. (b) Relative drift time vs drift time vs drift field $E_D$ with conditions as in (a).

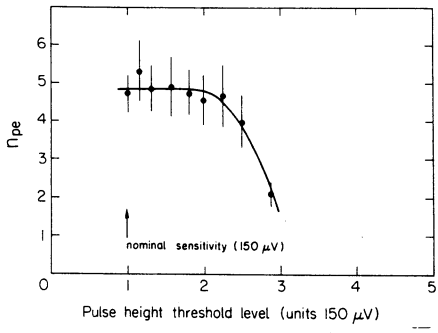


Fig. 14. The average number of primary electrons $n_{pe}$ collected on each wire vs preamplifier threshold level.

+ methane (29%) + TEA (1%) gas mixture used for these tests. Note also that the drift velocity does not plateau to a constant value. Increasing the voltage threshold of the discriminators, the number of collected primary electrons $n_{pe}$ was found to be constant for a discriminator threshold up to twice the normal value (150 μV), as shown in fig. 14.

### 3.2. *Measurements with an unpolarized calcium fluoride window*

Performing the measurements described in the previous section with a calcium fluoride window installed outside the entrance field-shaping electrode plane (see fig. 5) gave results which strongly deviated from the earlier results and which changed with time. Fig. 15 shows the average number of primary electrons $n_{pe}$ collected per wire, obtained with the beam in the median plane $w = 7.5$ at a distance $d = 100$ mm from the MWPC

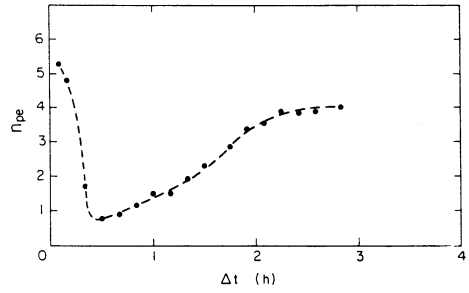


Fig. 15. Variation of average number of primary electrons collected per wire $n_{pe}$ vs elapsed time $\Delta t$ after turning on drift field with an unpolarized $CaF_2$ entrance window. Drift distance $d = 100$ mm, beam centred in gap $w = 7.5$ mm and $E_D = 1$ kV/cm.

anode plane as a function of elapsed time after the drift voltage was applied. During the first moments $n_{pe} = 5.4$ as before, but after half an hour $n_{pe}$ falls to about 1, after which it slowly rises, during the following two hours, up to a value of 4. Further studies showed that $n_{pe}$ continued to vary, with some tendency toward stability but never reached the original high wire-collection efficiency (i.e. $n_{pe} = 5.4$).

Plotting the wire efficiency $\epsilon_i = N_i/N$ for each of the 43 anode wires for $N = 500$ events shows how the losses are distributed in the drift volume. In fig. 16, histograms collected with $d = 100$, $w = 7.5$ mm at different times after the drift voltage has been turned on, show how the deterioration of the collection efficiency occurs preferentially at the borders of the drift volume. Fig. 17 shows histograms collected at approximately the same time, but with the beam positioned at $w = 7.5$ mm and different distances $d$ from the MWPC plane. The depletion is seen to be large at large drift distances ($d \geqslant 80$ mm).

From these data we concluded that the deterioration in the charge collection efficiency is due to varying inhomogeneities in the electric drift field, which in turn are due to slow and irregular charging-up of the calcium fluoride entrance window.

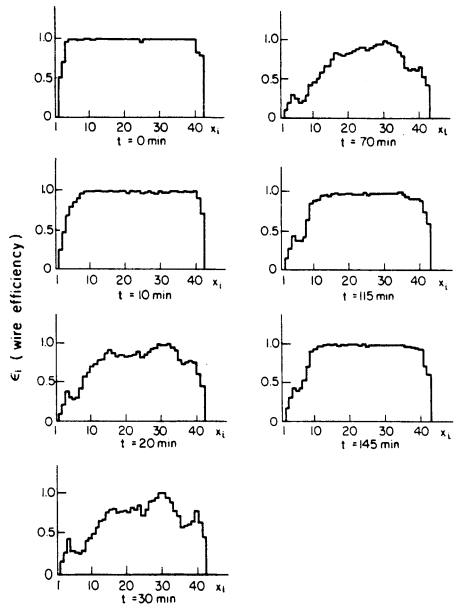


Fig. 16. Wire efficiency $\epsilon_i$ vs elapsed time after turning on the drift field when the $CaF_2$ entrance window is unpolarized. Drift distance $d = 100$ mm, $w = 7.5$ mm, $E_D = 1$ kV/cm.

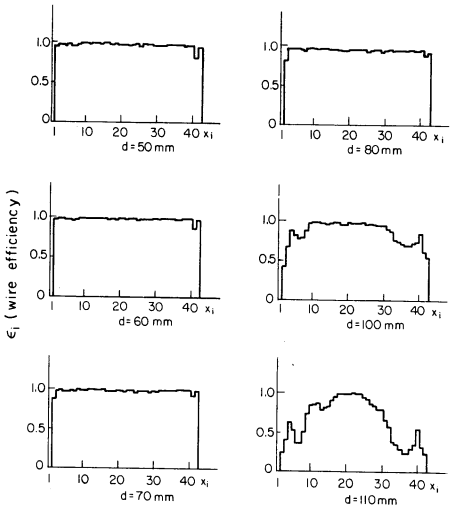


Fig. 17. Wire efficiency $\epsilon_i$ vs drift distance $d$ when the $CaF_2$ entrance window is unpolarized. Drift field $E_D = 1$ kV/cm and beam centred in gap $w = 7.5$ mm.

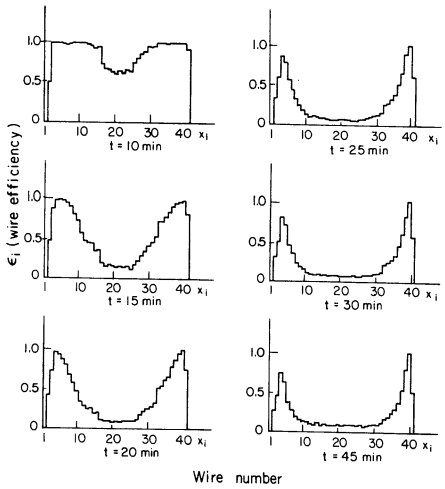


Fig. 18. Wire efficiency $\epsilon_i$ vs elapsed time after turning on drift field when the unpolarized $CaF_2$ entrance window is not in contact with the field-shaping electrode (separation 0.2 mm). Drift distance $d = 100$ mm, $w = 7.5$ and $E_D = 1$ kV/cm.

In the measurements of figs. 15–17 the window was in direct contact with the field-shaping electrode plane, making charge collection from the window surface to the field wires possible. To check the influence of this collection, measurements were made with the window 0.2 mm away from the field-shaping electrode plane, again at $d = 100$ and $w = 7.5$ mm. Fig. 18 shows the time evolution in this situation. Again the collection efficiency deteriorates, but in this case depletion occurs in the central part of the drift region.

### *3.3. Measurements with the calcium fluoride window polarized*

From the results described above, we tentatively concluded that in order to define a stable and homogeneous drift field inside the drift volume in the presence of the dielectric calcium fluoride window, the potential had to be defined also on the outside of this window. Having a field-shaping electrode plane on both sides eliminates uncontrolled charge accumulation on the outer window surface and polarizes the dielectric medium parallel to the window surface. Since the $CaF_2$ window was already glued in place, a second $CaF_2$ window was added, inside the drift volume, with field-shaping electrode planes on both sides of this inner window (see figs. 3 and 4). As already mentioned, this turned out to be convenient in later tests when this inner $CaF_2$ window was replaced by a fused quartz window for investigations with the photoionizing gas TMAE. In addition, to avoid charge accumulation in the legs of the U-frame, the potential-defining lines were made to encircle the U-frame legs.

In fig. 19a the results obtained with the window polarized are shown (open circles) and compared with the results obtained with the window unpolarized (closed circles). The collected charge ($n_{pe}$) remains high ($\approx 5.4$) up to a distance $d = 120$ mm, whereas with the window unpolarized it decreases significantly beyond $d = 80$ mm. Fig. 19b shows the scan over the gap width $w$ (at $d = 100$ mm), again indicating more efficient collection with the window polarized (open circles) than for the window unpolarized (closed circles). The former is as good as the measurement without window (see fig. 12a). The collected charge ($n_{pe}$) as a function of drift field is plotted in fig. 20 (open circles) and is compared to the unpolarized window case (closed circles). This curve shows efficient collection down to a field of 0.2 kV/cm, as was observed when no window was present. These data (open circles) are directly compared with the no-window data in fig. 13 (closed circles). We note that for the window unpolarized the drift field required for efficient collection is very high ($E_D \geq 1$ kV/cm) when $d > 100$ mm.

The equality of the collected charge $n_{pe} = 5.4$ when the window is polarized and without window, and its independence with drift distance, indicate that electron loss through drift-field distortions and gas absorption is

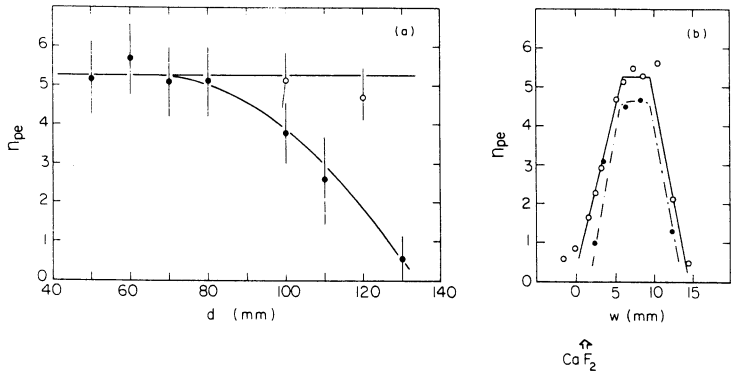


Fig. 19. The average number of primary electrons $n_{pe}$ collected on each wire with the $CaF_2$ entrance window polarized (open circles) and unpolarized (closed circles) vs (a) drift distance $d$ with $w = 7.5$ mm and $E_D = 1$ kV/cm, and (b) position of beam in the drift gap $w$ with $d = 100$ mm and $E_D = 1$ kV/cm.

small and that electron collection is efficient throughout the drift volume.

## 4. Drift velocity measurements in various gas mixtures

To measure the drift velocity the detector was placed in the 10 GeV/$c$ pion beam such that the beam was incident normally to the entrance window and parallel to the MWPC wires. In this geometry all the ionization electrons drift to only one or two wires of the MWPC where the drift time is measured at a given value of drift field strength $E_D$. The detector was then displaced a known distance, so as to increase (or decrease) the drift distance $d$, and the drift time was again measured. A plot of the measured drift time versus drift distance gave a straight line whose slope is the drift velocity $v_D$ at the set value of electric field $E_D$.

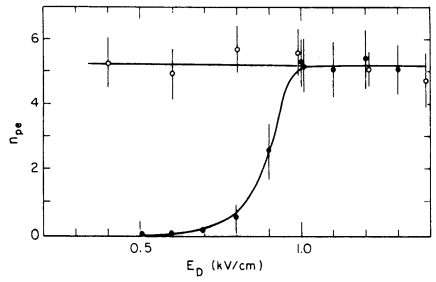


Fig. 20. The average number of primary electrons $n_{pe}$ collected on each wire with the $CaF_2$ entrance window polarized (open circles) and unpolarized (closed circles) vs drift electric field $E_D$ when the drift distance $d = 100$ mm and $w = 7.5$ mm.

The amplifying and drift carrier gas used in the photon drift detector should satisfy a number of requirements. It should have a large first Townsend coefficient so as to allow sufficient gas amplification; it should be opaque (or partially opaque) to the photons emitted in the avalanche amplification process so as to quench the discharge; it should have a small diffusion coefficient to allow accurate localization of the photon conversion point; and its drift velocity should not vary too strongly with drift field so as to allow stable operation. Furthermore, for use in Cherenkov ring imaging, it should be transparent over some range in the UV region where the photoionizing vapours (TEA or TMAE) are sensitive. As shown in ref. 3, methane satisfies all these requirements.

Various combinations of methane ($CH_4$), ethane ($C_2H_6$), isobutane (iso-$C_4H_{10}$), and carbon dioxide ($CO_2$) gases with small admixtures of TEA and TMAE were investigated. These gases are all transparent, to varying degrees, in the region up to 9 eV photon energy, as is shown in fig. 21. Also shown in this figure are our present best estimates of the quantum efficiency of TEA and TMAE. As can be seen from fig. 21 only methane can be used when the photoionizing vapour is TEA, whereas for TMAE, combinations of methane, ethane, and $CO_2$ are possible. The TEA and TMAE quantum efficiency curves shown have been measured with methane as a carrier gas so the high-energy cut-off reflects only the onset of methane absorption rather than an intrinsic decrease of quantum efficiency above 8.5 eV. Measurements using argon as the carrier gas (transparent to 11 eV) are planned so as to determine the quantum efficiency of TEA and TMAE in the 8.5–11 eV energy region.

The drift velocities measured are shown in fig. 22

versus the drift electric field. Note that the $CH_4$ + TMAE (curve a) and $CH_4$ + TEA (b) drift velocities plateau to a value of about 9.7 cm/$\mu$s above 0.6 kV/cm, whereas the argon + TEA (curve f) drift velocity has a maximum at 0.6 kV/cm and subsequently decreases. The other curves for $CH_4$, $C_2H_6$, iso-$C_4H_{10}$, and $CO_2$ show monotonically rising drift velocities with increasing electric field. The sharpest rise is shown by $CH_4$ with $CO_2$ mixtures (curves d and h). This strong dependence of $v_D$ with $E_D$ coupled with the low value of $v_D$ at low electric fields ($E_D \leq 0.5$ kV/cm) argues against the use of $CO_2$. From the viewpoint of fastest drift the $CH_4$ + TMAE and $CH_4$ + TEA mixtures are clearly superior, i.e. a total drift time of 2 $\mu$s for 20 cm drift distance. Mixtures of $CH_4$ + iso-$C_4H_{10}$, even though slower, are interesting because of their increased ability to quench the avalanche discharge around a MWPC wire and the almost exact match with the quartz transmission cut-off. In fig. 23 are shown the measurements of drift velocity versus the percentage of isobutane in methane + isobutane mixtures for the given fixed value of the drift field $E_D$. Even though the drift velocity in an argon + TEA mixture was measured (curve f in fig. 22) it is not considered as a useful drift and amplifying gas mixture because of its large diffusion coefficient (see section 5) and because the single photoelectron counting efficiency is low without preamplification [3].

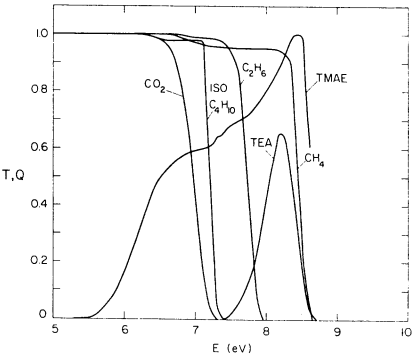


Fig. 21. Transmission $T$ vs photon energy $E$ of 10 cm long samples of methane (99.95%), ethane (99.97%), isobutane (99.95%), and carbon dioxide (99.9%) all treated by flowing through oxisorb and dryer chemical purifiers. Shown also are the quantum efficiencies $Q$ of TEA and TMAE in methane. The decrease of $Q$ at high energies (8.5 eV) is due to photon absorption in methane and does not reflect the true quantum efficiency of these molecules above 8.5 eV.

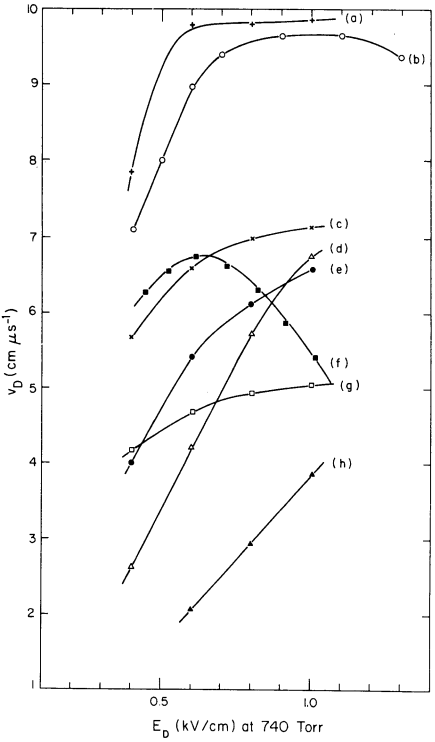


Fig. 22. Drift velocity $v_D$ vs electric field $E_D$ for (a) 100% $CH_4$ flowing through liquid TMAE (27°C), (b) 88.5% $CH_4$ with 11.5% $CH_4$ flowing through liguid TEA (3°C), (c) 85% $CH_4$ with 15% $C_2H_6$, (d) 97% $CH_4$ with 3% $CO_2$, (e) 89% $CH_4$ with 11% iso-$C_4H_{10}$, (f) 80% argon with 20% argon flowing through liquid TEA (3°C), (g) 100% $C_2H_6$ flowing through liquid TMAE (27°C), (h) 87% $CH_4$ with 13% $CO_2$. The argon gas purity was 99.995%, that of TEA was 99.5%; the TMAE purity was unknown and the other gases as listed in fig. 21.

## 5. Accuracy of the measured drift coordinate

Straight lines were fitted to 10 GeV/$c$ pion beam tracks as illustrated in fig. 11 and outlined in section 2.3. The variance $\sigma$ [see eq. (5)] of the fit provides a measurement of the accuracy to which the drift time is determined. This quantity is limited by the amount of longitudinal diffusion of the drifting electron(s) in the gas, by the time binning and electronics dispersion, and by any inhomogeneities in the drift field. Fig. 24 (taken from ref. 5) shows the measured or calculated values of the transverse diffusion coefficient $\sigma_t$ for a single electron versus the drift field $E_D$ in pure argon, $CH_4$, iso-$C_4H_{10}$, and $CO_2$. The measured longitudinal diffu-

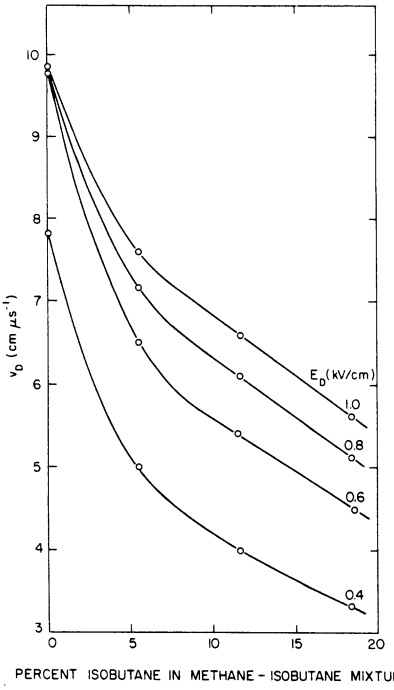


Fig. 23. Drift velocity $v_D$ vs volume percent of isobutane in methane–isobutane mixtures for fixed values of the drift electric field $E_D$.

sion coefficient $\sigma_l$ (as well as $\sigma_t$) for an argon (87%) + $CH_4$ (10%) + iso-$C_4H_{10}$ (3%) mixture used in the JADE detector [6] has been added in fig. 24. From this figure we note that the diffusion coefficient $\sigma_t$ in argon is extermely large, so to obtain highest precision a predominantly argon gas mixture should be avoided. Methane, isobutane, and $CO_2$ all have small diffusion coefficients; however, as indicated earlier, the low drift velocities which characterize $CO_2$ mixtures mitigate against its use. Since efficient single-electron counting in methane has been proved possible, we have concentrated on measurements with methane and small admixtures of isobutane to enhance quenching. As seen from fig. 24, the longitudinal diffusion coefficient in the JADE gas mixture is about a factor of 2 smaller than the transverse coefficient. This inequality, $\sigma_l < \sigma_t$, has been shown [7] to be true for Ar, $H_2$, $N_2$, He, CO and $C_2H_4$ whereas for $CH_4$ and $CO_2$ these coefficients are equal. We plan to measure the longitudinal and transverse coefficients in methane + isobutane (or $C_2H_4$) mixtures (with TEA or TMAE) using a pulsed (2 ns) UV-light source to produce single electrons in a long drift (~60 cm) volume inside a solenoidal magnetic field.

The measurements reported in this section were obtained with a second drift gap of the same construction as described previously but with a 45 mm gap (instead of 15 mm) and a MWPC wire spacing of 1.27 mm instead of 2.54 mm with 10 $\mu$m diameter wires (instead of 20 $\mu$m). The gas mixture used was methane (89%) + isobutane (11%) at atmospheric pressure but at an elevated temperature. The temperature of the outer support box was kept at 34°C, hence the gas temperature inside was probably higher than this value. Throughgoing beam tracks at a gap depth $w$ were observed and the ionization electrons were collected on the MWPC wires after drifting a distance $d$ in a drift electric field $E_D$. For each track a straight line fit was made with variance $\sigma$, and histograms of $\sigma$, $N$, $N(x_i)$, and $N(t_i)$ were obtained for 500 tracks as described in section 2.3. From the efficiency of each wire the number of primary electrons on each wire is calculated and this is averaged over the wires to obtain $n_{pe}$. The measurements are shown in fig. 25a, where $n_{pe}$ is shown versus the position $w$ of the beam in the gap. A constant value $n_{pe} = 1.5$

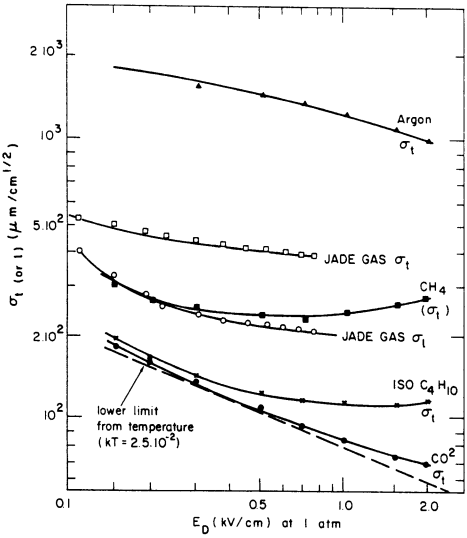


Fig. 24. Experimental values (from ref. 5) of the diffusion coefficents $\sigma_t$ or $\sigma_l$ vs electric drift field $E_D$ at atmospheric pressure. The iso-$C_4H_{10}$ curve is calculated. The values of $\sigma_t$ and $\sigma_l$ (from ref. 6) for the JADE gas (87% argon + 10% $CH_4$ + 3% iso-$C_4H_{10}$) have been added. The measured values of $\sigma_l$ (from ref. 7) for $C_2H_4$ follow very closely the $\sigma_t$ curve for iso-$C_4H_{10}$ and the $\sigma_l$ for $CO_2$ follows the $\sigma_t$ curve shown for $CO_2$.

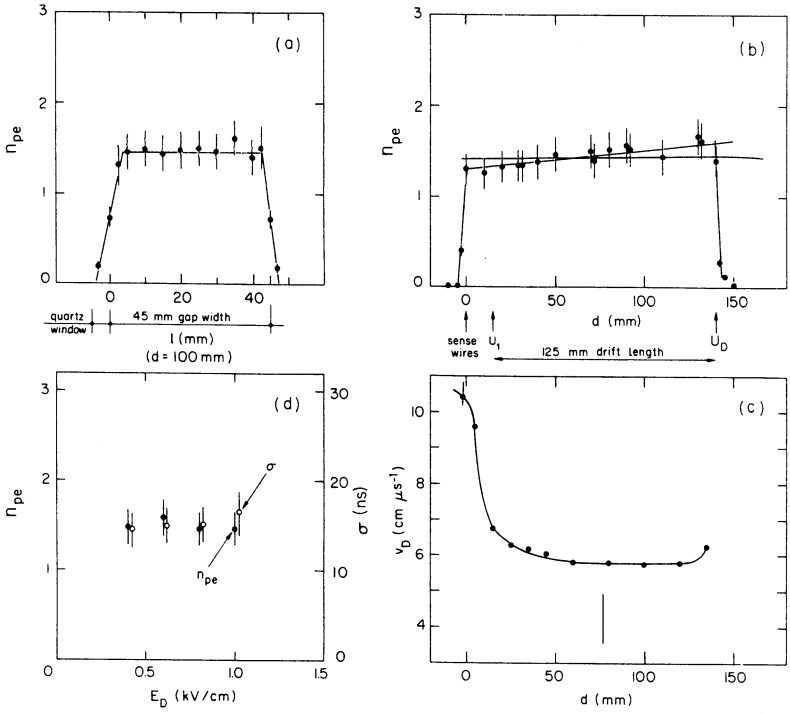


Fig. 25. The average number of primary electrons $n_{pe}$ collected per wire vs (a) gap width $w$ at drift distance $d = 100$ mm and $E_D = 0.6$ kV/cm, (b) drift distance $d$ at gap width $w = 22.5$ mm and $E_D = 0.6$ kV/cm. (c) The local drift velocity $v_D$ vs drift distance $d$ at gap width $w = 22.5$ mm and $E_D = 0.6$ kV/cm. (d) The $n_{pe}$ and the $\sigma$ of the straight line fit vs drift electric field $E_D$ at drift distance $d = 100$ mm and gap width $w = 22.5$ mm.

is observed throughout the 45 mm thick gap. Here, the value $n_{pe} = 1.5$ is smaller than the value 5.4 obtained previously (see fig. 12) because of a lower gas density, atomic charge, and wire spacing. Fig. 25b shows a scan in drift distance $d$, where a slight decrease in collection efficiency perhaps occurs at short drift distances. In fig. 25c the local drift velocity $v_D$ (measured time difference $\Delta t$ of two flat equal-time tracks with incremental drift distance $\Delta d$) is plotted versus drift distance $d$. We note a large increase in $v_D$ between $U_1$ and $U_{pC}$ indicating that field inhomogeneities remain in this 14 mm long region. Fig. 25d shows that $n_{pe}$ and the variance $\sigma$ are constant when the drift field $E_D$ is varied from 0.4 kV/cm to 1.0 kV/cm. From the average constant value $n_{pe} = 1.5$ and wire spacing 0.127 cm we calculate that 11.8 primary electrons are produced in 1 cm of this $CH_4$ (89%) + iso-$C_4H_{10}$ (11%) gas mixture at atmospheric pressure and temperature $\geq 34$°C.

To measure the longitudinal diffusion coefficient, the variance $\sigma^2$(ns) of the straight line fit was plotted versus

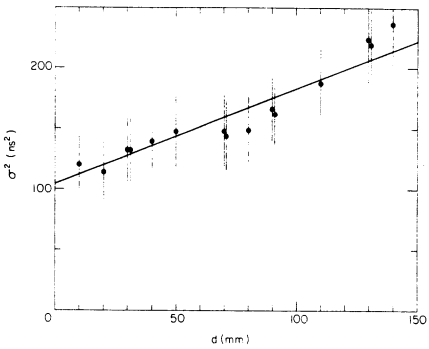


Fig. 26. The variance $\sigma^2$ of the straight-line fits plotted vs drift distance $d$ for $w = 22.5$ mm and $E_D = 0.6$ kV/cm. The straight-line fit $\sigma^2 = \sigma_0^2 + \sigma_1^2 d$ has values $\sigma_0 = 10.2$ ns and $\sigma_1 = 2.81$ ns/cm$^{1/2}$.

$d$ as shown in fig. 26. A straight line $\sigma^2 = \sigma_0^2 + \sigma_1^2 d$ has been fit to the data giving $\sigma_0 = 10.2$ ns and $\sigma_1 = 2.81$ ns/cm$^{1/2}$. Multiplying these quantities by the drift velocity $v_D = 5.75$ cm/$\mu$s gives the space errors $\sigma_0 = 590$ $\mu$m and $\sigma_1 = 162$ $\mu$m/cm$^{1/2}$. The magnitude of the $\sigma_0$ error is due partially to electronics dispersion (2.7 ns) and to time binning (1.2 ns), but the remainder (9.7 ns) is attributed to the drift field inhomogeneity between $U_1$ and the MWPC cathode $U_{PC}$. This defect has been corrected in a later drift gap (Mark II) where $\sigma_0 = 5.6$ ns has been realized. The single-electron longitudinal diffusion coefficient $\sigma_\ell$ is related [8] to $\sigma_1$ through the equation

$$\sigma_1 = \frac{\pi}{2\sqrt{3 \ln n}} \sigma_\ell, \tag{6}$$

where $n$ is the total number (primaries + secondaries) of electrons which contribute to the measurement of $\sigma_1$ when the electronics is sensitive to a single electron. The total number of electrons is $n = k n_{pe}$ with $k$ between 3 and 5; however, the resulting value of $\sigma_1$ is comparatively insensitive to the exact value of $k$. Using $k = 4$ and $n_{pe} = 1.5$ we obtain $\sigma_\ell = 1.48\sigma_1$, hence $\sigma_\ell = 240$ $\mu$m/cm$^{1/2}$. This result may be compared with the data in fig. 24, which give the values $\sigma_t = 230$ $\mu$m/cm$^{1/2}$ for methane and $\sigma_t = 120$ $\mu$m/cm$^{1/2}$ for isobutane (calculated) at $E_D = 0.6$ kV/cm. Our result is $\sigma_\ell \approx \sigma_t$ for methane (since our gas mixture is predominantly methane), which agrees with the data of ref. 7 for $\sigma_\ell$.

An improved drift cage (Mark II) has been constructed as shown in fig. 27. It has a 140 mm long drift distance between the extreme field-shaping electrodes $U_D$ and $U_1$ with a transfer mesh at voltage $U_T$ between $U_1$ and the MWPC cathode $U_{PC}$. The distance $U_1$ to $U_T$ is 4.8 mm, $U_T$ to $U_{PC}$ is 3.2 mm, and $U_{PC}$ to the sense wire plane is 3.2 mm. The sense wires of 10 $\mu$m diameter and 50 mm length are spaced 1.27 mm apart. The transverse dimension of the drift volume is 185 mm and

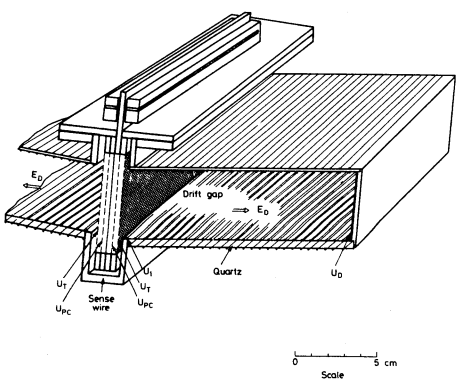


Fig. 27. Schematic view of the modular Mark II drift gap.

the detector plane contains 145 wires. As may be seen in fig. 27, this drift cage is self-contained (i.e. not mounted inside an outer support box), with three sides of the box, 40 mm deep, made of 1.6 mm thick Stesalite on both sides of which are glued Kapton printed-circuit sheets. These printed circuits have parallel conducting copper strips, 100 $\mu$m wide, every 2.54 mm. The fourth side of the box has a quartz rectangular entrance window (140 mm $\times$ 185 mm) on which are wound 100 $\mu$m diameter wire loops, also with 2.54 mm pitch. This window is glued to the Stesalite–Kapton drift cage, with the wire loops in electrical contact with the Kapton printed-circuit strips. A resistance chain mounted near the box provides the electric potentials to the strips which, because of the contact between the strips and the loops, are conducted to both sides of the quartz entrance window. The fifth side of the box is closed by a Stesalite plane, fully copper plated on the inside of the box and connected to the high potential $U_D$. The sixth and last side of the box is closed by the transfer mesh and MWPC array. The box is gas-tight and has gas input and output leads located near the MWPC array. This unit is modular in the sense that it has been designed so that many such units can be mounted, for example, like the lines of longitude and latitude to cover a spherical surface.

The Mark II detector has been tested with through-going 10 GeV/$c$ pion beam tracks, as described above, with two different gas mixtures (1) pure $CH_4$, and (2) $CH_4$ (89%) + iso-$C_4H_{10}$ (11%) at atmospheric pressure and 20°C. The average number of primary electrons $n_{pe}$ measured is shown in fig. 28a versus drift distance $d$ for the two gas mixtures. We find $n_{pe} = 1.1$ and 1.8, respectively, where the latter number should be compared with the value $n_{pe} = 1.5$ found using the original (Mark I) field cage with the same $CH_4$ (89%) + iso-$C_4H_{10}$ (11%) gas mixture (see fig. 25); however at an elevated temperature $\geqslant 34$°C. This difference in $n_{pe}$ for the two measurements is attributed to a difference in gas densities caused by the disparity in temperatures. The local drift velocity $v_D$ versus drift distance in Mark II is shown in fig. 28b, where we find $v_D = 9.9$ cm/$\mu$s and 5.4 cm/$\mu$s, respectively, with a rapid change of $v_D$ only near the MWPC wire plane as expected. Thus a much better linearity of the electric field is observed compared to the Mark I drift cage (see fig. 25c).

In fig. 29 the variance of the straight line fits $\sigma^2$ (ns) is plotted versus $d$, and straight lines of the form $\sigma^2 = \sigma_1^2 + \sigma_2^2 d$ are fitted to these data. The parameters are:

for (1) $\sigma_0 = 5.8$ ns and $\sigma_1 = 1.74$ ns/cm$^{1/2}$;
and with $v_D = 9.9$ cm/$\mu$s, giving
$\sigma_0 = 574$ $\mu$m and $\sigma_1 = 172$ $\mu$m/cm$^{1/2}$;
for (2) $\sigma_0 = 5.4$ ns and $\sigma_1 = 2.80$ ns/cm$^{1/2}$;
and with $v_D = 5.4$ cm/$\mu$s, giving
$\sigma_0 = 292$ $\mu$m and $\sigma_1 = 151$ $\mu$m/cm$^{1/2}$.

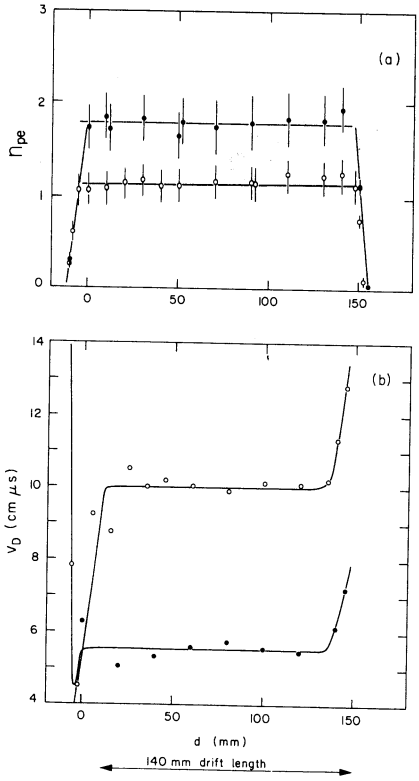


Fig. 28. (a) The average number of primary electrons $n_{pe}$ collected per wire vs drift distance $d$ in the Mark II drift gap with the beam centred in the gap and $E_D = 0.6$ kV/cm. The open circles are for pure methane and the closed circles for 89% $CH_4$ + 11% iso-$C_4H_{10}$ gas mixture. (b) The local drift velocity vs drift distance $d$ with conditions as in (a).

Correcting for the total number of electrons $n = 4n_{pe}$ we obtain (1) $\sigma_\ell = 231$ $\mu$m/cm$^{1/2}$ and (2) $\sigma_\ell = 234$ $\mu$m/cm$^{1/2}$, respectively, for the two different gas mixtures. These numbers should be compared to $\sigma_\ell = 240$ $\mu$m/cm$^{1/2}$ obtained with the previous (Mark I) detector. It is not thought that these numbers are significantly different, so the average of $\sigma_\ell = 235$ $\mu$m/cm$^{1/2}$ represents the results of our longitudinal diffusion coefficient measurements in pure $CH_4$ or $CH_4$ (89%) + iso-$C_4H_{10}$ (11%) at a drift field of $E_D = 0.6$ kV/cm. There is, however, a significant difference in $\sigma_0$ for the Mark II detector. This value has been reduced to 5.6 ns, compared with 10.2 ns for the Mark I detector. This represents an approximately 4.7 ns contribution due to field

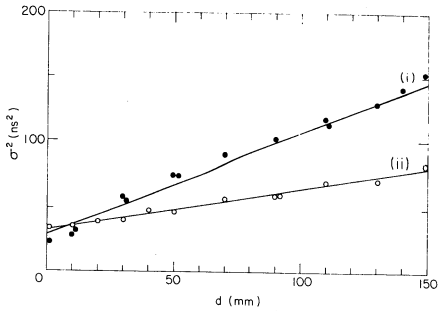


Fig. 29. The square of the variance $\sigma$ of the straight-line fits for the Mark II drift gap plotted vs drift distance (1) for pure $CH_4$ and (2) for a mixture of 89% $CH_4$ + 11% iso-$C_4H_{10}$. The straight-line fits are of the form $\sigma^2 = \sigma_0^2 + \sigma_1^2 d$ with (1) $\sigma_0 = 5.8$ ns and $\sigma_1 = 1.74$ ns/cm$^{1/2}$, and (2) $\sigma_0 = 5.4$ ns and $\sigma_1 = 2.8$ ns/cm$^{1/2}$.

inhomogeneities, compared to 9.7 ns for the Mark I detector, hence a significant improvement. In a slow gas mixture such as $CH_4$ (89%) + iso-$C_4H_{10}$ (11%) 5.6 ns corresponds to an intrinsic spatial error $\sigma_0 \simeq 300$ $\mu$m, whereas for a fast gas such as $CH_4$ this error becomes $\sigma_0 = 500$ $\mu$m. The 2.7 ns contribution from electronics dispersion is not intrinsic and can largely be removed by calibrating each channel. However, this has not been done in treating the data reported in this paper.

## 6. Summary and conclusions

A drift detector, capable of localizing single photoelectrons, has been constructed and tested by measuring ionization tracks from relativistic charged particles. A first conclusion from these tests is that it is necessary to apply field-shaping conductive strips to both the inside and the outside of the dielectric walls surrounding the drift volume in order to have a stable and homogeneous electric field inside. It is furthermore necessary to have the drift volume surrounded by potential-defining strips all the way up to the MWPC cathode plane, so as to avoid field distortions which produce timing errors.

The spatial resolution of the detector is limited by several sources of error. In the drift (longitudinal) direction, one component of the error is proportional to the square root of the drift distance and the proportionality constant has been measured to be $\sigma_\ell = 235$ $\mu$m/cm$^{1/2}$ for predominantly methane gas mixtures. A second component of the error which is independent of the drift distance is due to error in the drift time measurement. This component has been determined, in the best case, to be $\sigma_{0t} = 5.6$ ns corresponding to a 300 $\mu$m constant positional error. In the direction transverse to

the electric field, there are also two error components, the first being again proportional to the square root of the drift distance with the proportionality constant given by the transverse diffusion coefficient $\sigma_t$. We have not here measured this quantity; however, classical Townsend electron diffusion experiments [9,10] give this quantity. The second component of the error in the transverse coordinate is due to the wire spacing of the MWPC that detects the drifting electrons. It has a value $\sigma_{0t} = s/\sqrt{12}$, where $s$ is the wire spacing. For a drift over a maximum distance $D$, the average of the distance-dependent error is $\frac{2}{3}\sigma\sqrt{D}$. Adding the independent error components in the quadrature we obtain

$$\sigma_y^2 = \sigma_{ot}^2 + \tfrac{4}{9}\sigma_t^2 D, \quad \sigma_x^2 = \tfrac{1}{12}s^2 + \tfrac{4}{9}\sigma_t^2 D, \tag{7}$$

as the average square errors in the two directions $(x, y)$ over the detector surface.

The intrinsic resolution of a Cherenkov ring image is given by $\Delta\theta_c$, the chromatic aberrations of the focused image [1]. This quantity depends on the optical dispersion of the Cherenkov radiating medium and is given approximately as $\Delta\theta_c = \Delta n/\sqrt{12n^2(n^2-1)}$, where $n$ is the refractive index and $\Delta n$ is the difference of refractive indices of the two extreme photon energies detected. The corresponding spatial resolution $\Delta r$ is determined by the mirror focal length $f$ as simply $\Delta r = f\Delta\theta_c$. An approximate optimization of error sources requires that the detector resolution $1/2(\sigma_x^2 + \sigma_y^2)$, averaged over the circular image, should be equal to $(\Delta r)^2$. Using eq. (7) to solve for the optimal drift distance $D$ as

$$D = \frac{2(\Delta r)^2 - \sigma_{ot}^2 - s^2/12}{4(\sigma_t^2 + \sigma_t^2)/9}. \tag{8}$$

As an example, for $\Delta\theta_c = 1$ mrad, $f = 1000$ mm we find $\Delta r = 1$ mm. Taking $s = 1.27$ mm, $\sigma_{ot} = 0.3$ mm, $\sigma_t = \sigma_t = 0.235$ mm/cm$^{1/2}$ as measured, we find $D = 36.2$ cm, corresponding to a drift length more than double that of the present detector (Mark II). To cover e.g. 1 m$^2$ of detection surface three drift zones, each of 33.3 cm in length, are separated by three rows of MWPC wires, 1 m in lenght, each containing 787 wires. Such a detector, covering 1 m$^2$, has $5 \times 10^5$ resolution elements (pixels) at the cost of instrumenting $3 \times 787 = 2361$ proportional chamber wires. Such a detector allows reconstruction of the ring images without ambiguity, with sufficient precission, at minimal cost.

For shorter focal lenghts, $\Delta r$ decreases; hence, from eq. (8), the diffusion coefficients must decrease if long (economical) drift distances are to be used. This can certainly be achieved with $CH_4 + CO_2$ drift gas mixtures where $\sigma_t = \sigma_t = 0.1$ mm/cm$^{1/2}$ have been measured [7,10]; however, as previously discussed, such mixtures have low drift velocities. Other gases such as $C_2H_2$, $C_2H_4$, $C_3H_6$, $C_3H_8$, and $SiH_4$ have been measured to have low values of $\sigma_t \approx \sigma_t = 0.14$ mm/cm$^{1/2}$, however with reasonable drift velocities (2–4 cm/$\mu$s) at 0.6 kV/cm drift field. The first four of the above gases are transparent below 7 eV ($SiH_4$ has not been measured) and so could be used for Cherenkov ring imaging with TMAE and quartz. We have not yet tried to count single photoelectrons with additions of these gases to methane but plan to do so in the near future.

We wish to acknowledge the aid and support of Dr. A. Wetherell and Dr. E. Gabathuler of CERN, Dr. P. Fleury of the Ecole Polytechnique, Dr. S. Kullander of the University of Uppsala and Dr. M. Froissart of Collège de France. The technical aid of D. Bernier, R. Bouhot, A. Brehm, C. Detraz, B. Goret, J.P. Hubert, C. Muratori, P. Quéru and C. Rivoiron, and the electronic design of Y. Kornelis were very important in this work, and to them we express our thanks.

## References

[1] T. Ypsilantis, Physica Scripta 23 (1981) 370.
[2] J. Séguinot and T. Ypsilantis, Nucl. Instr. and Meth. 142 (1977) 377.
[3] T. Ekelöf, J. Séguinot, J. Tocqueville and T. Ypsilantis, Physica Scripta 23 (1981) 718.
[4] G. Charpak and F. Sauli, Phys. Lett. 78B (1978) 523. See also J. Séguinot, J. Tocqueville and T. Ypsilantis, Nucl. Instr. and Meth. 173 (1980) 283.
[5] V. Palladino and B. Sadoulet, Nucl. Instr. and Meth. 128 (1975) 323.
[6] H. Drum et al., Nucl. Instr. and Meth. 176 (1980) 333, from the data of B. Schmitt, Diplomarbeit, Phys. Inst. der Univ. Heidelberg (1980).
[7] E. B. Wagner, F.J. Davis and G.S. Hurst, J. Chem. Phys. 47 (1967) 3138.
[8] W. Farr, J. Heintze, K.H. Hellenbrand and A.H. Walenta, Nucl. Instr. and Meth. 154 (1978) 175.
[9] T.L. Cottrell and I.C. Walker, Trans. Faraday Soc. 63 (1976) 459.
[10] L.W. Cochran and D.W. Forester, Phys. Rev. 126 (1962) 1785.

# II

UPPSALA UNIVERSITY

THE SVEDBERG LABORATORY and
DEPARTMENT OF RADIATION SCIENCES

# PHOTOSENSITIVE MOLECULES FOR CHERENKOV RING IMAGING DETECTORS: TRI ETHYL AMINE AND TETRAKIS DIMETHYL AMINO ETHYLENE

B. Lund-Jensen[1], T. Ekelöf[1], A. Hallgren[1], J. Séguinot[2], J. Tocqueville[2], T. Ypsilantis[2], R. Arnold[3], J.L. Guyonnet[3] and P. Petroff[4]

[1] Univ. of Uppsala, [2] College de France, [3] CRN Strasbourg, [4] LAL, Orsay

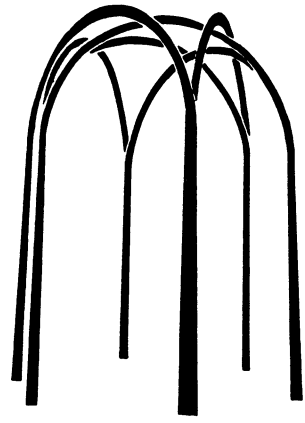

October 1988

TSL - ISV: 17
ISSN 0284 - 2769

# Photosensitive Molecules for

# Cherenkov Ring Imaging Detectors :

# Tri Ethyl Amine and Tetrakis diMethyl Amino Ethylene.

B. Lund-Jensen, T. Ekelöf, A. Hallgren
(University of Uppsala, Sweden)

J. Séguinot, J. Tocqueville, T. Ypsilantis
(College de France, Paris, France)

R. Arnold, J. L. Guyonnet
(CRN Strasbourg, France)

P. Petroff
(LAL, Orsay, France)

## ABSTRACT

Cherenkov ring images have been observed with a drift type single photon detector using TEA or TMAE as photoionizing vapour. Properties of TEA and TMAE are reviewed. The implications of feedback photoelectrons on the detector resolution and the maximum attainable gain have been studied for both TEA and TMAE by comparing the experimental data with Monte-Carlo simulations. In these respects detectors with TEA are found to be superior. Our TEA data are reproduced using a peak quantum efficiency of 60% at 8.2 eV photon energy. The results are used to predict the behaviour of a fast photon detector for Ring Imaging in high rate and high resolution experiments.

( To be submitted to Nuclear Instrumentation and Methods)

## 1. Introduction.

In this paper we present experimental data obtained with a photosensitive gas detector. Vapours of Tri Ethyl Amine (TEA) or Tetrakis diMethyl Amino Ethylen (TMAE) $\{C_2(N(CH_3)_2)_4\}$ were used as the photoionizing molecules to observe Cherenkov ring images produced by relativistic charged particles in a focusing gas radiator. The data, collected in 1981, were in fact the first ring images obtained using the long drift (TPC) imaging technique, which gives ambiguity free two dimensional photon conversion points [1]. Since that time, this technique has been extensively developed [2] and serves as the basis for two large detector systems presently under construction at $e^+e^-$ colliders e.g. DELPHI at LEP/CERN [3] and SLD at SLC/Stanford [4]. All of these developments are made with TMAE because it allows the use of fused quartz windows. The quartz transmission limit of 7.6 eV photon energy is considerably above the TMAE photoionization threshold energy of 5.4 eV. In this energy interval (5.4 to 7.6 eV) many gases and some liquids and solids are transparent (figure 1) allowing a rather large choice of Cherenkov radiator media. Fused quartz is also sufficiently cheap to allow large surface area ($\sim 50\ m^2$) detectors to be built [3, 4].

In contrast, TEA has a photoionization threshold of 7.5 eV and thus cannot be used with fused quartz windows, it requires instead single crystals such as $CaF_2$ (transmission limit 10 eV), NaF (9.8 ev), $MgF_2$ (10.8 eV) or LiF (11.8 eV). Radiator media which are sufficiently transparent to be used with TEA are scarcer and include Helium, Neon, Argon, Nitrogen, Methane and $CF_4$ gases and liquids as well as the above cited single crystals.

The physical properties (vapour pressures, cross sections and quantum efficiencies) of TEA and TMAE are reviewed in the next section of this paper. For TMAE the agreement between the various measurements is rather good [2], however, for TEA the maximum quantum efficiency reported by Holroyd et al [5] disagrees with our preliminary 1981 measurements [6] and with the measurements by Salomon and Scala [7] where they normalize to chemical actinometry. It is this disagreement which initially motivated this analysis. However, the same analysis has also resulted in an unbiased measurement of photon feedback which limits the operation of any multiwire photoionization detector.

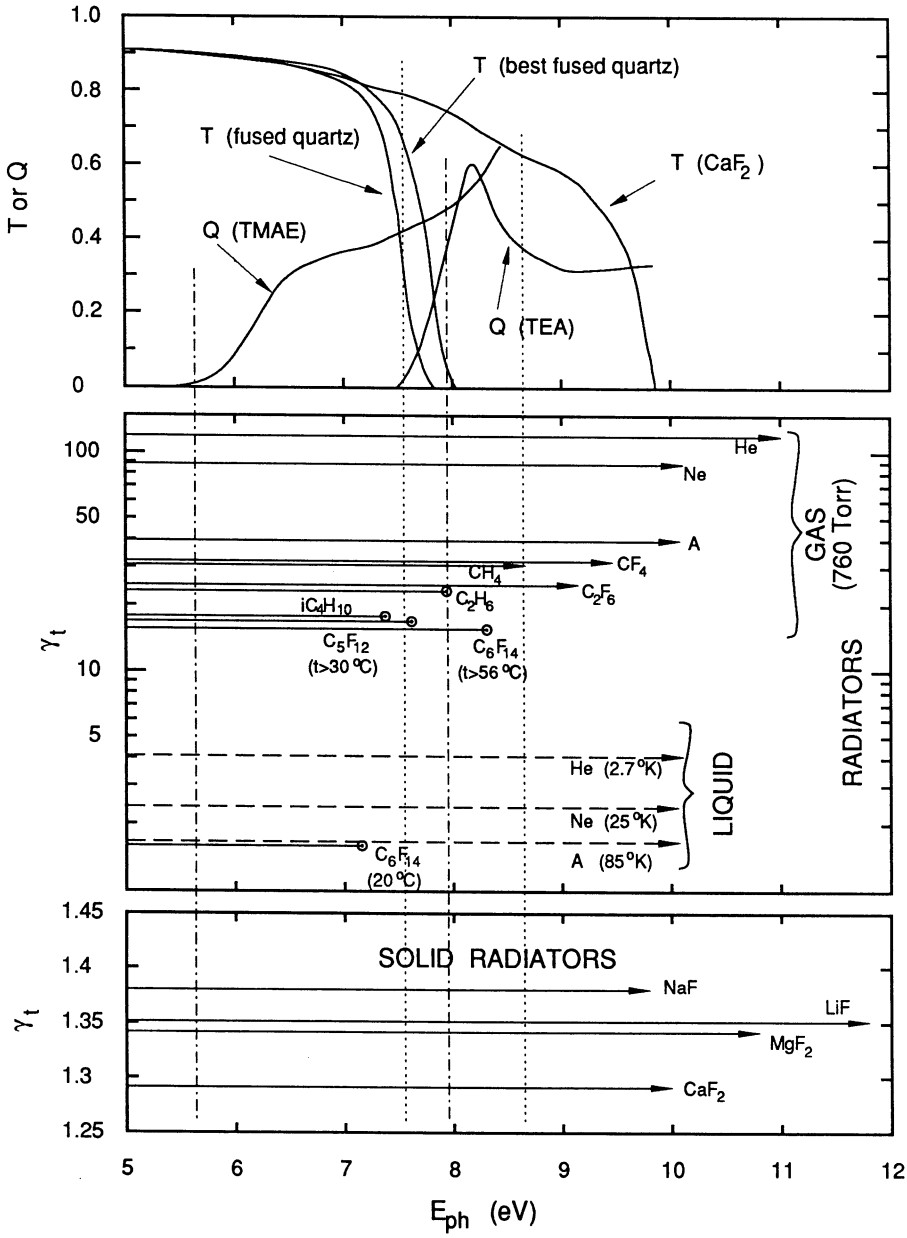


*Figure 1. Quantum efficiencies for TMAE and TEA and window transmissions together with transparency range and Lorenz factor ($\gamma_T$)at the Cherenkov threshold for different radiating media. The media that have a sufficiently high transparency limit to be used with TEA are marked with arrows. $\gamma_t$ for the solid radiators are calculated from the refractive index for 8.2 eV energy photons. The dotted lines show the photon energy range for TEA in Methane gas, while the dash dotted lines show the limits for TMAE with fused quartz.*

The average number of detected Cherenkov photons ($N_{pe}$) is given by the relation

$$N_{pe} = N_0 L \sin^2\theta_c \qquad (1)$$

where L is the radiator length, $\theta_c$ the Cherenkov angle and

$$N_0 = \frac{1}{137\,\hbar c}\int Q(E) \prod_i \varepsilon_i(E)\, dE \qquad (2)$$

is the detector merit factor. The quantity Q(E) is the photoionization quantum efficiency and $\varepsilon_i(E)$ represent both the photon transfer efficiencies e.g. radiator and window transmitivities and the mirror reflectivity and the photoelectron counting efficiencies. An equivalent form of Eq. 2 is

$$N_0 = \frac{Q_{max}}{137\,\hbar c}\int \frac{Q(E)}{Q_{max}} \prod_i \varepsilon_i(E)\, dE \qquad (3)$$

where $Q(E)/Q_{max}$ is the relative spectral distribution for the quantum efficiency. A measurement of $N_{pe}$ in a Cherenkov image allows $Q_{max}$ to be determined (Eq.'s 1 and 3) if $Q(E)/Q_{max}$ and $\varepsilon_i(E)$ are known. The measurements performed with TMAE thus provide a verification of the analysis method since its absolute quantum efficiency is well determined.

In the future, the Ring Imaging Cherenkov (RICH) technique must develop towards "fast" detectors that have a time dispersion of less than 15 ns in order to be operational at the next generation of high luminosity hadron colliders, at which interaction rates of 100 MHz are expected with beam crossings every 15 to 25 ns. Experiments at high luminosity ($> 10^{33}$ $cm^{-2}s^{-1}$) $e^+e^-$ colliders (B meson factories) will require RICH detectors to identify secondary particles from B decay [8]. A "fast" detector will also be advantageous here in order to discriminate against background from beam-gas or beam-pipe interactions in previous and subsequent beam crossings. These requirements exclude the long drift TPC technique which is "slow" having integration times of up to 30 μs [3,4]. The "fast" RICH detector described in section 6, will consist of a thin multi-wire photo-sensitive gas detector, with pad readout, in which created photoelectrons drift perpendicular to the entrance window toward the sense wires. To be "fast" requires that the photon absorption length in the gas must be short as this mainly determines the dispersion of the photoelectron collection time. TEA is a good candidate for such detectors because its photon absorption length is only 0.6 mm at NTP. TMAE would have to be heated to 90 °C to reach such a short absorption length which would make the construction and operation more difficult. For this reason TEA has become, once again, an interesting photosensitive molecule.

Isotropic emission of secondary U.V. photons results from the charge multiplication around the anode wires of a multiwire proportional chamber MWPC. Excitation of atomic states of carbon and hydrogen is caused by the impact of 50 to 100 eV electrons produced near the wire [9, 10]. The emitted U.V. photons may, in turn, ionize the photosensitive gas generating feedback photoelectrons which drift back to the anode wires. This influences the spacial resolution and hence the separating power for particle identification. It diverges for high gains and thus limits the maximum gain attainable in a MWPC detector. This process is discussed in section 3. These effects have been studied in detail for TMAE [2] but a similar study for TEA has not been carried out until this work.

For most of the multiwire detectors developed for the long drift method, the propagation of feedback photons has been limited by using optical screens (blinds) between the sense wires [11,12]. This is imperative when charged particles cross the photosensitive region because the several hundreds of ionization electrons create a large feedback background which interferes with ring image pattern recognition and degrades the Cherenkov angle resolution.

An attractive way of reducing the production of feedback photoelectrons has been proposed by Charpak and Sauli [13] with the use of the Multi-Step Avalanche Chamber (MSAC). This type of detector includes a photon conversion gap, a parallel plane amplification gap, a transfer gap and a second parallel plane amplification gap or a multiwire detector. The transfer gap should be at least 3 or 4 photon mean free paths thick in order to achieve good suppression (>95%) of the photon feedback. The gain necessary to detect the single photoelectrons is partitioned between the two amplifying gaps. Since most feedback photons are created in the second amplifying gap and are absorbed before reaching the first amplifying gap, the subsequent charge developed by feedback photoelectrons is too small for detection. The probability of having further generations of feedback photoelectrons is for the same reason decreased which increases the limit of detector gain. This technique has not yet been implemented with long drift detectors and may provide a natural and simple solution to the photon feedback problem.

At the time of the measurements in 1981, the detectors with blinds had not yet been developed and the photon detector used was simply a multiwire chamber coupled to a drift volume. With these measurements an unbiased (by blinds) comparison of the feedback photoelectron production rate in TEA and TMAE is thus obtained. The results are discussed in section 5 and compared to a Monte-Carlo simulation of the detector response. These results are applied in section 6 to predict the behaviour of a fast RICH detector with pad readout using TEA or TMAE.

## 2. Photosensitive Organic Vapours.

The use of organic vapours as gaseous photocathodes with efficient single photoelectron detection was proposed and demonstrated in 1977 by two of the present authors [14]. Previously such vapours had been used in low pressure ion chambers, operating in a unit gain DC mode, to observe high flux UV sources in space [15]. Benzene ($C_6H_6$) was the first photosensitive gas used in a Multiwire Proportional Chamber (MWPC) geometry in a pulse counting mode. Its room temperature (T = 20 $^0$C) vapour pressure (p = 76 torr) is high and corresponds to a photon mean absorption length $l_{ph}$ = 0.11 mm. The relation between $l_{ph}$ and p is

$$l_{ph} = \frac{k\,T}{p\,\sigma} \qquad (4)$$

which follows from the defining relationship $l_{ph} \cdot n \cdot \sigma = 1$ and the perfect gas law n = p/kT, where n is the gas number density, $\sigma$ the photon absorption cross section, T the absolute temperature and k is the Boltzmanns constant ( k = 1.036 mm·torr·Mb/$^0$K). The benzene photoabsorption cross section is about 35 Mb at 10 eV photon energy [16]. The MWPC geometry, anode to cathode distance of ±4 mm, gas filling of Ar, $CO_2$ and Benzene of ~ 650, 99 and 11 torr respectively resulted in $l_{ph}$ = 0.79 mm hence complete photon absorption in the 8 mm gap [14]. The detectable quantum efficiency of benzene above 10 eV is between 40 and 50% hence it is a superior photoionizing vapour. Its only, but important disadvantage, is its high threshold (9.25 eV) which allows only expensive $MgF_2$ (transparent below 10.8 eV) and LiF (transparent below 11.8 eV) windows.

Photosensitive liquids with lower threshold and sufficient vapour pressure were soon found [17] such as Tri Ethyl Amine [18] ($E_{thresh}$=7.5 eV, p(20 $^o$C)=52 torr, $\sigma \approx$10 Mb) and Tetrakis Methyl Amino Ethylene [19, 20] ($E_{thresh}$=5.4 eV, p(20 $^o$C)=0.35 torr, $\sigma \approx$30 Mb) . Other molecules are of potential interest but have not yet been systematically investigated.

### 2.1 Photoabsorption mean free path and vapour pressure.

The photoabsorption lengths $l_{ph}$ of TEA, Argon gas mixtures were measured versus photon energy. Using equation (4) the measurements were converted to the total cross sections versus wavelength shown in figure 2. In TEA - Methane mixtures the effective region for photoionization is between 7.5 (TEA threshold) and 8.5 eV (methane cutoff) with peak response at 8.2 eV where the cross section is $\sigma$ = 9.7 Mb. This corresponds to $l_{ph}$ = 0.61 mm for Methane bubbling through 20 $^o$C TEA into a MWPC detector at 25 $^0$C. The corresponding time dispersion for collection of the photoelectrons is $\sigma_\tau = l_{ph}/v_D$ where $v_D$ is the electron drift velocity. In predominantly

Methane gas mixtures $v_D \approx 1$ mm/10 ns hence $\sigma_\tau = 6$ ns. A MWPC detector filled with room temperature TEA is thus intrinsically fast.

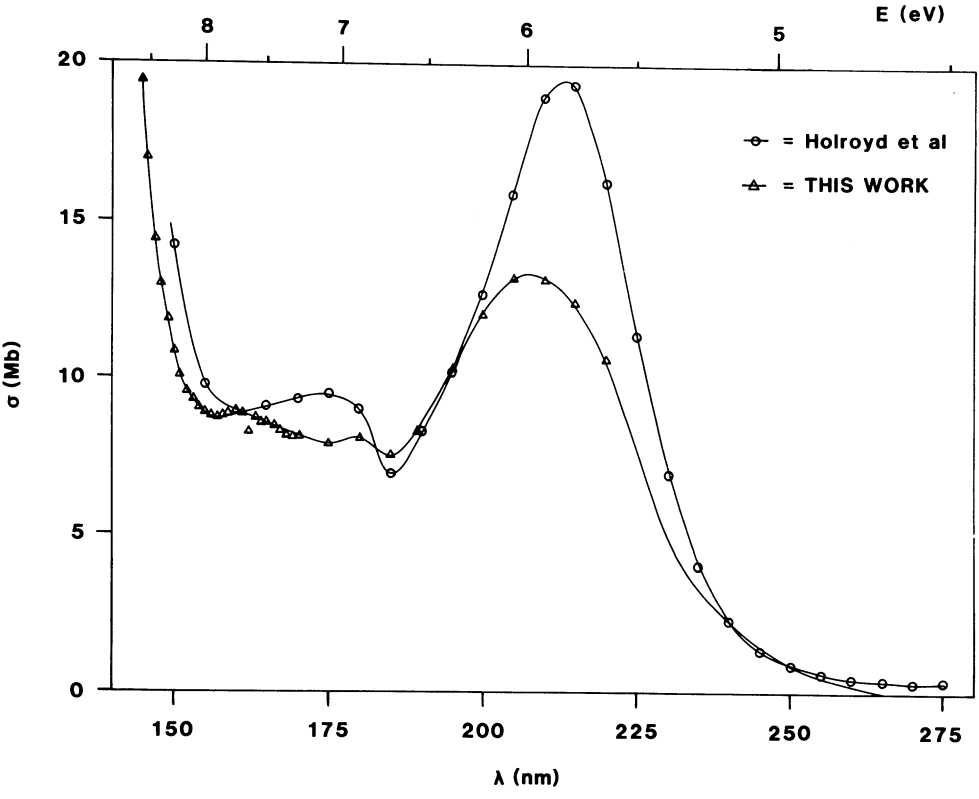


*Figure 2. Total cross section for photon absorption in TEA as a function of the photon wavelength.*

The vapour pressure of TEA versus temperature has recently been measured by Anderson [21] and fitted to the Clausius-Clapeyron equation

$$p = p_0 \, e^{\frac{\Delta H}{R}\left(\frac{1}{T_0} - \frac{1}{T}\right)} \qquad (5)$$

where $\Delta H$ (J mol$^{-1}$) is the heat of vapourisation (at constant pressure) and R=8.3143 J mol$^{-1}$ $^oK^{-1}$ is the molar gas constant, with the result for TEA of $p_0 = 73.2$ torr, $\frac{\Delta H}{R} = 4299$ $^oK$ and $T_0 = 300$ $^oK$.

For TMAE the photoabsorption length $l_{ph}$ versus photon energy E has been measured by Anderson [20], Apsimon et al [22], Ashford et al [23], Holroyd et al [5] and Arnold et al [2]. An example from the latter paper is shown in figure 3 where the absorption coefficient $\mu = 1/l_{ph}$ in an 85 °C cell is plotted versus photon energy at three different bubbler temperatures (23 °C, 50 °C and 80 °C) referenced to T = 300 °K. They are, in the same figure, compared with the Holroyd et al [5] measurements. Reasonable agreement between the measurements is observed.

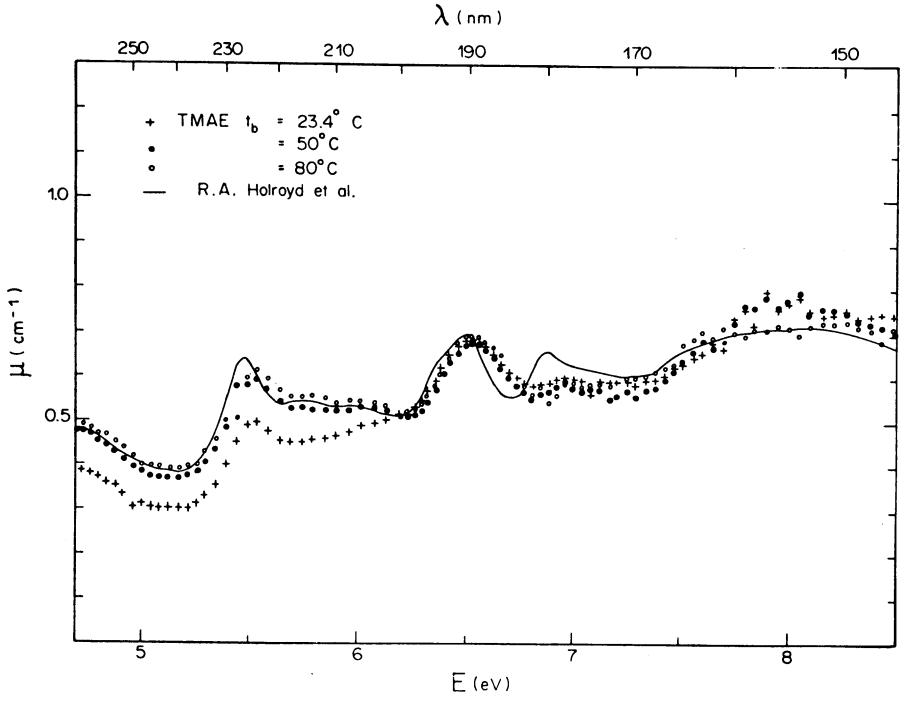


*Figure 3. Variation of the TMAE absorption coefficient μ (cm-1) with photon energy at bubbler temperature of 23, 50 and 80 °C normalized to T = 300 °K. (From Arnold et al [2] figure 9).*

From equations (4) and (5) we may calculate

$$\mu = \mu_0 \, e^{\frac{\Delta H}{R}\left(\frac{1}{T_0}-\frac{1}{T}\right)} \qquad (6)$$

with $\mu_0 = \frac{P_0 \cdot \sigma}{k \cdot T}$. Fits to the data are shown in table 1. It is believed that the first listed coefficient $\mu_0 = 0.73$ cm$^{-1}$ is too large and there is a tendency for the measured heats of vaporization ΔH to decrease as the purification of the TMAE samples is improved (Anderson only used pumping, while Ashford

et al [23] and Arnold et al [2] used washed TMAE as will be described in section 2.3).

*TABLE 1. Fits of measured photon absorption lengths in TMAE as functions of temperature to the parameters of equation 6.*

| $\mu_0$ (cm$^{-1}$) | $\Delta H/R$ ($^0$K) | wavelength (nm) | reference |
|---|---|---|---|
| 0.73 | 6510 | 160 to 180 | Anderson [20] (Xenon light source) |
| 0.56±0.01 | 6214±203 | 170 | Ashford et al [23] |
| 0.48±0.01 | 6023±176 | 200 | - " - |
| 0.53±0.01 | 5614±100 | 200 | Arnold et al [2] |

The vapour pressure measurements (which are of course independent of the photon wavelength) are fitted to the Clausius-Clapeyron parameters of equation (5). Two different measurements by Anderson [20, 21] and one by Giomataris [24] gave $p_0$=0.58, 0.50 and 0.57 torr and $\Delta H/R$ = 6454, 6372 and 6285 $^0$K respectively. The agreement is not bad, with an average $p_0$ = 0.55 torr and $\Delta H/R$ = 6370 $^0$K. From the early data [20] a cross section $\sigma$ = 41 Mb may be calculated whereas later data [23] give $\sigma$ = 29 Mb at 170 nm, $\sigma$ = 27 Mb at 200 nm and data [2] give $\sigma$ = 30 Mb at 200 nm. The later data seem to be in agreement with $\sigma \approx 30$ Mb.

## 2.2 Quantum efficiency.

The spectral shape of the quantum response of TEA has been measured by Comby & Ypsilantis (private communication quoted in references [18, 25]), Comby et al [26], Ekelin & Fransson [27, 28] and Holroyd et al [5] as shown in figure 4, where the relative quantum efficiency $Q/Q_{max}$ (normalized to 1 at maximum) has been plotted versus photon wavelength. All the measurements (except Ekelin & Fransson) are in Argon - TEA mixtures hence without competitive photon absorption until the Argon transmission limit of 110 nm. The measurement of Ekelin & Fransson [27, 28] was with a Methane - TEA mixture and the drop of quantum efficiency (below 150 nm) reflects the onset of photoabsorption in Methane. A comparison of the three curves beyond 145 nm shows a rough agreement between Comby & Ypsilantis [18, 25] and Holroyd [5] while Comby et al [25] shows little quantum efficiency beyond 145 nm. This is not in agreement with the Ring Imaging data (which will be discussed later) which shows that a Helium - TEA detector has more response than a Helium - Methane - TEA detector in the ratio 3 to 2. The onset of sensitivity is earlier in the Comby and Holroyd distributions with peak response at 153 nm and 152 nm

respectively. The agreement amongst these distributions is poor indicating uncontrolled errors in the measurements.

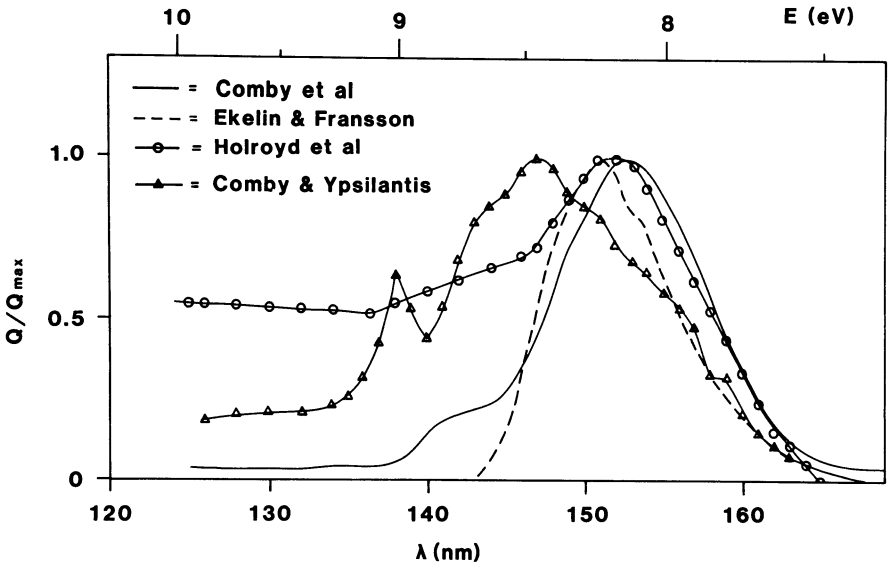


*Figure 4. The relative quantum efficiency ($Q/Q_{max}$) of TEA as functions of the photon wavelength as measured by Comby & Ypsilantis [18, 25], Comby et al [26], Ekelin & Fransson [27, 28] and Holroyd et al [5].*

The situation with regard to the absolute scale ($Q_{max}$) of the TEA quantum response is also poor. Holroyd et al [5] give $Q_{max}$=33% with the absolute efficiency established relative to the known Benzene and Cis-2-butene quantum efficiencies. Data from Ring Imaging detectors seem to give a considerably higher value for $Q_{max}$. The experiment of Charpak et al [29] with an Argon - TEA filled Multi Step Avalanche Chamber (MSAC) gave the Cherenkov quality factor $N_0$=80 $cm^{-1}$ and Ekelöf et al [1] again with a MSAC found the Cherenkov quality factor $N_0$=90 $cm^{-1}$ with Argon - TEA filling of the detector and $N_0$=60 $cm^{-1}$ with Argon - Methane - TEA filling. These data translate to $Q_{max}$ between 60 and 65 % using the spectral shapes of Comby & Ypsilantis [18, 25] and Ekelin & Fransson [27, 28]. The later experiment of Mangeot et al [30] with MSAC detectors filled with either He - TEA or He - Methane - TEA gave $N_0$=45 $cm^{-1}$ and 42 $cm^{-1}$ in real beam running conditions. The expected values (using measured window transmissions, mirror reflectivities and radiator gas transmission) are

$N_0$=58 $cm^{-1}$ and 45 $cm^{-1}$ respectively using the spectral shape of Comby & Ypsilantis [18, 25] and $Q_{max}$=65 %. The data was interpreted to indicate that the MSAC efficiency for single photoelectron counting was the ratio of the measured and expected $N_0$ i.e. 78% for He - TEA and 93 % for He - $CH_4$ - TEA mixtures. An equally valid interpretation would assume 100% single electron efficiency for He - $CH_4$ - TEA filling and $Q_{max}$=60 %. In this case the He - TEA single electron efficiency is 85 % which is consistent with their reported single electron amplitude distributions for this mixture. One Ring Imaging experiment [25] gave a value of $Q_{max}$=37 % however this result depended on the unmeasured assumption that the radiator gas had only 3 ppm of oxygen contamination. A level of 12 ppm oxygen would have lead to the conclusion $Q_{max}$=60 % hence the data [25] cannot be regarded as being in contradiction with the other Ring Imaging data [1, 29, 30].

The method of chemical actinometry was used by Solomon and Scala [7] as normalization to determine the absolute quantum efficiency of various molecules at 147 nm wavelength. The absolute photon flux of a low pressure Xenon lamp (99% at 147 nm and 1% at 130 nm) was measured in a total absorption cell filled with low pressure (6 to 14 torr) of Hexa Fluoro Acetone (HFA) gas. Photolysis of HFA produces one molecule of CO and one of $C_2F_6$ for each incident 147 nm photon [31]. On this basis, they [7] measured the number of moles of CO gas produced to detemine the integrated photon flux. Quantum efficiencies Q(147nm) for TEA, Tri Methyl Amine, Di Propyl Amine and Tetra Methylene Sulfide of 0.46±.01, 0.386±.008, 0.096±.005, 0.15±.007 and 0.10±.005 respectively were found. The spectral shape of figure 4 for TEA from Holroyd et al [5] gives $Q(147nm)/Q_{max}$ = 0.73 which with the actinometric value Q(147nm) = 0.46 predicts $Q_{max}$ = 0.63 in contradiction with the Holroyd et al [5] value of $Q_{max}$ = 0.33 but in agreement with the Ring Imaging data [1, 29, 30]. The spectral shape of Comby et al [26] shows $Q(147)/Q_{max}$ = 0.45 hence Q(147nm) = 0.46 predicts a value for $Q_{max}$ = 1.02±.02. Such a large efficiency is inconsistent with the Ring Imaging data [1, 29, 30]. This distribution is considered very unlikely because it predicts too little response below 145 nm. The Ring Imaging data [1, 29, 30] show about 33% of the total response to be below 145 nm as does the Holroyd et al [5] distribution. The distribution of Comby and Ypsilantis [18, 25] is better with regard to the 145 nm region however it peaks at 147 nm whereas all the others peak at 156 nm. This distribution was obtained in the earliest days of TEA detectors and the data was not published so that the experimental details could be examined. It is believed by one of the authors (Ypsilantis) that this data should be superceeded by the Holroyd et al [5] and Ekelin & Fransson [27, 28] distributions even though these show some differences (≈2nm) near threshold. We also believe, however, that the 33 % maximum quantum efficiency of Holroyd et al [5] is wrong and is closer to 60 % as shown by the present work and other Ring Imaging data [1, 29, 30].

For TMAE the spectral shape of the quantum efficiency has been measured by Nakato et al [19], Ekelin & Fransson [27, 28] and Holroyd et al [5]

as shown in figure 5. The measurements of Nakato et al are limited in energy range (E<7.3 eV) whereas the Ekelin & Fransson measurements extend to 8.5 eV, the Methane absorption limit. The agreement amongst these distributions is reasonable. The absolute normalization of figure 5 has been obtained by Holroyd et al [5] in comparison to the known Benzene and Cis-2-Butene efficiences. The normalization of the Ekelin & Fransson and Nakato et al data has been described by Arnold et al [2] from Ring Imaging measurements of the Cherenkov quality factor $N_0$=95 $cm^{-1}$ in a Methane - Ethane - TMAE filled detector with fused quartz windows. The agreement, in this case, seems good whereas for TEA the agreement is bad. The source of this inconsistency is not understood.

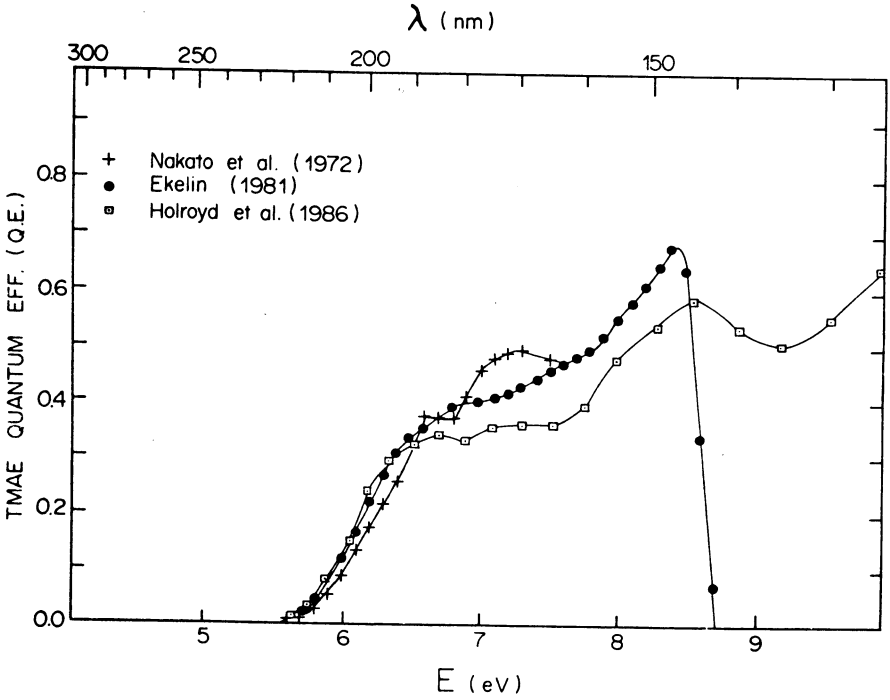


*Figure 5. The quantum efficiency (Q) of TMAE as a functions of the photon energy as measured by Nakato et al [19], Ekelin & Fransson [27, 28] and Holroyd et al [5].*

### 2.3 Purification and Use.

TEA is a stable material in air and no special precautions have to be observed in its use. We have used Fluka AG puriss p.a. quality TEA with

stated purity > 99.5 %. Electron drift over the detector surface of 13 cm showed no effects which could be attributed to electron pickup due to TEA or impurities.

For TMAE, on the other hand, certain precautions must be observed in its use since it oxidizes violently when exposed to air. The transfer of the liquid TMAE into a bubbler was effected in a glove box filled with dry Nitrogen. The TMAE liquid was pumped for a period sufficient to reduce the volume by 10 %. In later work [2] the TMAE was washed three times (under nitrogen atmosphere) with triply distilled and de-ionized water in a separating funnel with the immiscible heavier water fraction drained off each time. It was then dried by the passage of the liquid TMAE through a silicagel bed and then de-aerated by bubbling pure methane through the liquid TMAE. This treatment allowed electron drift through a Methane - TMAE (≈1 torr) mixture for distances of 1.7 m with a photon absorption length of more than 10 m. This corresponds to an electron lifetime of greater than 160 μs.

# 3. Multiwire Gas Detectors: Counting Efficiency and Feedback Photoelectron Production.

## 3.1 Counting efficiency.

It was demonstrated by Ekelöf et al [1] that single-stage multiwire chambers are efficient for single photoelectron counting using either pure Methane, Ethane, Isobutane, or mixtures thereof, as carrier gases for the photosensitive organic vapour.

The distribution of the induced charge (q) on anode wires is of the Polya type [32]:

$$P(q) = \frac{1+\theta}{\bar{q}\,\Gamma(1+\theta)} \left( \frac{(1+\theta)\,q}{\bar{q}} \right)^{\theta} e^{-\frac{(1+\theta)}{\bar{q}} q} \qquad (7)$$

where $\bar{q}$ is the mean charge and $\theta$ is a parameter which varies linearly with $\bar{q}$. The measurement of Arnold et al. [33] have been fitted to obtain ($\theta = 0.0113 \cdot \bar{q} - 0.095$, $\bar{q}$ in fC). Here the charge q is the true charge, whereas in [33] q was the measured charge which corresponds to only 60% of the true charge because of the short time constant (10ns) of the input preamplifier used. Their measurements were made using a multiwire detector with cylindrical cathodes made of 2 mm inner diameter stainless steel tubes. The photoelectrons were focused through a 0.8 mm slit in the cylindrical wall parallel to the wire. This detector was operated with a Methane - Ethane - TMAE gas mixture with average gains ( $\bar{g} = \bar{q}/e$ ) of up to $5 \cdot 10^5$ before instabilities occurred due to feedback photoelectrons. The detector used for the measurements in the present paper has a different geometry and, as will be shown, $\bar{g} \approx 7 \cdot 10^5$ in a Methane - TMAE mixture ($l_{ph}$=15 mm) and $\bar{g} \approx 1.9 \cdot 10^6$ in a Methane - TEA mixture ($l_{ph}$=6 mm) can be reached. Extrapolating from the linear fit this corresponds to $\theta \approx 1.2$ and $\theta \approx 3.3$ respectively. For these values of $\theta$ the Polya distribution is peaked with the peak moving to higher q and becoming narrower with increasing gain. For average gains below $5 \cdot 10^4$ then $\theta \sim 0$ and the distribution becomes exponential (i.e. of the Furry type):

$$F(q) = \frac{1}{\bar{q}} e^{-q/\bar{q}} \qquad (8)$$

Predominantly Argon gas mixtures exhibit this exponential distribution and are therefore less suitable for single photoelectron detection.

The discriminator threshold, for the tests reported here, corresponds to a gain of $2.2 \cdot 10^5$. With a maximum average gain of $7 \cdot 10^5$ for Methane - TMAE this threshold results in a counting efficiency of ~ 82 %, while in

Methane - TEA full detection efficiency (>99.5%) with a comfortably long plateau is obtained. With the more modern detection electronics of Arnold et al [33] an r.m.s. noise level corresponding to 8000 electrons was observed when the anode wires were coupled to the readout electronics. With a discriminator level set 2 to 3 times above the noise level to $2 \cdot 10^4$ almost full detection efficiency (>95%) is achieved for $\bar{g} \approx 3 \cdot 10^5$.

### 3.2 Feedback photoelectron production.

During the avalanche process around the anode wires, atomic levels in the Carbon and Hydrogen are excited (by electron collisions with molecules of the detector gas) and quickly de-excite by isotropic photon emission. The photons from Hydrogen (Lyman $\alpha$) have 10.2 eV energy and are strongly absorbed in Methane, Ethane and Isobutane. The photons from Carbon have 6.42, 7.48 and 7.94 eV energy with relative intensities of about 3 : 5 : 3 [34]. Methane is transparent to all of these photons while Ethane weakly absorbs the 7.94 eV line and Isobutane strongly absorbs the 7.94 eV line and weakly absorbs the 7.48 eV line. The photons which can ionize molecules of TMAE (all lines) or TEA (only the 7.94 eV line) in the carrier gas create secondary photoelectrons which at later times and on the same or neighbouring wires create new avalanches.

The mean production rate $\alpha$ of feedback photons per unit charge q developed in the avalanche has been measured by Arnold et al [33] and found to be constant (independent of detector gain) with a value* of $\alpha = 0.041$ photons/fC $= 6.5 \cdot 10^{-6}$/e. This corresponds to one feedback photon in an avalanche of gain $g = q/e = 1/\alpha e = 1.5 \cdot 10^5$. The number of secondary photoelectrons per avalanche $N_{spe} = \alpha\, q\, \bar{D}\, \bar{Q}$, where $\bar{D}$ is an efficiency factor given by the detector geometry and gas transmission, and $\bar{Q}$ is weighted average of the quantum efficiency (TEA or TMAE) at the feedback photon energies with weights corresponding to their relative intensities. Instability sets in when $\bar{N}_{spe} = \alpha\, \bar{q}\, \bar{D}\, \bar{Q} = 1$. For TMAE in Methane $\bar{Q}=0.44$ whereas for TEA, which is insensitive to the 6.42 and 7.48 eV feedback photon lines, $\bar{Q}=0.10$, hence a detector with TEA can be operated at ~4.4 times higher gain than the same detector with TMAE. In the present work the detector was operated with a longer photon mean free path for TMAE than TEA thus reducing this factor.

There are two different observed effects caused by photons emitted in the avalanches, both deteriorating the separation power for particle identification:

i) Photons which propagate in the same or adjacent wire cells and produce secondary avalanches practically synchronous with the

* The value given by Arnold et al in reference [33] is the number of feedback photoelectrons per unit charge measured after filtering by the preamplifier. This is converted to the number of feedback photons by Dracos [35].

primary avalanche. These distort the single photoelectron charge distribution, create clusters of hit wires and spread the induced cathode charge distribution, biasing the determination of its centroid when detected by cathode strips or pad arrays.

ii) Photons converting such that they produce separate secondary avalanches at later times on the same or adjacent wires. These contribute to the ring image background.

In order to limit the above effects it is obvious that the production rate of feedback photoelectrons ( $\alpha \cdot \bar{q} \cdot \bar{D} \cdot \bar{Q}$ ) must be kept as low as possible. This can be achieved by operating at lower gain, which implies the use of low noise electronics, or by using a detector gas mixture which absorbs the Carbon emission line photons of energies higher than the maximum transmission of the radiator or the window. This latter reduction is possible for TMAE only if the radiator or window transmission limit is below 7.94 eV otherwise Cherenkov photons are lost. With present electronic thresholds the gain used for a detector with TMAE will have to be a compromise between the amount of feedback photoelectrons and the detection inefficiency. With TEA however, the gain can be sufficiently high to achieve full detection efficiency with a tolerable amount of feedback. These implications on the choice of TEA or TMAE will be illutstrated further in the discussion about fast RICH detectors in section 6.

# 4. Experimental setup and data analysis.

## 4.1 Experimental setup.

Measurements were made at the CERN Proton Synchrotron with a beam of negatively charged particles having momenta which were adjustable within the range of 5 to 20 GeV/c. The general layout of the setup is shown in figure 6. The coincidence of the four scintillators $S_1$, $S_2$, $S_3$ and $S_4$ defined the passage of a charged particle through the radiator gas, where the 5 mm diameter $S_1$ and $S_3$, placed 3 m apart, restricted the acceptance. The Cherenkov light emitted along the particle trajectory was focused by a spherical mirror with focal length f=1 m into a ring image inside the drift volume of the photon detector. The beam particles passed outside the photon detector and at a distance (y) of 165 mm from the centre of curvature of the spherical mirror. The imaging error caused by the 8.2 % impact parameter (y/2f) [36] was negligible, however the incidence angles of the photons gave a parallax error to the image due to photons converting at different depths. By letting the beam pass outside the photon detector the large signal from dE/dx ionization in the detector was avoided.

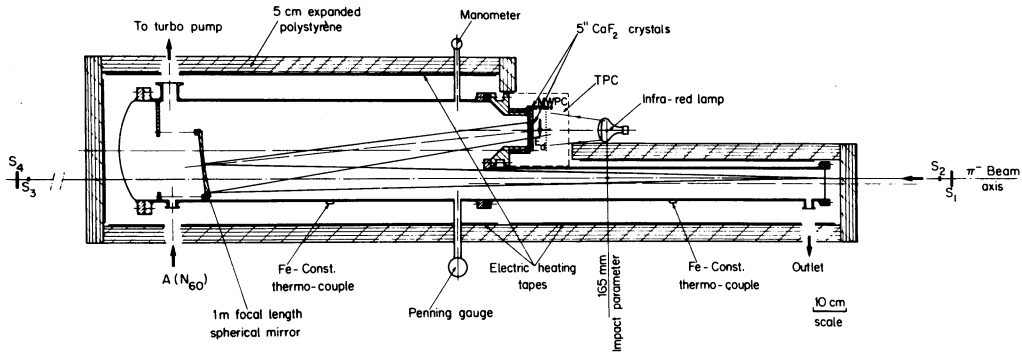


*Figure 6: Layout of the experimental setup.*

### 4.1.1 The gas radiator.

In the measurements reported here Argon gas was used as the radiator medium. The path length between the entrance window of the ~80 liter stainless steel radiator tank and the centre of the spherical mirror was 1.87 m. The tank, prior to use, was pumped (with photon detector mounted in place) to $10^{-5}$ mbar with a turbo-molecular pump and degassed for about 12 hours. The radiator was then filled with Argon gas through a reduction valve to a constant pressure of 1.13±0.03 bar and flushed at a flow rate of 40 l/h. A measurement performed with a monochromator dictated the use of high purity Argon gas (quality N60, i.e. ≤ 1 ppm impurities) in order to achieve better than 99% transparency over 1 meter. The heating, used to

prevent condensation of TMAE in the detector, was regulated to keep the radiator at a constant temperature of 35±1 °C to avoid a variation of the refractive index. The radiator was not heated during the TEA runs.

### 4.1.2 Photon detector and electronics.

The photon detector (shown in side-view figure 7) and the electronics have been described extensively in reference [28]. The detailed tests reported in this reference exhibited the difficulties in obtaining a uniform electron collection in a thin photosensitive drift volume, which was due to the build up of surface charge on the detector window. This determined a particular detector structure which will be briefly recalled.

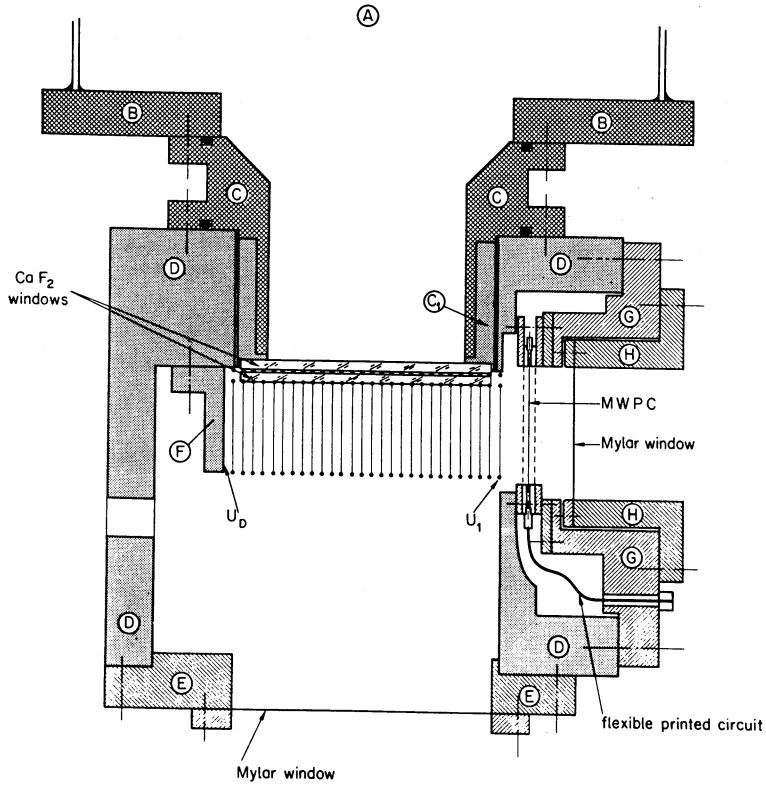


*Figure 7. Details of the photon drift detector: A is the gas radiator volume with end flange B (stainless steel) and the gas container extension C (stainless steel) and C1 (Araldite, glued to C). The outer entrance window is glued to the Araldite extension C1. D is the support box (Araldite) for drift gap and MWPC. E is the rear closure for the support box with mylar window. F is the drift volume with field shaping electrodes and the inner entrance window. The potentials $U_D$ at the far side and $U_1$ at the side nearest to the MWPC was divided in equidistant steps defining the parallel electric drift field. G is the MWPC array with wire mesh cathodes and wire anodes. H is the closure of the MWPC array with mylar window.*

#### 4.1.2.1 The drift volume.

It was found [28] that in order to obtain a sufficiently uniform electric drift field inside the drift gap it was necessary that both sides of the entrance window dielectric be polarized with the same electric field as in the drift gap. This required field shaping electrode wires on both sides of the window preventing charge buildup on the dielectric surface. Since a 5 inch diameter $CaF_2$ window was already glued in position to ensure gas tightness, it was difficult to implement electrodes on both its surfaces. A second window was thus installed in mechanical contact with an added set of field shaping wires between the two windows. As a consequence, the absorption in the second window caused an additional loss of photons reaching the detector gas. Of course, for the new generation of photon detectors such losses can be avoided by correctly designing the field shaping of the drift volume.

The drift gap consisted of a U shaped frame of glass-fibre reinforced epoxy* around which were wound 100 μm diameter gold-plated tungsten-wire loops with a spacing of 2.54 mm. The legs of the U were covered with a 0.1 mm thick polyamide (Kapton** ) foil on which conductive strips, 0.1 mm wide with 2.54 mm pitch, had been etched using the printed circuit technique. These conductive loops and strips were put at fixed linearly increasing potentials from $U_d$ at the far end to $U_1$ at the end nearest to the MWPC detector. The surface area of the drift gap was 140 mm (x) times 130 mm (y) and its depth (z) was either 15mm or 45 mm in two different versions.

#### 4.1.2.2 The photosensitive gas mixture.

The Methane gas used in the photon detector was bubbled through either TEA or TMAE. The TEA bubbler was kept at a temperature of 4 $^0$C and the preferred partial pressure adjusted by allowing only a part of the Methane gas to pass through the bubbler. When using TMAE, all methane gas passed through the bubbler and the partial pressure was adjusted by changing the regulated temperature of the heated bubbler.

#### 4.1.2.3 The MWPC and readout electronics.

The MWPC consisted of a picket fence of 42 short (60 mm long, 20 μm diameter) wires arrayed in the x coordinate with 2.54 mm spacing . The two cathode planes placed at ±3.2mm distance from the wire array, were made of a woven mesh of 50 μm wires with 500 μm spacing.

The signals from the sense wires were preamplified, with amplifiers mounted on the detector, and then transferred to the counting area for further amplification and discrimination. The resistance to ground of the

---

* Quality 4411W from Stesalite AG, Switzerland.

** Kapton is a registered trade-mark of DuPont de Nemour.

sense wires was $R_i$=1.77 kΩ with a measured stray capacitance of $C_i$=16 pF, hence an entrance filter time constant of 28 ns. The discriminator threshold was, according to a laboratory measurement, set for a 177 μV (i.e. 0.1 μA through 1.77 kΩ) signal on the sense wire. Calculating the voltage response of the MWPC with the preamplifier entrance filter using the relation

$$v(t) = \frac{e\,g\,C}{4\,\pi\,\varepsilon_0\,C_i} \int_0^t \frac{e^{-\tau/R_iC_i}}{t + t_0 - \tau}\,d\tau \qquad (9)$$

with the constant

$$t_0 = \frac{\pi\,\varepsilon_0\,d^2}{C\,U_c\,\mu} \qquad (10)$$

where g is the MWPC gain, $C = \frac{2\,\pi\,\varepsilon_0}{(\pi a/s - \ln(2\pi d/s))}$ is the capacitance per unit length of the MWPC (pF/m), $\varepsilon_0$ is the dielectric constant of free space, s is the wire spacing (0.254 cm), a the anode to cathode distance (0.32 cm), d the wire diameter (0.002 cm), $U_c$ the anode-cathode potential (3.98 kV) and μ is the mobility of the positive ions (2.26 $cm^2/V{\cdot}s$). For these values we calculate C=8 pF/m, $t_0$=1.5 ns and $v_{max} = 12{\cdot}10^{-4} \cdot g$ (μV) at t = 15 ns. A threshold of 177 μV thus corresponds to $g=1.48{\cdot}10^5$ i.e. a charge of 23.6 fC. The laboratory measurements on the electronics has shown a 25 % R.M.S. variation of the adjusted threshold while the crosstalk to nearby channels was measured to be about 3%.

A Drift Time Recorder system (CERN DTR 247, 9 bits) digitized the detection time of the discriminated signals from the wires relative to the delayed trigger. The maximum time range was 2048 ns with 4 ns time bins. The DTR system had a multi-hit capability with a minimum of 60 ns between successive pulses on the same channel.

### 4.2 Data analysis.

The position of the centre of the ring image depends only on the particle direction [36]. With the maximum divergence of the beam particles given by the 5 mm diameter scintillators, this position is localized within a 3.4 mm spot. A first rough estimate of the position of the average centre was obtained by making an eye-fit to online plots of ~100 overlayed images. An annular cut around this centre was applied, requiring that digitizations counted as Cherenkov photo-electrons were situated between a minimum and a maximum radius. The ring image centre was then calculated by fitting a circle to the detected photo-electrons for each event. A least squares fit was made in which the deviation in the square of the radius (r) was minimized. The radius (r) and centre ($x_c$,$y_c$) were free parameters thus requiring at least

three coordinates for the fit. The reason for using $r^2$ instead of r, is that an analytical solution can be found:

$$x_c = \frac{\sigma_{yy}(\sigma_{xx^2} + \sigma_{xy^2}) - \sigma_{xy}(\sigma_{yx^2} + \sigma_{yy^2})}{2(\sigma_{xx}\sigma_{yy} - (\sigma_{xy})^2)} \tag{11}$$

and

$$y_c = \frac{\sigma_{xx}(\sigma_{yy^2} + \sigma_{yx^2}) - \sigma_{xy}(\sigma_{xy^2} + \sigma_{xx^2})}{2(\sigma_{xx}\sigma_{yy} - (\sigma_{xy})^2)} \tag{12}$$

where $$\sigma_{uv} = \overline{u \cdot v} - \overline{u} \cdot \overline{v} = \frac{\sum_{i=1}^{n} u_i \cdot v_i}{n} - \frac{\sum_{i=1}^{n} u_i \cdot \sum_{i=1}^{n} v_i}{n^2} \tag{13}$$

from which the radius can be calculated as

$$r = \sqrt{\overline{(x - x_c)^2} + \overline{(y - y_c)^2}} = \sqrt{\frac{\sum_{i=1}^{n} [(x_i - x_c)^2 + (y_i - y_c)^2]}{n}} \tag{14}$$

The average fitted centre $(\bar{x}_c, \bar{y}_c)$ was used both for an improved cut when reiterating the circle fits, and for calculating the radii of individual coordinates (which is then possible also for events with less than three coordinates). Images from single particles are shown in figure 8 together with annular cuts and fitted circles.

Although some feedback photoelectrons give rise to clusters (as seen in figure 8) and might be eliminated to improve the resolution, others are indistinguishable from Cherenkov photoelectrons. It is thus clear that the understanding of the efficiency and resolution of the detector can only be obtained by a comparison with simulations. Since a like fraction of events with high multiplicities outside the cuts and with large cluster-sizes was found both in data and in the simulations, no cluster reduction nor any elimination of noisy events was made in the analysis in order to avoid a bias towards low photon feedback multiplicities.

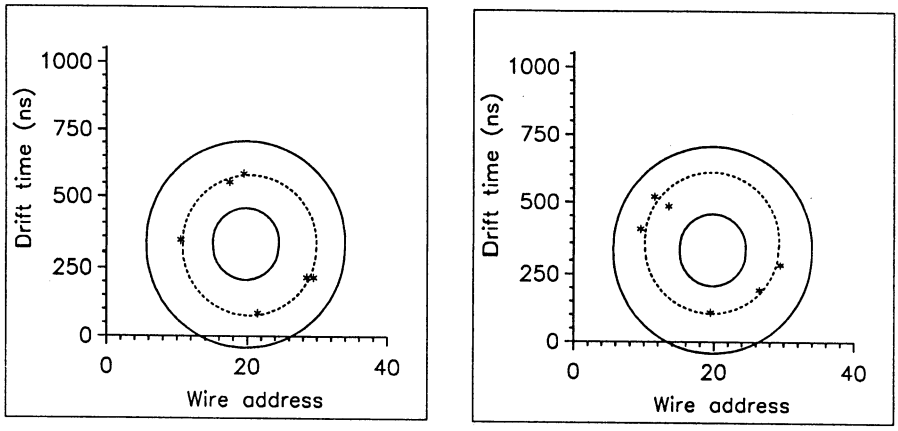


*Figure 8. Single Cherenkov ring images obtained with Methane - TEA gas mixture at gain≈1.65·10⁶. The solid circles are the outer and inner radius of the annular cuts. A circle (dashed) is fitted to the signals inside cuts. Feedback photoelectrons and crosstalk give rise to clusters as can be seen in the first event. The second event illustrates the difficulty in determining which are feedback photoelectrons.*

### 4.3 Monte-Carlo simulation.

A Monte-Carlo simulation program for Cherenkov ring images including the detector response was developed.

Particles (e μ π K and p) corresponding to the beam contents were generated with a given momentum. The variation in incident particle trajectories was obtained by generating uniform distributions in the 5 mm diameter scintillators.

The number of generated Cherenkov photons was taken from a Poisson distribution with an average $\bar{N}_{gen}$ given by

$$\bar{N}_{gen} = \frac{\alpha}{\hbar c} L \int_{E_{min}}^{E_{max}} \left(1 - \frac{1}{\beta^2 n^2(E)}\right) dE \qquad (15)$$

integrated between the photon energy limits 5.4 to 8.8 eV for TMAE and 7.3 to 8.8 eV for TEA. The photons were given energies with a distribution in accordance with the integrand. L is the radiator length (1.87 meters), β the particle velocity and n(E) the refractive index given by the Lorentz equation

$$\frac{n^2 - 1}{n^2 + 2} = C \cdot f(E) \qquad (16)$$

where $C = \frac{4\pi}{3} r_B^3 \frac{N_A \cdot \rho}{M}$, $r_B$ is the Bohr radius, $N_A$ is Avogadros number, M is the molecular weight and $\rho$ is the radiator density, hence for an ideal gas $C = 1.668 \cdot 10^{-5} \cdot p(bar) \cdot (273.16/T(^oK))$. The energy dependent molar refractivity function f(E) is obtained by a Sellmeier equation fit $f(E) = \sum_{i=1}^{2} \frac{F_i}{E_i^2 - E^2}$ to the experimental data [37]. For Argon gas the parameters of the Sellmeier equation are $E_1$=13.08 eV, $E_2$=24.22 eV, $F_1$=278.1 $eV^2$ and $F_2$=3694. $eV^2$.

Both the azimuthal angle of the photons and the creation point along the particle trajectory were generated with uniform distributions.The photons were tracked from the emission point, reflected by the mirror and traced back through the radiator gas, the windows and into the drift volume taking the refractive indicies, the transmissions ($T_i(E)$) and the mirror reflectivity into account. The mirror reflectivity and the transmissions of the two $CaF_2$ windows had previously been measured in the laboratory and are shown in figure 9. The photons that reached the drift volume converted into photo-electrons with a probability given by the quantum efficiency Q(E) as is also shown in figure 9. The spectral shapes measured by Ekelin and Fransson [27, 28] were used for both the TEA and TMAE quantum efficiencies. The absolute normalization of the TMAE quantum efficiency of Arnold et al [2] (70% at 8.5 eV) was made with TMAE that was purified by washing. For the present tests the TMAE was purified by pumping only. To obtain an agreement with the experimental data a normalization of 60% at 8.5 eV had to be used. The difference can be explained by the lower purity of the TMAE used in the present measurements. The 60% agrees however with the 58% reported by Holroyd et al [5]. The absolute normalization of the TEA quantum efficiency was left as a parameter to be fitted to the data.

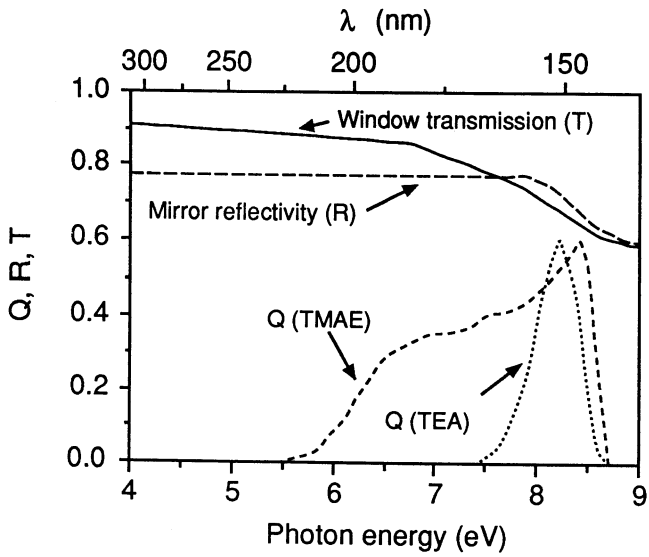


*Figure 9. The transmission (T) of the 5mm thick $CaF_2$ windows (the curve shown is for a single window) and the mirror reflectivity (R) as measured with a monochromator prior to the beam measurements. The TEA and TMAE quantum efficiencies (Q) (in methane gas) which are used in the simultions are also shown. The TEA curve is normalized to 60% at its maximum.*

The conversion point inside the photosensitive gas of the drift region was given by an exponential attenuation with an interaction distance $l_{ph}$. A photoelectron at point (x,y) was then drifted a distance y to the MWPC wire plane (at y=0) in a constant electric field $E_D$=0.6 kV with a drift velocity as measured prior to these tests, $v_D$ = 96±1 μm/ns ($CH_4$ - TEA) and $v_D$ = 99±1 μm/ns ($CH_4$ - TMAE). Longitudinal diffusion ($\sigma_L$) and distortions due to field inhomogenities together with time binning ($\sigma_{0t}$) were included through the relation $\sigma_y^2 = \sigma_{0t}^2 \cdot v_D + \sigma_L^2 \cdot y$ with the measured values [28] of $\sigma_{0t}$=10.2 ns and $\sigma_L$=235 μm/cm$^{-1/2}$. Transverse diffusion ($\sigma_T$) and wire binning were similarly included via the relation $\sigma_x^2 = \sigma_{0x}^2 + \sigma_T^2 \cdot y$ with $\sigma_{0x}=s/\sqrt{12}$ and $\sigma_T$ = 235 μm/cm$^{-1/2}$ where s is the wire spacing (2.54 mm). The generated point (x,y) was then smeared with variances ($\sigma_x$,$\sigma_y$) respectively. The induced charge (q) on the wires was generated from the Polya type distribution (eq. 7) as described in section 3.1. The signal was accepted if it was larger than the threshold of the electronics, corresponding to a total induced charge of 35 fC. This threshold value was determined from the TMAE data, however, it is somewhat larger than the 24 fC previously assumed. The earlier value was based on a measurement with injected electronic pulses where pulse shape differences might explain the discrepancy. The TEA data, being obtained at higher detector gains, are not sensitive to these differences in electronic threshold. The measured 25% r.m.s. variation of the threshold value was included.

For each avalanche, feedback photons were generated according to a Poisson distribution with average $\bar{n}=\alpha \cdot q$ ($\alpha=0.041/fC$). These photons could convert, as described above, and give feedback photo-electrons which could again give more feedback photons. The mesh planes were taken into account for the transmission of photons. A photo-cathode effect from TMAE adsorbed on the mesh planes was included (Arnold et al [33]), while no such effect was used in the case of TEA. Instability of the detector was defined to occur whenever more than 500 avalanches above threshold, due to a large amount of feedback photoelectrons, were generated for an incident particle event.

The measured 3% electronics crosstalk between adjacent channels was included in the simulation. A uniformly distributed background corresponding to noise from the electronics and other indistinguishable sources was generated with an average of 0.75 and 1.5 signals per trigger for the TEA and TMAE measurements respectively. Background ring-images from beam-particles passing close in time to the triggering particle were simulated corresponding to a measured rate of $\sim 10^4$ particles per 300ms burst.

Finally a deadtime was applied. After a detected signal, other signals within 60 ns (deadtime of the DTR system) on the same wire were discarded. Signals within 60 to 220 ns where thrown away with an exponentially decreasing probability in order to simulate the deadtime due to the pulse lengths. The accepted signals were encoded and subsequently analysed.

## 5. Experimental results and comparisons with Monte-Carlo simulations.

The distribution of the number of photoelectrons counted within the fiducial limits of the Cherenkov ring images is a convolution of the Poisson distribution of detected Cherenkov photoelectrons, with the distribution of feedback photoelectrons per primary avalanche where deadtimes effects have to be taken into account in the convolution. For detector gains allowing full single electron counting efficiency, the former distribution has an essentially constant average value $\bar{N}_{pe}$ given by the equation (1), whereas the distribution of secondary photoelectrons is strongly gain dependent. The probability of having no signal within the fiducial limits i.e. the detection inefficiency ($\eta$), is not affected by the secondary photons, and its measurement is an unambiguous and direct determination of $\bar{N}_{pe}$ via $\eta = EXP(-\bar{N}_{pe})$ which characterises a Poisson distribution.

Practically, such a determination was only possible for values of $\bar{N}_{pe}$ lower than about 4 because of the uncertainty due to both the background and to the beam content, since K and $\bar{p}$ with a Lorenz factor $\gamma$ below the threshold for Cherenkov light emission contribute to the probability for no signal. The K and $\bar{p}$ content in the beam was measured (1.4±0.3% K, 0.5±0.2% $\bar{p}$) before starting the tests and used as a correction for calculations and input parameters for Monte-Carlo simulations. Since, in the case of TMAE, $\bar{N}_{pe}$ was large (>4), the determination of $\bar{N}_{pe}$ from the measurements of $\eta$ was only used for the tests with TEA. The results are shown as a function of the cathode voltage $U_{pc}$ in figure 11 in comparison with the Monte-Carlo simulations. The agreement which is observed proves that the part of the detector response, which do not depend on the feedback photoelectrons, is well described. This crosscheck is important since the feedback photoelectron production, with its strong gain dependence, only enters as a minor contribution from the background of images from off-time particles. The uncertainties make it difficult to conclude on the TEA absolute quantum efficiency, although the simulations with 50% peak quantum efficiency give values of $\bar{N}_{pe}$ which are clearly below the experimental data.

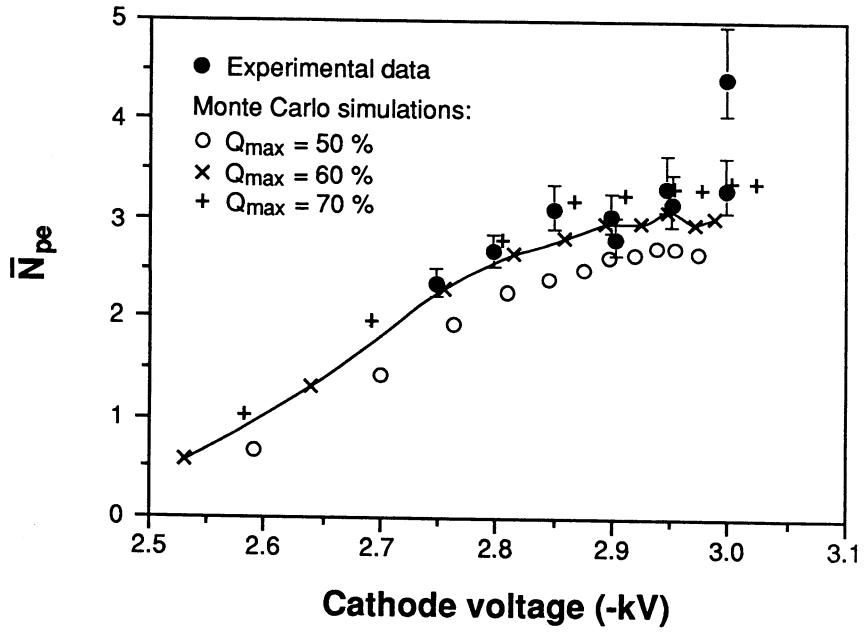


*Figure 11. The average number of photoelectrons ($\bar{N}_{pe}$ ), calculated by using the detection inefficiency ($\eta$), as a function of cathode voltage for TEA data. ( $\bar{N}_{pe}$ = - Ln ( $\eta$ ) ). Monte Carlo simulations with 50, 60 and 70% peak quantum efficiency are also shown. The calibrations of gain to cathode voltage used in the simulations are explained in section 5.3. The statistical errors of the Monte-Carlo data are < 0.05. The solid line is a set of interpolation splines to the simulations with 60% peak quantum efficiency.*

### 5.1 Photoelectron collection in the drift gap.

Tests were made with TEA where the photon absorption length $l_{ph}$ was varied over a large range (2 to 24 mm) to study the collection efficiency in the drift volume. If the electron collection efficiency close to the window for a thin slice of thickness $t_1$ is $c_1$ and the collection efficiency of the remaining gap $t-t_1$ is $c_2$ the observed number of photoelectrons $N_{pe}$ may be calculated in terms of the number of photoelectrons $N_{pe'}$ produced in an infinite conversion gap as

$$N_{pe}=N_{pe'}\cdot\left[\left(1-e^{-t_1/l_{ph}}\right)\cdot c_1+e^{-t_1/l_{ph}}\left(1-e^{-(t-t_1)/l_{ph}}\right)\cdot c_2\right] \qquad (17)$$

Assuming no collection near the window ($c_1$=0) and full collection elsewhere ($c_2$=1), for $t>>l_{ph}$ then $N_{pe}=N_{pe'}\cdot e^{-t_1/l_{ph}}$.

Figure 12 shows the logarithm of $\bar{N}_{pe}$ obtained for 10 GeV/c pions as a function of the inverse of the photon absorption length. The number of photoelectrons was estimated from the measurement of the detection inefficiency ($\eta$), as previously described, with corrections for the beam content and for a 50 mm length of the photon absorption region. The 50 mm corresponds to the sensitive length of the anode wires, and was used rather than the depths (15 and 45 mm) of the drift volume field cage, since the expected losses for photon absorption lengths $l_{ph}$ larger than $t_D/4$, where $t_D$ is the thickness of the field cage, were not observed. Given the geometry shown in figure 7, such a collection of photoelectrons created beyond the field cage is allowed. The linear dependence of $Ln(N_{pe})$ versus $1/l_{ph}$ clearly indicates a loss of photoelectrons in a thin layer at the surface of the $CaF_2$ window, which is estimated to be about 1.5±0.15 mm from the best least squares fit of a line to the data. Such a loss has already been observed [28] and explained by surface charge effect. It has, of course, been included in the Monte-Carlo simulations of the detector.

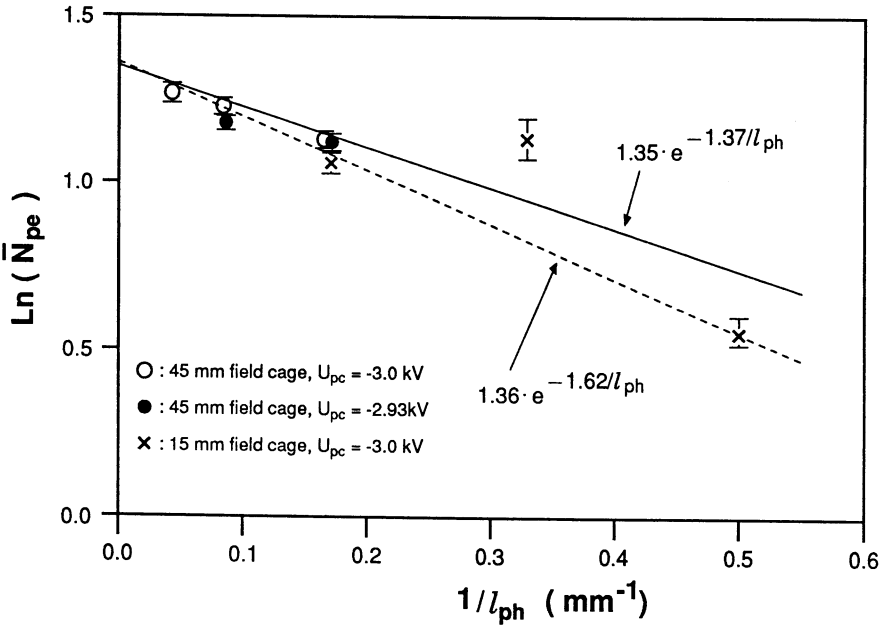


*Figure 12. The logarithm of the average number of Cherenkov photoelectrons ( $ln(\bar{N}_{pe})$ ) versus the inverse of the photon absorption length ($1/l_{ph}$). $\bar{N}_{pe}$ was calculated from the frequency of events without detected photoelectrons with corrections for beam content. Corrections were also made for the 50 mm efficient depth of the photon absorption region. The data was obtained with a 10 GeV/c pion beam using different concentrations of TEA as photosensitive vapour. The straight lines are least squares fits to the data where the solid line show the fit when all data points were used. The point at 1/lph = 0.33 was not included in the fit shown as the dashed line.*

### 5.2 Detector response and comparison with Monte-Carlo simulations.

Figures 13 to 16 and 17 to 20 show comparisons between data and Monte-Carlo simulations for TEA and TMAE respectively in pure $CH_4$ at 10 GeV/c beam momentum. In both cases one observes a very good agreement. For TEA, a maximum quantum efficiency of 60% at 8.2 eV photon energy was used. The discrepancy which is, however, observed for the first peak of the wire distribution (fig 13 and 14) is due to a large electronic noise on 8 channels of a preamplifier card, clearly visible on the scatter plot in figure 21. In both cases, the Monte-Carlo simulation reproduces correctly the background visible on the tails of the drift time distribution, with the difference due to the electronic noise mentioned.

The figures 15 to 16 and 19 to 20 exhibit in particular the spacial propagation of the secondary feedback photoelectrons relative to the primary avalanches which is again well reproduced by the Monte-Carlo simulations. One must point out that the good description of the data with TMAE was obtained by taking a surface quantum effect (from molecular adsorption of TMAE on metal surfaces) of 70% of the quantum efficiency in the gas phase. This is slightly different from the 100% previously published [33]. However, in the present detector the metallic cathode surface was different and the temperature of the detector body higher (60 to 70 $^0$C instead of 40 $^0$C).

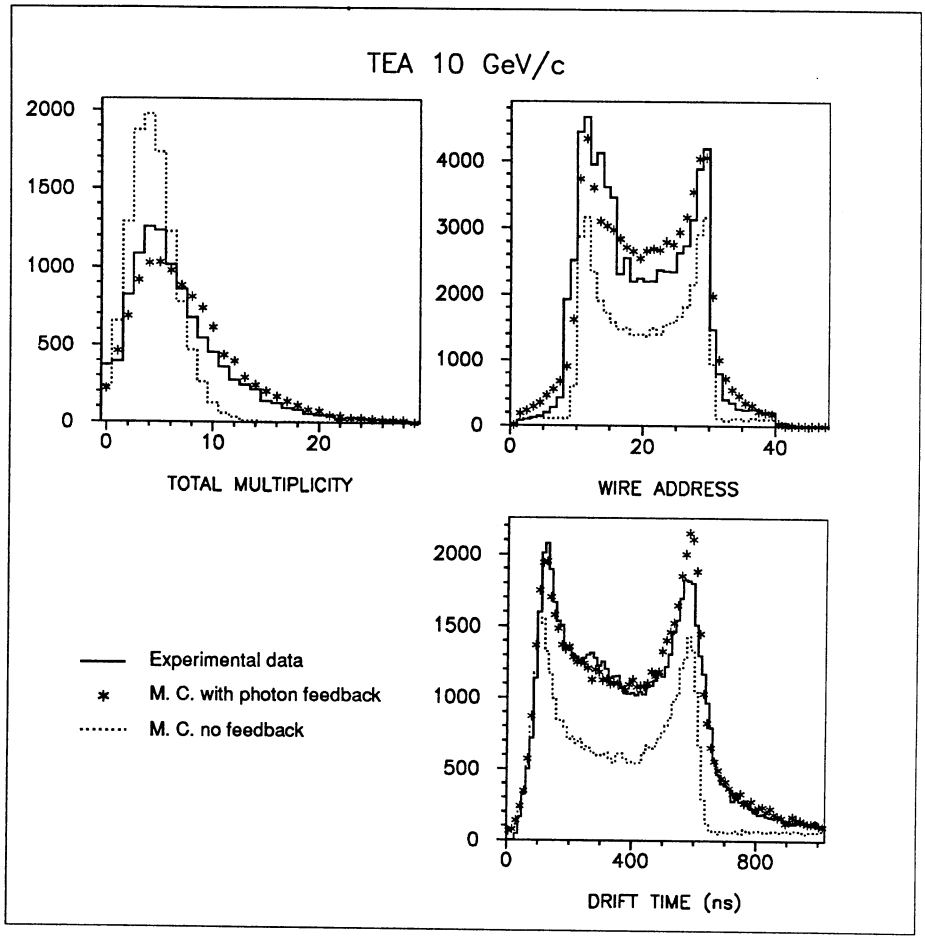


*Figure 13. The total multiplicity, wire address and drift time distributions of images obtained with 10 GeV/c beam and TEA. The simulations are made using a 60% peak photoionization quantum efficiency for TEA and a detector gain of $1.67 \cdot 10^6$ ($U_{pc}$ = 3.98 kV). The drift time range is 0 to 1 μs. The photon absorption length $l_{ph}$ is 12 mm. Both the data and Monte-Carlo samples were ~10000 events.*

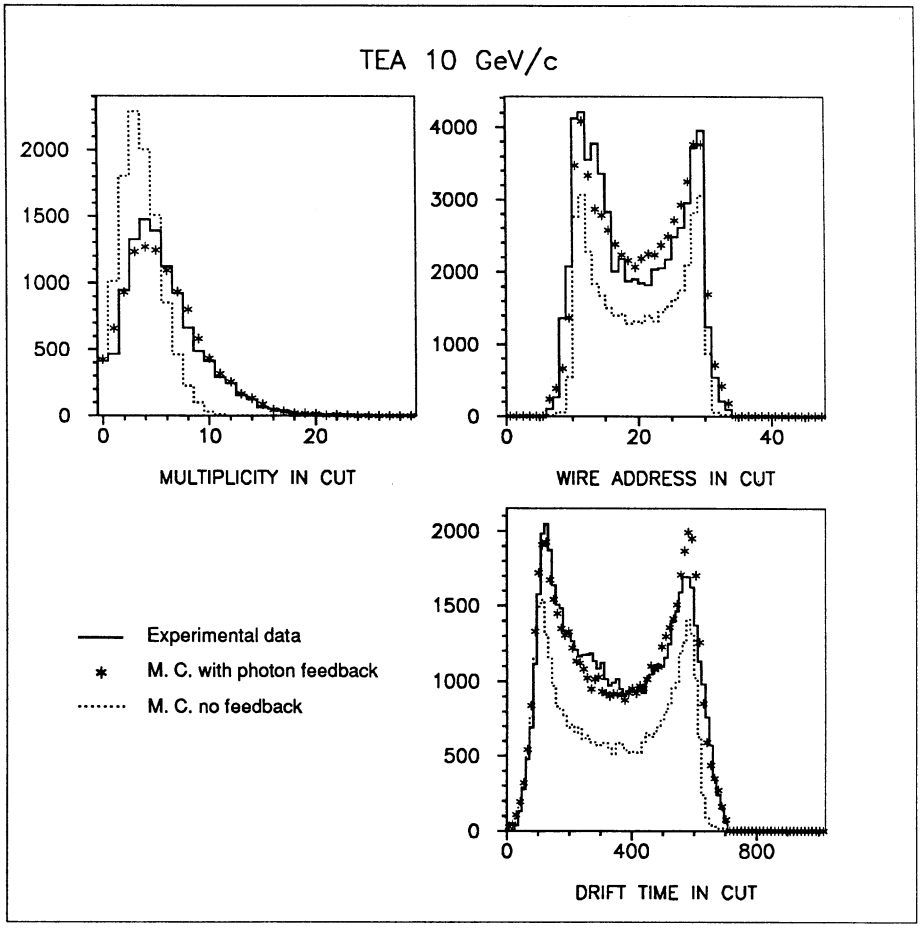


*Figure 14. The distributions of multiplicity, wire address and drift time within fiducial cuts (13 - 33 mm radius) of images obtained with 10 GeV/c beam and TEA.*

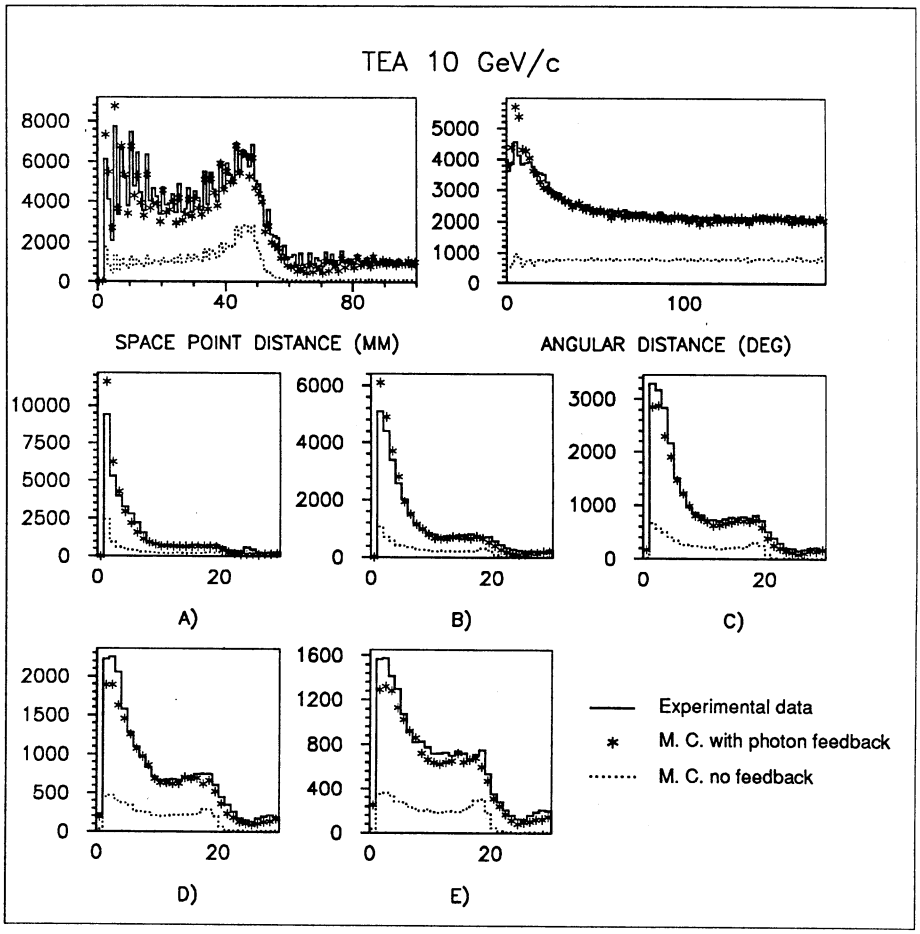


*Figure 15. Distributions to exhibit the spacial propagation of the secondary feedback photoelectrons by showing correlations between signals. The space point distance distribution shows the distance from each detected avalanche to all other detected photoelectrons within the 0 to 1 μs drift time range. Correlations in the form of the angular distance between signals within cuts calculated from the fixed expected centre are shown in the second distribution. The distributions A to E of wire distances show detected signals on neighbouring wires during 0-32, 32-64, 64-96, 96-128 and 128-160 ns respectively after a signal. Both the experimental (10 GeV/c beam, TEA, $U_{pc}$=3.98 kV) and the Monte-Carlo ($Q_{max}$ = 60%, g=1.67·10$^6$) data samples are ~10000 events.*

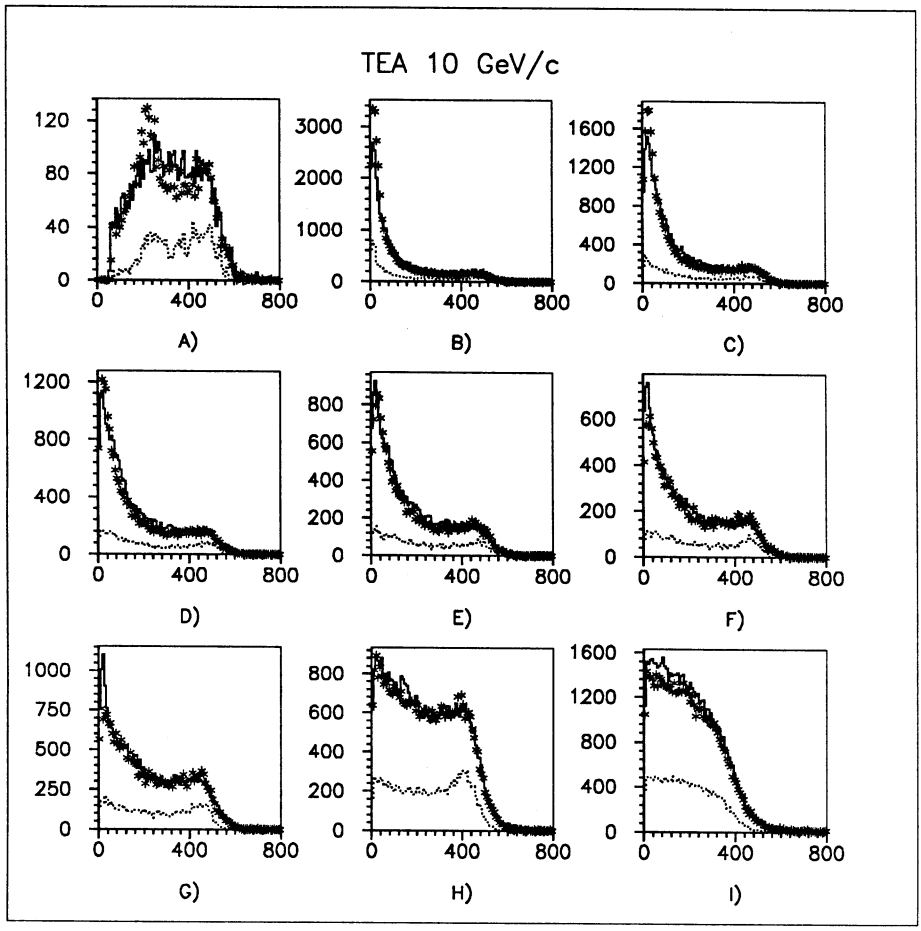


*Figure 16. Time distributions which exhibit correlations between signals; A) on the same wire; B) to G) one to six wires away respectively; H) seven and eight wires away; and I) at nine to twelve wires distance. The solid lines are experimental data (TEA), the asterisks are Monte-Carlo simulations including photon feedback and the dotted lines are simulations without feedback photons.*

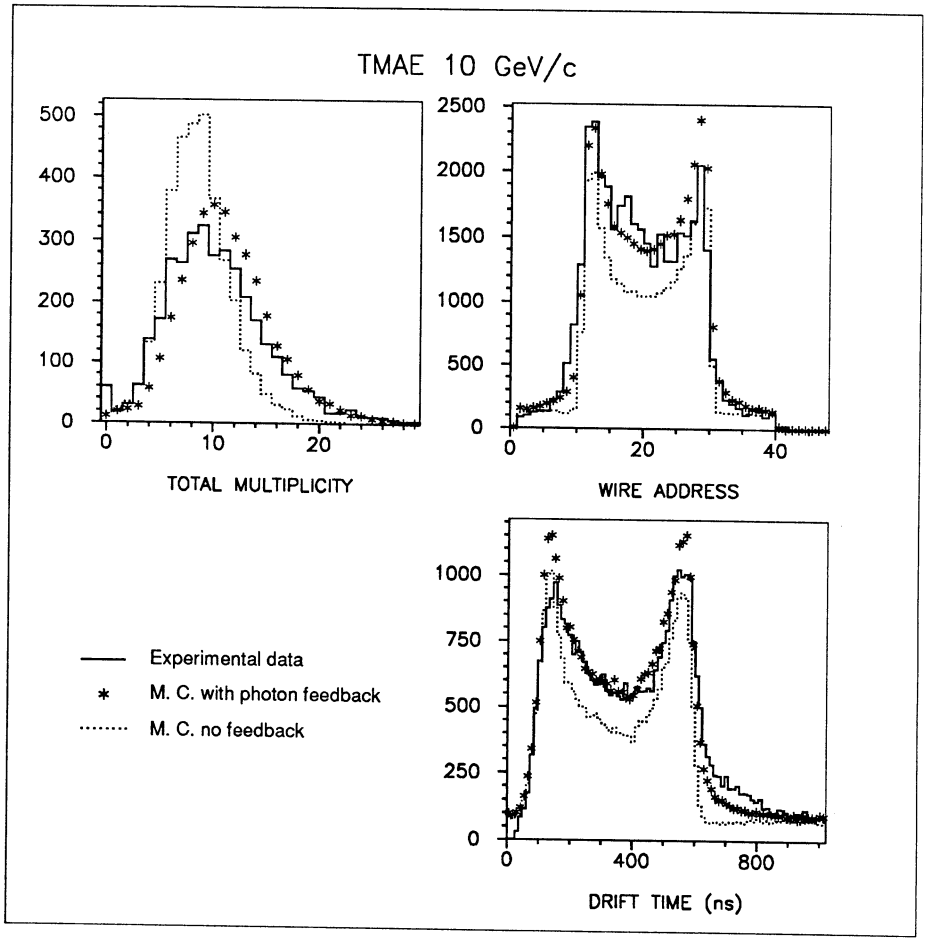


*Figure 17. The total multiplicity, wire address and drift time distributions from ring images when using TMAE. The gain used in the simulations was $3.5 \cdot 10^5$ corresponding to an anode-cathode voltage of 3.73 kV. The drift time range is 0 to 1 μs and the photon absorption length $l_{ph}$ was 15 mm. The experimental data sample was 3500 triggers to which the 3 times larger Monte-Carlo sample was normalized.*

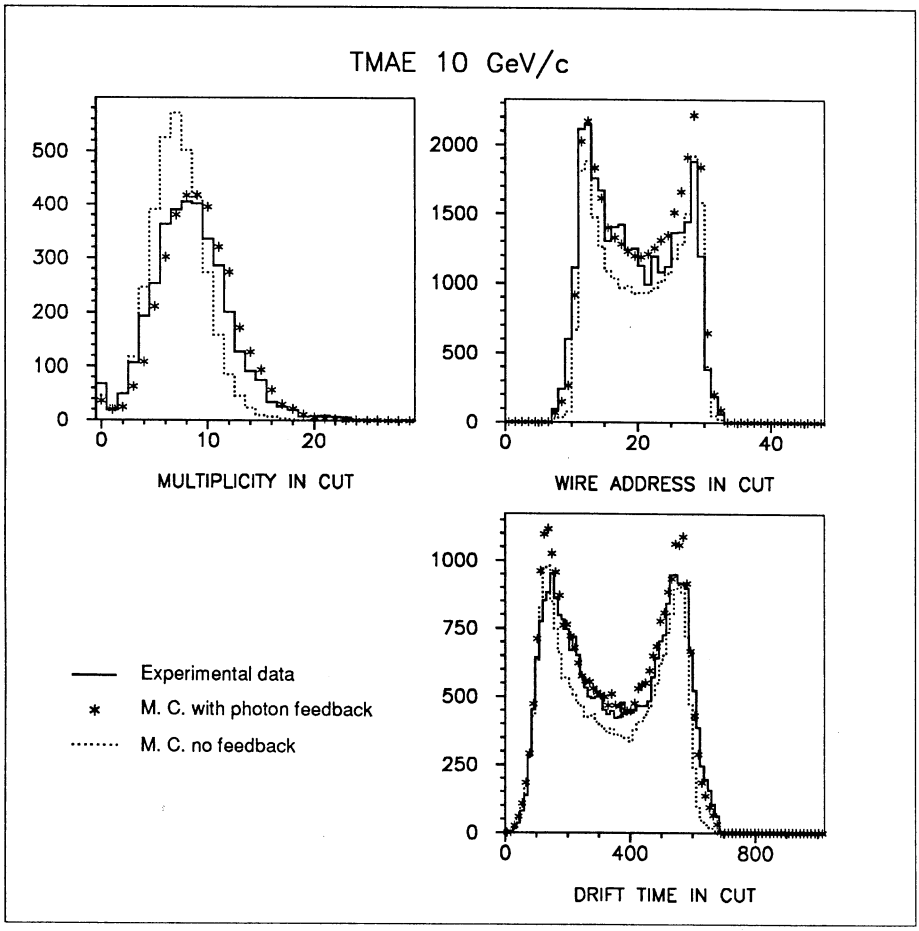


*Figure 18. The distributions of multiplicity, wire address and drift time within fiducial cuts (13 - 33 mm radius) of images obtained using TMAE.*

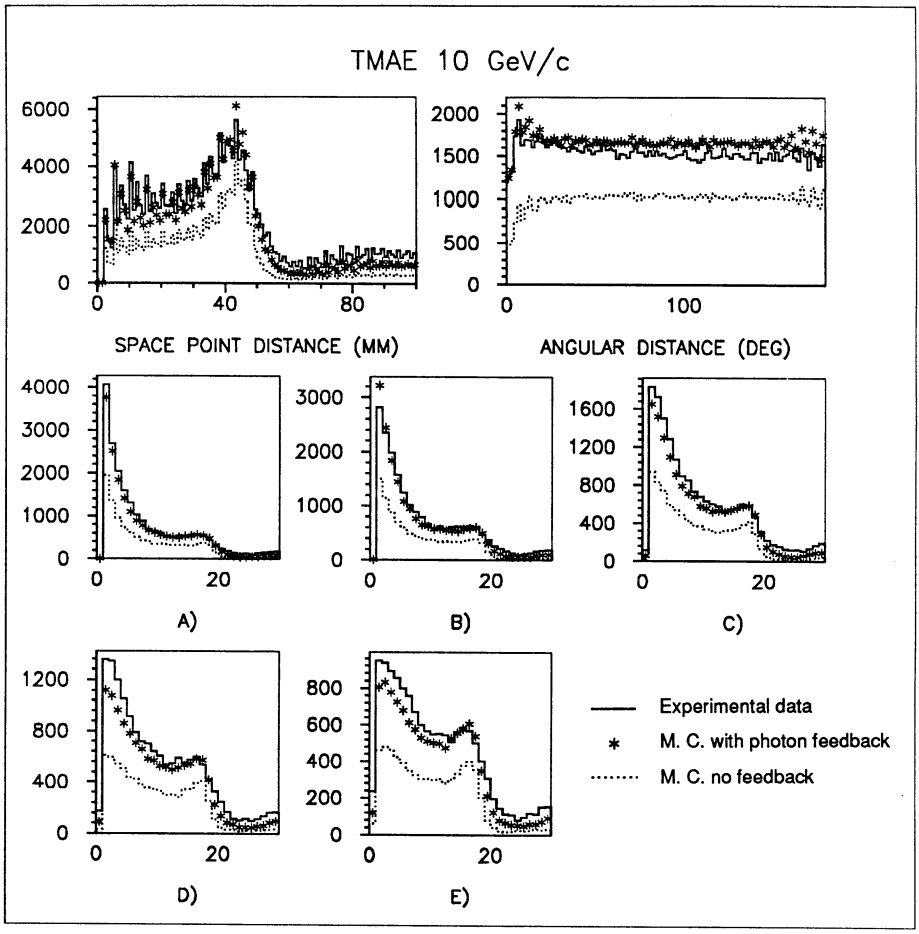


*Figure 19. Distributions corresponding to those of figure 15 but obtained using TMAE ($g$=3.5·10$^5$).*

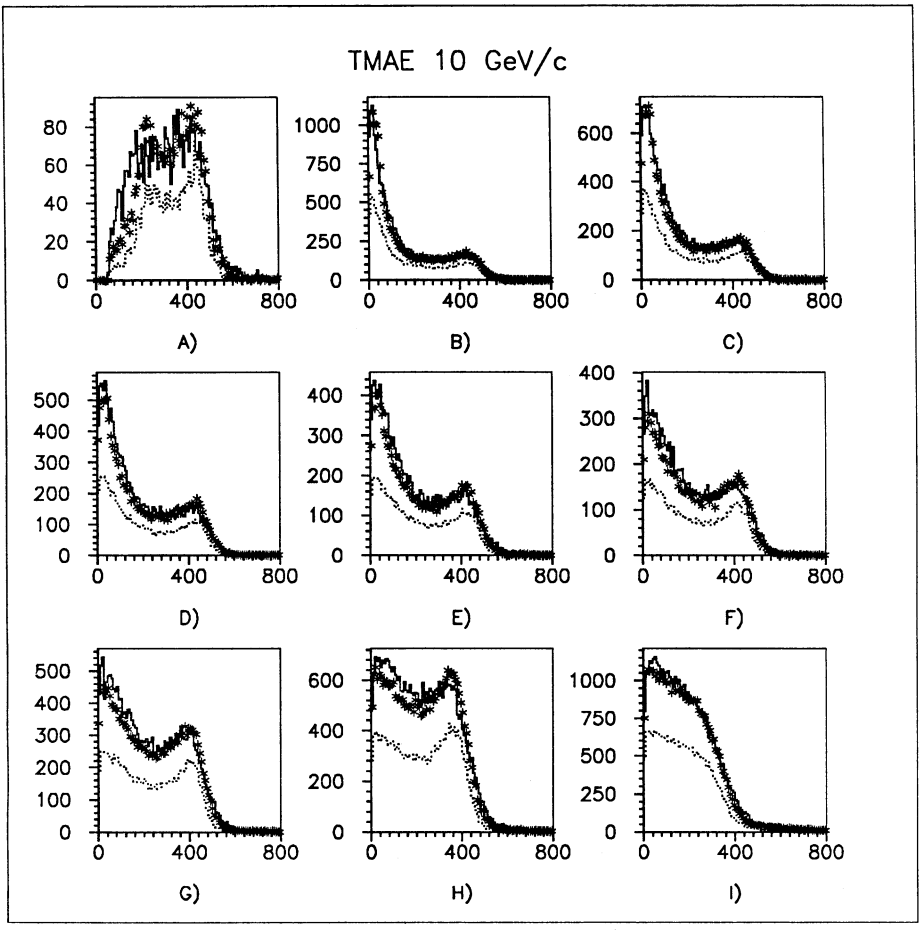


*Figure 20. Time distributions corresponding to those of figure 16 but obtained using TMAE.*

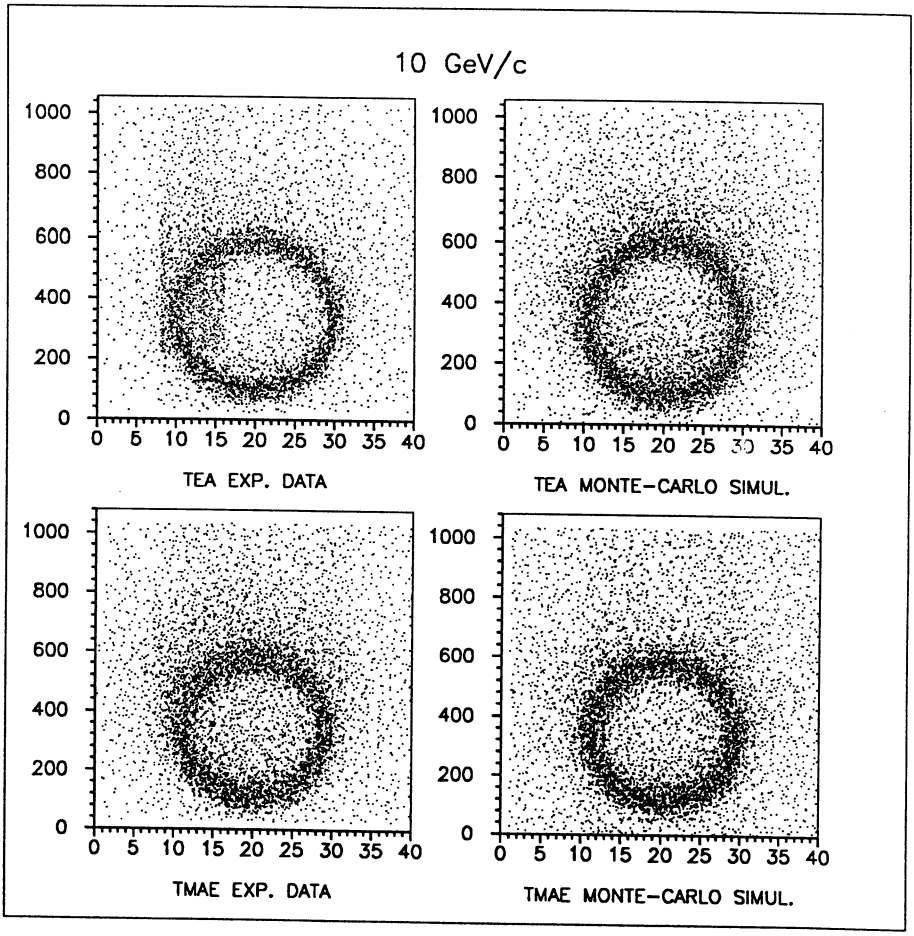


*Figure 21. Scatter plot of images from 3000 particles. A comparison of data obtained using TEA and TMAE with Monte-Carlo simulations. Photon feedback was included. The shadow at the left side of the images seen in the experimental data (especially the TEA data) is due to a large electronic noise of the preamplifier card for wires 9-16.*

### 5.3 Detection efficiency and feedback photoelectron production versus detector gain. - Limits of stability for detector operation.

The good agreement between data and Monte-Carlo simulations is preserved when the gain of the MWPC detector is changed in order to vary the feedback photoelectron production.

The exponential variation of the gain with the cathode voltage $U_c$ was verified during the tests using a $^{55}Fe$ X-ray source, but the relation between the charge developed in the avalanche and the voltage, which is needed for the Monte-Carlo simulations, was, a posteriori, obtained by a fit to the data. Figure 22 which shows the variation of the average number of photoelectrons counted within the fiducial limits as a function of $U_c$ for TEA at 10 GeV/c beam momentum. The Monte-Carlo simulations were made using a quantum efficiency at the maximum of response (8.2 eV) of 50, 60 and 70 %. The absolute voltage to gain calibration obtained by fitting the curves for the three different quantum efficiencies to the data at 2.9, 2.95 and 3.0 kV. The only free parameter was the translation along the voltage axis. The simulations indicate detector instability at 2.97, 3.0 and 3.02 kV corresponding to gains of 2.4, 1.9 and $1.6.10^6$ for 50, 60 and 70 % peak quantum efficiency respectively. The 60% peak quantum efficiency curve had the lowest $\chi^2$ in the fit. This combination of quantum efficiency and voltage - gain relation is the only one of the three that can reproduce all our data, in particular for the distributions shown in section 5.2 and the variation with cathode voltage for both TEA and TMAE.

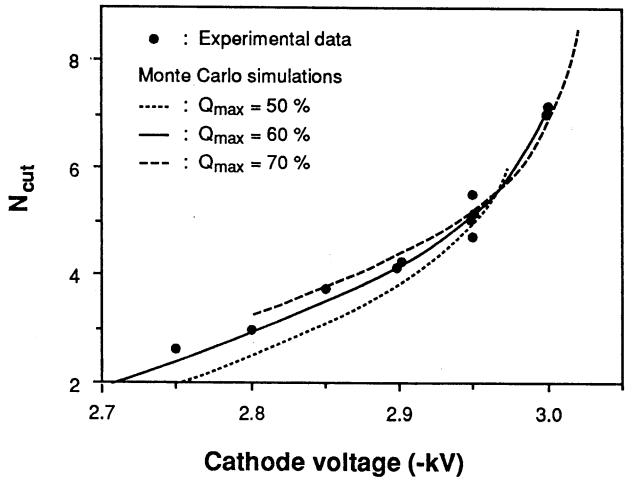


*Figure 22. The multiplicity within fiducial cuts as functions of voltage difference between anode and cathode in the MWPC detector. The data are obtained using TEA with a photon absorption length of 6 mm. The Monte-Carlo simulations shown are made with 50, 60 and 70% peak quantum efficiency and with a gain at 2.95 kV which is fitted to be $1.95{\cdot}10^6$, $1.41{\cdot}10^6$ and $1.02{\cdot}10^6$ respectively*

The result that $Q_{max}$ is 60% significantly contrasts with the 33% reported by Holroyd et al [5] but is compatible with other ring imaging data [1,29,30] and the actinometric measurements [7] as described in section 2.

In figure 23 the total multiplicity and the multiplicity within the fiducial cuts are shown as functions of cathode voltage for both TEA and TMAE. The results show that a good agreement between data and simulation is obtained over a one order of magnitude range of gains from $1.5 \cdot 10^5$ to $1.9 \cdot 10^6$ corresponding to cathode voltages of 2.6 to 3.0 kV.

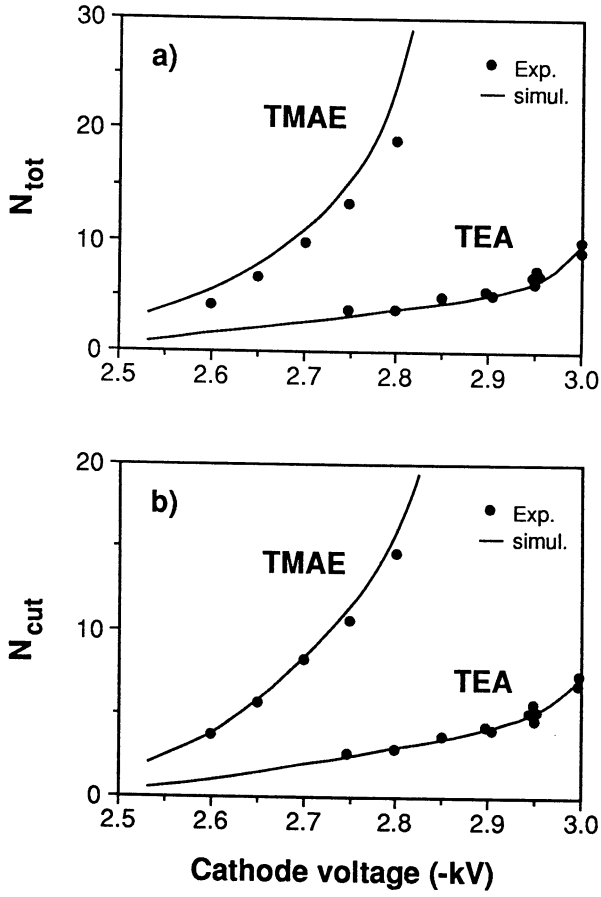


*Figure 23. Total multiplicity (a) and multiplicity within fiducial cuts (b) as functions of voltage difference between anode and cathode in the MW detector for both TEA andTMAE. The Monte-Carlo simulations are shown as lines where a 60% peak quantum efficiency was used for TEA. The dashed-dotted line in (a) show the calibration between the detector voltage and the gain used in the simulations. The maximum achievable gain before instability was found to be ~ $7 \cdot 10^5$ and $1.9 \cdot 10^6$ for TMAE and TEA respectively.*

Taking the 60% peak quantum efficiency for TEA as input to the Monte-Carlo simulations, the number of feedback photoelectrons produced ($N_{pfb}$) and detected ($N_{dfb}$) per avalanche from Cherenkov photoelectrons can be estimated as functions of the gain and the photon absorption length ($l_{ph}$). The results are shown in figure 24 for TEA ($l_{ph}$ = 6 mm) and TMAE ($l_{ph}$ = 15 mm) respectively in the same conditions as the beam tests. The fraction of feedback photoelectrons detected is of course dependent on $l_{ph}$, on the detection efficiency and on the electronic dead time. The rise of $N_{pfb}$ with the gain is very sharp for TMAE in comparison with TEA and exhibits a clear limit of stability for the detector operation at about $7 \cdot 10^5$ which is similar to previously published measurements [33]. For this detector when operated with TEA the gain can, roughly, be increased by a factor 3 relative to the use of TMAE in order to keep the same rate of feedback photoelectrons.

In this respect the use of TEA provides a definite advantage over TMAE. Thus, with a low noise level electronic for detection which would allow operating gains between 2 and $4 \cdot 10^5$, there is no problem caused by the feedback photoelectrons when using TEA. For these tests reported here, because of the low sensitivity of the electronics used, gains above $8 \cdot 10^5$ were required for a detection efficiency better than 95% (see figure 24 and 23). This gain was higher than the maximum attainable with TMAE. The tests with TMAE only allowed the detection of about 85 % of the Cherenkov photoelectrons with a large background (nearly 1 : 2) smearing the single photon Cherenkov angle resolution.

For the highest gains which can be attained with TEA and TMAE, the probability of having at least one secondary photoelectron per avalanche is about 0.5 (see figure 24) in agreement with previous results by Dresselhaus et al [38].

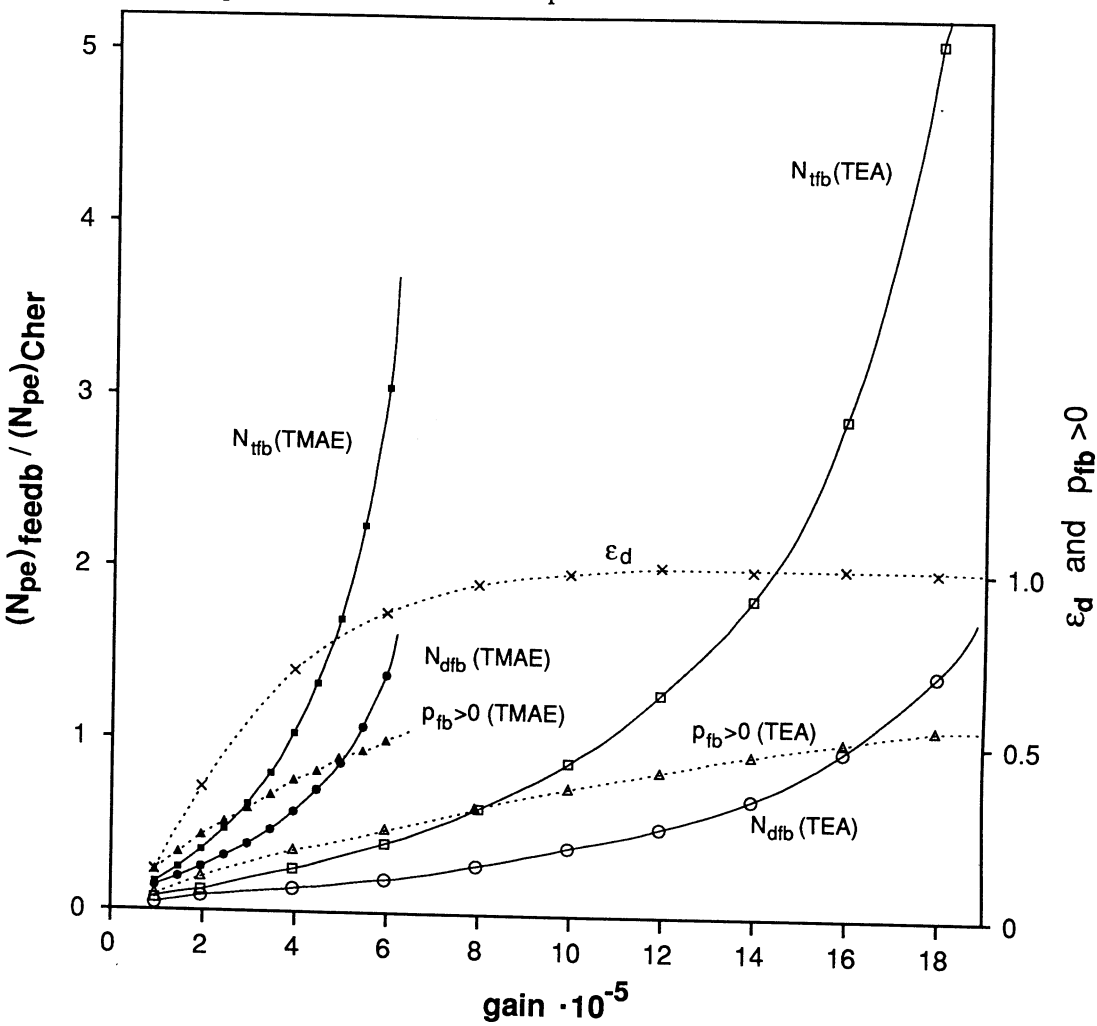


*Figure 24 The number of produced ($N_{pfb}$) and detected ($N_{dfb}$) feedback photoelectrons per Cherenkov photoelectron for TEA and TMAE estimated by Monte-Carlo simulations as functions of the detector gain. A 60% peak quantum efficiency for TEA was used. The probabilities of having at least one feedback photoelectron ($p_{fb}$) and the detection efficiency are also shown. The difference between the produced and detected feedback photoelectrons at full detection efficiency is due to electronic deadtime. $p_{fb}$ is about 50% at the upper limit of detector gain for both TEA ($g \sim 1.9 \cdot 10^6$) and TMAE ($g \sim 7 \cdot 10^5$).*

### 5.4 Variation of the detector response with the particle Lorenz factor. - Determination of the merit factor $N_0$.

Tests have been performed with TEA at various beam momenta in order to measure the variation of the average number $\bar{N}_{pe}$ of Cherenkov photoelectrons produced as a function of the Cherenkov angle $\theta_c$. The radius r of the ring image and the photoelectron yield vary with $\theta_c$ according to the relations $r = f \cdot \tan\theta_c$ and $\bar{N}_{pe} = N_0 \cdot L \cdot \sin^2\theta c$ respectively, where f is the focal length of the mirror. Hence, for small Cherenkov angles

$$\bar{N}_{pe} = \left(\frac{N_0 \cdot L}{f^2}\right) \cdot r^2 \qquad (18)$$

is a good approximation. The variation of the average number of detected Cherenkov photoelectrons with $r^2$ is thus expected to be linear with slope proportional to the merit factor $N_0$.

Measurements were made with pions of 5.36, 6.21, 7., 7.92 and 16 GeV/c momentum, the detector being operated with a photon absorption length $l_{ph}$ of 6mm, and at 6.21 and 10 GeV/c with $l_{ph}$ = 12 mm, all at a gain of $1.65 \cdot 10^6$. Because of the photoelectron capture within a 1.5 mm thick layer at the $CaF_2$ window surface, we have corrected the number of photoelectrons counted by the factor $e^{1.5/l_{ph}}$ in order to compare the data independent of $l_{ph}$. The results are shown in figure 25. The straight line is the best fit to the Monte-Carlo simulations obtained with 60 % peak quantum efficiency for the TEA response. The nonzero value of $\bar{N}_{pe}$ for $r^2 = 0$ corresponds to the accidental background within the fiducial limits. The agreement with the experimental data is good. It thus confirms the previous conclusion on the photoionizing properties of TEA.

From the slope of the straight line, one can calculate a value of $N_0 = 38.6\ cm^{-1}$ for f = 100 cm and L = 187 cm, assuming no loss of photoelectrons drifting near the window. This value corresponds to the use of two $CaF_2$ windows, where the second window causes an additional loss of 33 % on the photon transmission. Since the second window was used only for historical reasons as described earlier, such losses can be avoided in presently designed detectors. We therefore claim that a merit factor $N_0 = 58\ cm^{-1}$ is achievable using TEA and a good UV transmitting $CaF_2$ window with improved field definition to eliminate photoelectron capture near the window.

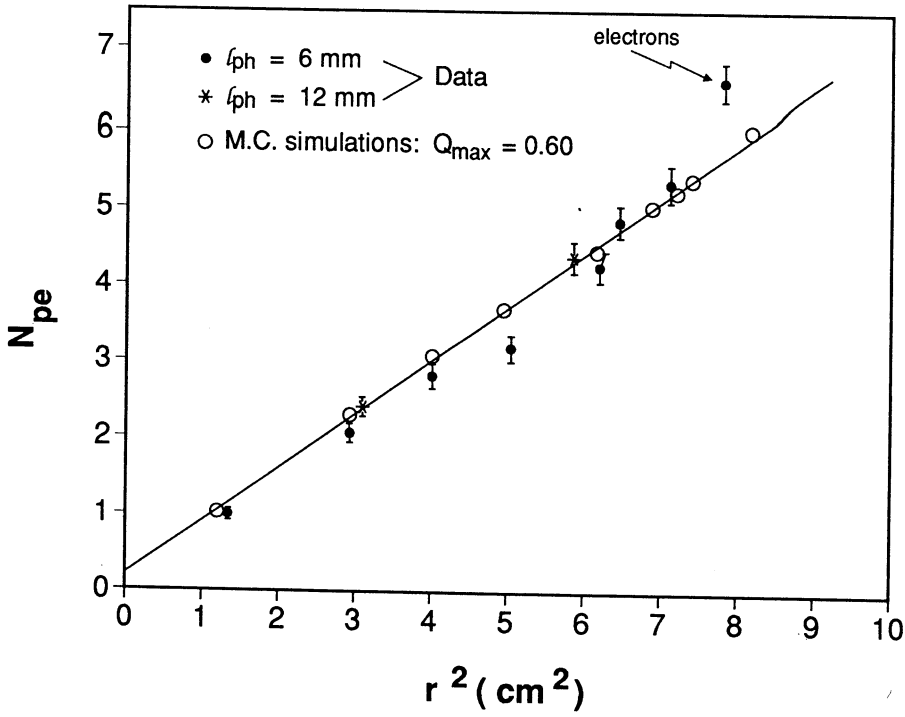


*Figure 25. The number of detected Cherenkov photoelectrons, estimated using the detection inefficiency with corrections for beam contents, as a function of the square of the ring image radius. Data was taken with a predominantly pion beam of varied momentum using two different concentrations of TEA giving photon mean free paths of 6 and 12 mm. The data are corrected for drift losses close to the detector window in order to compare the results for both concentrations. External identification by a threshold Cherenkov counter was used to obtain a measurement with a pure electron beam shown as the data point marked "electrons". The straight line is a least squares fit to the Monte-Carlo simulations which are made using a 6 mm photon mean free path and a TEA peak quantum efficiency of 60%.*

### 5.5 Single photon Cherenkov angle resolution.

The requirement of $N_{pe} \geq 3$ for fitting radius and centre position of circles to the ring images, as described in section 4.2, gives a bias towards high multiplicity events with increased sensitivity to feedback photoelectrons and background, especially in the case of TEA where on average only ~3.3 Cherenkov photoelectrons are expected (from simulations without photon feedback, crosstalk and background but including deadtime). However the image centre expected for each event is determined from the average fitted centre of the sample, with a $\sigma$ of 0.6 mm due to beam divergence. One can thus, also for low multiplicity events ($N_{pe}<3$), calculate the radius of single photoelectrons by using the expected centre.

The distributions of the single photoelectron radii and the fitted radii obtained for 10 GeV/c pions are shown in figure 26 and compared to Monte-Carlo simulations for TEA and TMAE respectively. In the single photoelectron radius distributions there is a very good agreement between data and the Monte-Carlo simulations where feedback photoelectrons are included. The double peak reflects the binning of the wire coordinate. The distributions of fitted radii show a slightly less impressive but still good agreement. However, one has to keep in mind that the circle fit is sensitive to the azimuthal distibution of the detected photoelectrons, and thus to nonuniformities in the detector response, such as noisy electronic channels and slight differences in drift losses at various positions in the drift volume, which are not included in the simulations.

The average radius and the radius resolution $\sigma_r$ of single photoelectrons are listed in table 2.

---

*Table 2. The average radius, the resolution $\sigma_r$, the average number of detected photons in the radius peak and the average background signal for experimental data and Monte-Carlo simulations with and without feedback photoelectrons for TEA and TMAE.The average radius and the resolution $\sigma_r$ are calculated from the single photoelectron radius by fitting with a Gaussian which represents the signal and a second order polynomial to describe the background. $(N_{pe})_{peak}$ is calculated by subtracting the fitted background from the experimental distribution. $N_{bkg}$ is the contents of the fitted background per event in the radius range from 0 to 50 mm .*

| | Radius (mm) | $\sigma_r$ (mm) | $(N_{pe})_{peak}$ | $N_{bkg}$ |
|---|---|---|---|---|
| TEA | | | | |
| Exp. data | 24.54 | 2.84 | 4.66 | 1.84 |
| M.C. inc. feedback | 24.56 | 2.65 | 4.32 | 1.94 |
| M.C. no feedback | 24.51 | 2.21 | 3.45 | 0.31 |

| | Radius (mm) | $\sigma_r$ (mm) | $(N_{pe})_{peak}$ | $N_{bkg}$ |
|---|---|---|---|---|
| TMAE | | | | |
| Exp. data | 23.28 | 2.88 | 6.82 | 3.37 |
| M.C. inc. feedback | 23.23 | 2.62 | 7.63 | 2.72 |
| M.C. no feedback | 23.16 | 2.31 | 6.38 | 1.25 |

The number of detected photons in the experimental data and simulations with photon feedback, are larger than the expected number of Cherenkov photoelectrons, indicating that the background subtracted distribution still contains a large amount of feedback photoelectrons. In fact, as expected, it is one of the main contributions to the error $\sigma_r$ as indicated in table 3.

*Table 3. The dominant contributions to the radius error $\sigma_r$ as found from Monte-Carlo simulations. In the simulation only one source at the time was contributing. The chromatic aberrations are errors due to thevariation of the refractive index with photon energy in the radiator. The wire-binning is used in the contributions from crosstalk and feedback photoelectrons. The parallax error is due to the combination of the photon mean free path in the photosensitive gas and the incidence angle of the light. All errors are given as the error per photoelectron calculated from the single photoelectron distribution after background subtraction as described in table 2. The simulations are made with a gain of $1.67 \cdot 10^6$ and $3.5 \cdot 10^5$ and a mean photon absorption length of 6 and 15 mm for TEA and TMAE respectively.*

| Error source | $\sigma_r$ (mm), TEA | $\sigma_r$ (mm), TMAE |
|---|---|---|
| Chromatic aberrations | 0.4 | 0.7 |
| Parallax | 0.9 | 1.0 |
| Drift dispersion | 1.2 | 1.2 |
| Crosstalk and wire binning | 1.0 | 0.5 |
| Feedback | 0.9 | 1.1 |
| Beam divergence | 0.6 | 0.6 |
| $\sqrt{\sum_i \sigma_i^2}$ | 2.14 | 2.18 |

The drift dispersion is found to be the most dominant source of error. The drift dispersion of the present detector was measured in reference [28]

where an improved drift field cage was shown to have about half the time dispersion ($\sigma_{0t}$) of the present detector. The larger energy acceptance of TMAE makes the cromatic aberrations more important.

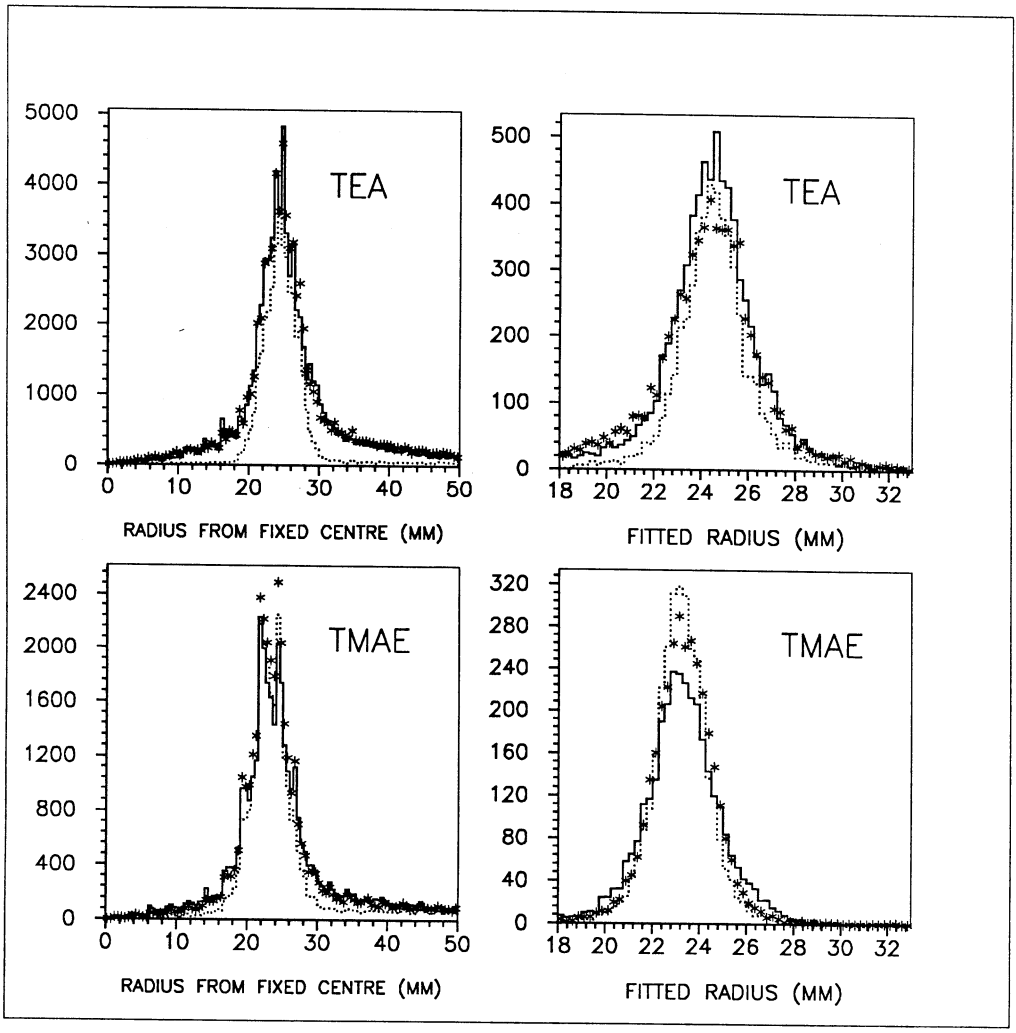


*Figure 26. Distributions of single photoelectron radii from the expected image centre and distributions of fitted radii for TEA and TMAE shown as solid lines. The asterisks and dotted lines are Monte-Carlo simulations with and without feedback photon production respectively. A 60% peak quantum efficiency was used for TEA. The gain was $1.67 \cdot 10^6$ and $3.5 \cdot 10^5$ for TEA and TMAE respectively. The double peak in the single photoelectron radius distributions reflect the wire-binning.*

# 6 Fast RICH detectors.

Particle identification at the next generation of hadron colliders (LHC and SSC) is a challenge for the Ring Imaging technique. Identification should be achieved over a wide momentum range of up to at least 200 GeV/c for $\pi$ - K separation (1 % misidentification limit) and for an interaction rate of $10^8$ $s^{-1}$ as expected for luminosity of $10^{33}$ $cm^2$ $s^{-1}$. The separation requirements impose the use of the least dispersive gaseous radiator media such as He, Ne, $CF_4$ or $C_2F$ and of high granularity photoelectron detectors (1 or 2 $mm^2$ measurement pixel) to obtain the required angular resolution and multihit capability for large multiplicity events. The high rate implies very fast photon detectors with a time dispersion of less than 15 ns to avoid overlapping of events from different beam crossings.

We show in this section that comparable performances for particle separation can be obtained with TEA as well as TMAE and we discuss Monte-Carlo simulations of the expected response of fast photondetectors which emphasize the interest of using TEA rather than TMAE.

## 6.1 Particle separation at high energies using TEA or TMAE.

The momentum p for which $n_\sigma$ standard deviations separate the $\pi$ - K hypothesis on particle identity, limited by chromatic aberrations only, is given by,

$$p^2 = \frac{\sqrt{N}}{2 \cdot n_\sigma} \cdot \frac{1}{\Delta n} \left(m^2_K - m^2_\pi\right) \qquad (17)$$

with N the number of detected Cherenkov photons for a $\beta$=1 particle. The variance of the refractive index $\Delta n$ is approximated with

$\Delta n = \left(\frac{dn(E)}{dE}\right)_{E=\bar{E}} \cdot \frac{\Delta E}{2.36}$ where the dispersion of the radiator gas $\frac{dn(E)}{dE}$ is calculated at the average photon energy $\bar{E}$ and where $\Delta E$ is the FWHM of the energy acceptance distribution ( $\left(1 - \frac{1}{n^2(E)}\right) \cdot Q_E(E) \cdot R(E) \cdot T(E)$, with n(E) the refractive index, $Q_E(E)$ the quantum efficiency of the photosensitive molecule used, R(E) the mirror reflectivity and T(E) the gas and window transmissions). The total energy acceptance is 7.5 to 8.5 eV for TEA with $CH_4$ as carrier gas and $CaF_2$ window, and 5.4 to 7.8eV for TMAE with a $CH_4$ - $C_2H_6$ mixture and quartz window. $\Delta E$ is estimated to about 0.7 and 1.5 eV for TEA and TMAE respectively.

The formula (17) can now be written:

$$p^2 = \frac{\sqrt{N}}{2 \cdot n_\sigma} \cdot \left(\frac{dn(E)}{dE}\right)_{E=\bar{E}} \cdot \frac{2.36}{\Delta E} \left(m^2_{\overline{K}} - m^2_\pi\right) \qquad (20)$$

The performance for particle separation is kept the same for TEA and TMAE if the gas of the radiator is chosen such that,

$$\left(\frac{1}{\sqrt{N}} \cdot \frac{1}{\left(\frac{dn(E)}{dE}\right)_{E=\bar{E}}} \cdot \Delta E\right)_{TMAE} = \left(\frac{1}{\sqrt{N}} \cdot \frac{1}{\left(\frac{dn(E)}{dE}\right)_{E=\bar{E}}} \cdot \Delta E\right)_{TEA} \qquad (21)$$

A quality factor $N_0 = 150$ cm$^{-1}$ can be obtained with TMAE, the best quality fused quartz window (7.8 eV energy cut-off e.g. Tetrasil SEH) and 90% reflectivity mirrors. Under such conditions 25 photoelectrons per image can be detected for a 4 m long (L) He - $CH_4$ gas radiator with a Lorentz factor at threshold $\gamma_t = 49$ ($N = N_0 \cdot L \cdot \gamma_t^2$). This gas mixture has a chromatic dispersion

$$\left(\frac{dn}{dE}\right)_{E=7eV} \approx 5 \cdot 10^{-6} \text{ eV}^{-1}, \quad (\Delta E = 1.5 \text{ eV})$$

Hence, for 1 % misidentification ( $n_\sigma = 4.2$ ), equation (18) gives 205 GeV/c for $\pi$ - K separation, 345 GeV/c for K - p and 60 GeV/c for e - $\pi$ respectively.

According to the present work a quality factor $N_0$ of 58 cm$^{-1}$ can be achieved with TEA. By using better windows (80% transparency over the TEA range) and mirrors (90% reflectivity) it appears that $N_0 = 80$ cm$^{-1}$ can be attained. This would give N = 13.3 photoelectrons for the same radiator as above ( L = 4 m, $\gamma_{th} = 49$ ). The dispersion dn/dE at the 8 eV average photon energy of a TEA - $CH_4$ detector is slightly larger ($7 \cdot 10^{-6}$ eV$^{-1}$) while the energy acceptance is only about half (0.7 eV) compared to a detector with TMAE. The 1 % misidentification limit gives for the TEA detector 215 GeV/c for $\pi$ - K separation, 365 GeV/c for K - p and 64 GeV/c for e - $\pi$ respectively. This justifies the possible use of TEA for RICH detectors at high energy.

To optimize the overall resolution requires the measurement pixel s to be such that:

$$\Delta\theta_{geom} = \frac{s}{\sqrt{12}} \cdot \frac{1}{f} < \Delta\theta_{chrom} \qquad (22)$$

where f = L is the focal length of the mirror and

$$\Delta\theta_{chrom} = \frac{dn}{dE} \cdot \frac{\Delta E}{2.36} \left(\gamma_t - \frac{1}{\gamma_t}\right) = \gamma_t \cdot \frac{dn}{dE} \cdot \frac{\Delta E}{2.36} \qquad (23)$$

for high $\gamma_t$ values. Hence $s < \gamma_t \cdot \left(\frac{dn}{dE} \cdot \Delta E\right) \cdot L \cdot \frac{\sqrt{12}}{2.36}$.

s < 2.16 and 1.49 mm is obtained for TMAE and TEA respectively. Such sizes for square pads seems unacceptable in respect of cost for large detector areas, construction and space for electronics implantation on the detector. Hence, a compromise must be found which will make the photon detector resolution rather than the chromatic dispersion of the radiator medium, the dominant source of error for the Cherenkov angle determination .

### 6.2 Photon detector

A fast photon detector with a drift time dispersion $\sigma_t \approx 10$ ns can be made with a direct coupling between the conversion gap and the photoelectron detector, where the latter can be either a conventional multiwire proportional chamber (MWPC) or a multistep avalanche chamber (MSAC) , the two dimensional image being obtained by pad array readout. The signal detected on the pads of the MWPC (figure 27) is generated by positive ions migrating towards the cathode planes, whereas in the MSAC, shown in figure 28, it is given by the charge collection of the electrons created in the avalanches. The latter solution has recently been successfully tested [39], however with a poor time resolution in comparison to the present requirements.

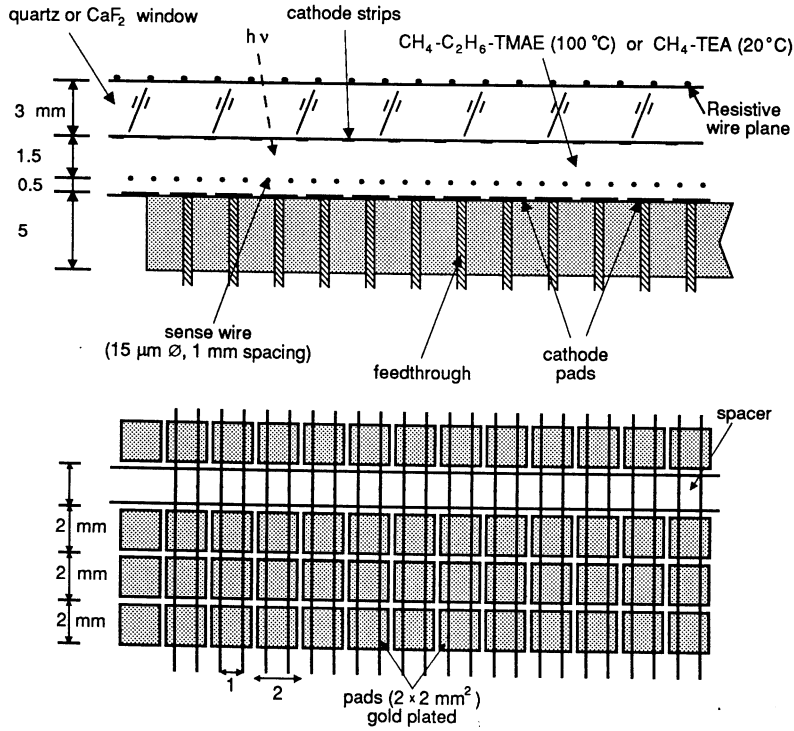


*Figure 27. A fast photon detector with multiwire chamber (MWPC) geometry. The photons ionize the TMAE (TEA) molecules after passing the 3 mm thick quartz (CaF2) window. The position information about the conversion points are obtained both by the wires and the cathode pads.*

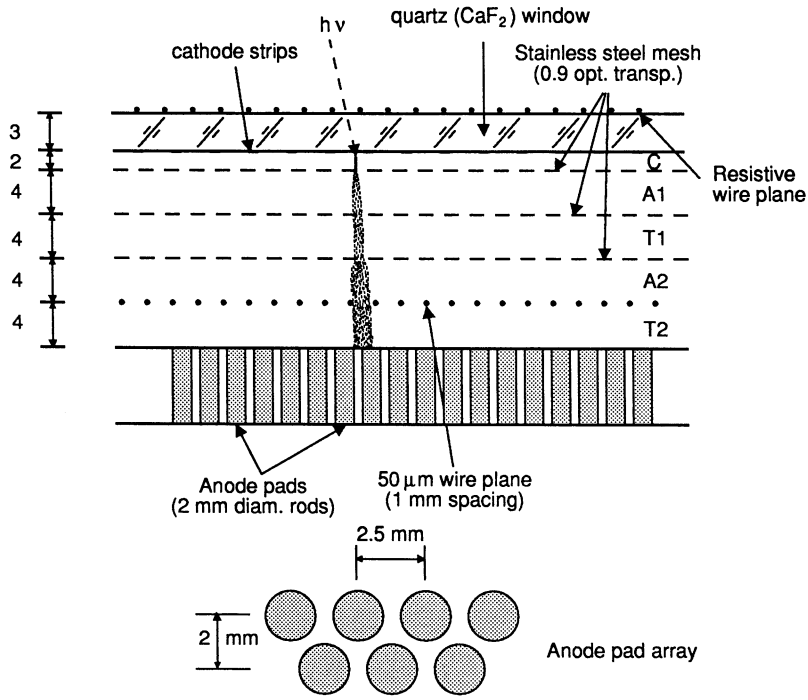


*Figure 28. A multistep avalanche chamber (MSAC) for photon detection. The photons ionize the TMAE (TEA) molecules in the conversion gap (C). The photoelectron drifts into the first amplification gap A1 where charge multiplication takes place. The charge passes the transfer gap T1 for further amplification in the A2 gap and is then transferred via the gap T2 for collection on the anode pads.*

The time dispersion $\sigma_t = l_{ph}/v_d$, where $l_{ph}$ is the photon absorption length and $v_d$ the drift velocity. To obtain at least 95% photon collection efficiency 3 photon mean free paths thickness of the conversion gap is needed. Taking $\sigma_t$ = 10 ns and $v_d$ = 6 cm·μs$^{-1}$ for TMAE in $CH_4$ (75%), $C_2H_6$ (25%) and 10 cm·μs$^{-1}$ for TEA in pure $CH_4$ (both at $E_d$ = 0.6 kV/cm) give an upper limit $l_{ph}$ = 0.6 mm and 1 mm for TMAE and TEA respectively with a total collection time of $3 \cdot l_{ph}/v_d \approx$ 30ns. To obtain 0.6 mm requires a TMAE bubbler at 95 $^0$C (see section 2) and a detector temperature of at least 100 $^0$C to prevent condensation. This imposes severe mechanical constraints on the detector design to minimize the distortions from thermal expansion. The difficulties may be overcome for MWPC detectors using boron nitride as construction material for the detector body and metallized quartz fibres for the anode wires. It seems, however, harder to find an acceptable solution for

the construction of the parallel mesh planes of large MSAC photon detectors.

TEA, on the contrary, does not need heating since its photon mean free path is 0.6 mm at 20 $^0$C. It requires, however, the radiator gas to be transparent up to 8.5 eV ($CH_4$ cut off), hence He, Ne, $CF_4$, $C_2F_6$ or mixtures of these ( $25 < \gamma_t < 112$ ). Gas transparency higher than 95% implies that the $O_2$ content should be kept below 0.3 ppm for a 6 m average photon path. Such a strong limitation which does not exist with TMAE is due to the large $O_2$ photoabsorption cross section in the energy region of the TEA acceptance ($\sigma_a$ = 12 Mb at 8.5 eV photon energy).

In the MWPC the distance (d) between wires and cathode is 0.5 mm in order to increase the capacitive coupling and, hence, the induced signal on the pads. A 2 mm total gas thickness of the detector gives 3.3 photon mean free paths for both TMAE at 95$^0$C and TEA at 20$^0$C. The longest drift path (from the window to the wire plane) is only ~1.5 mm, hence, a total collection time of the Cherenkov photoelectrons ~ 15ns (TEA - $CH_4$) and ~ 25 ns (TMAE - $CH_4$ - $C_2H_6$). Owing to the thinness of the gas layer and the very short photon mean free path, the ionization of charged particles crossing the detector should not cause problems because of the feedback photoelectron production. This is an important feature as it avoids the use of "blinds" between wires, allowing easy construction.

The resolution $\sigma_x$ in the transverse direction x to the wires for the detector shown in figure 27 is $\Delta_w/\sqrt{12}$ ($\Delta_w$ = 1 mm = wires spacing) if the wire signals are used as information on the photoelectron position. Under this condition the pad size $\Delta x$ can be chosen longer than the size $\Delta y$, provided that the probability of ambiguities for reconstruction are small. This would allow measurement pixels of 1 x 1 mm$^2$ with pad sizes of 10 ($\Delta_x$) x 1 ($\Delta_y$) mm$^2$, for example, at a lower cost with much larger possibilities to locally implement elecronic chips on the back of the detector. Such a possibility does not exist for the MSAC discussed here. The MWPC can also, using high discrimination level on wires, provide fast signals from ionisation by charged particles for contribution to a first level trigger.

With a rejection factor of $10^4$ from a first level trigger, the data acquisition rate would be reduced to $10^4$ sec$^{-1}$ or one event per 100 μs. 90% data taking efficiency will thus require a maximum acquisition time of 10μs per event without data processing. The time delay of the first level trigger comprising scintillation counter arrays and fast calorimeters ( between 0.5 to 1μs) will require an equivalent storage time in the electronics. With these timing requirements, the large number of channels and the small pixel sizes, the fast Ring Imaging Technique requires the development of high density integrated electronics (VLSI) for amplification, discrimination and local buffering and readout.

### 6.3 Monte- Carlo simulation of a MWPC with cathode pad array readout.

Monte Carlo simulations of the multiwire photon detector with a pad size of 2 x 2 $mm^2$, shown in figure 27, have been performed with TEA and TMAE as photosensitive agents. The simulations were made for a large range of gain in the avalanche multiplication, to study the variation of the two-dimensional resolution and the behaviour of the detector as a function of the feedback photoelectron production.

The primary photoelectrons were uniformly generated over the pad area, whereafter the Monte-Carlo simulation followed the same process as discussed in section 4, concerning the charge development in the avalances and the feedback photoelectron production, taking a 0.6 mm photon mean free path for both TEA and TMAE. The spread of the charge over the cathode pad area was of a gaussian shape $e^{-(r^2/2d^2)}$, where d = 0.5 mm is the distance between the anode wire plane and the cathode pads. The total induced charge on the pads, due to the limited capacitive coupling, was assumed to be 20% of the anode charge .

Calculations of the response of the detector and the associated fast transconductance amplifier stage, using the well known theory of the charge development in time, show that a maximum time constant for filtering of 5 ns is allowed to keep the time jitter of the detected pulse below 10 ns after discrimination. With this time constant, the maximum of the amplifier response is reached when only 25% of the total charge of the avalanche is developed. The discriminator threshold was set to $4.5 \cdot 10^3$ electrons equivalent input charge on the pads after filtering, which corresponds to ~2$\sigma$ r.m.s noise according to recent developments on low noise fast amplifiers. This threshold corresponds to a total input charge of $5.4 \cdot 10^4$ electrons.

The number of pads hit per primary avalanche is shown as a function of the average detector gain $\bar{g}$ in figure 29. The rapid rise of the number of pads hit, because of the large production of feedback photoelectrons when using TMAE, is observed as expected from the experimental results reported. The detection efficiency for cathode pads is higher than 95% at gains above $\bar{g} = 5 \cdot 10^5$. The resolutions $\sigma_x$ and $\sigma_y$ (y is along the wire direction) are calculated from the distributions of $(x_{th} - x_{meas})$ and $(y_{th} - y_{meas})$, using the pad information only. $x_{th}$, $y_{th}$ are the coordinates of the point where the photoelectron was generated and $x_{meas}$,$y_{meas}$ the measured coordinates where the mean value is taken when more than one pad is hit. The results are shown in figure 30 as a function of the average detector gain for both TEA and TMAE. The use of TEA allows a comfortable operation of the MW detector exhibiting a remarkable stability of the resolutions $\sigma_x$,$\sigma_y$ with the gain up to $10^6$. As expected the resolution $\langle\sigma_x\rangle$ is $\sim 2/\sqrt{12} = 0.577$ mm whereas $\langle\sigma_y\rangle$ is better than $\langle\sigma_x\rangle$ (0.4 mm at $\bar{g} = 1 \cdot 10^6$) corresponding to a pixel size $\Delta_y$ = 1.4 mm. The results meet the requirements quoted in section 6.1. On the contrary ,when using TMAE the resolutions $\sigma_x$, $\sigma_y$ rapidly

degrade with increasing gain. To approach the results obtained with TEA, the detector should be operated at the minimum gain compatible with an acceptable detection inefficiency.

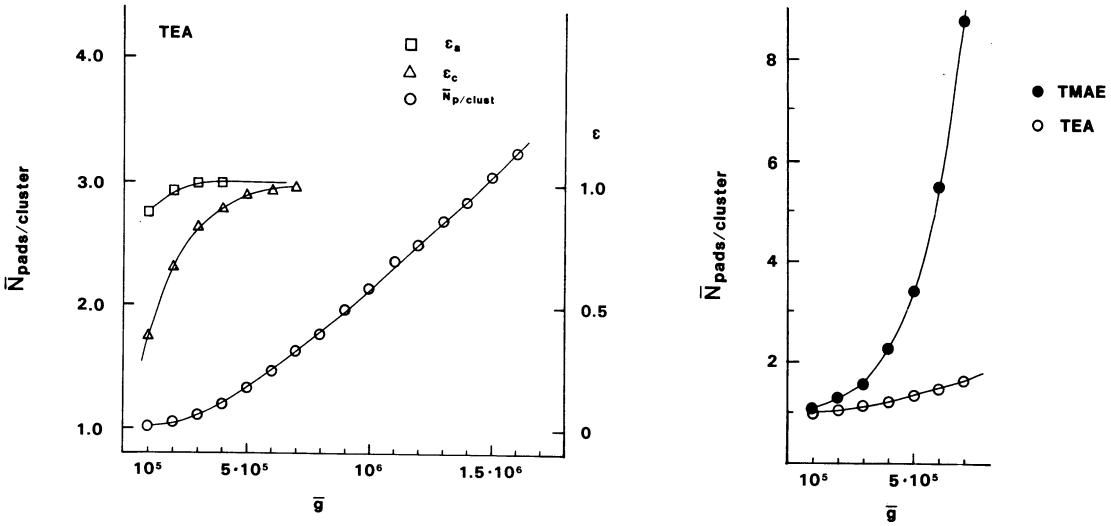


*Figure 29. The cluster size of the pad signals (number of hit pads per cluster) as functions of the average detector gain when using TEA or TMAE. The detection efficiency on the anode wires $\varepsilon_a$ and cathode pads $\varepsilon_c$ are also shown.*

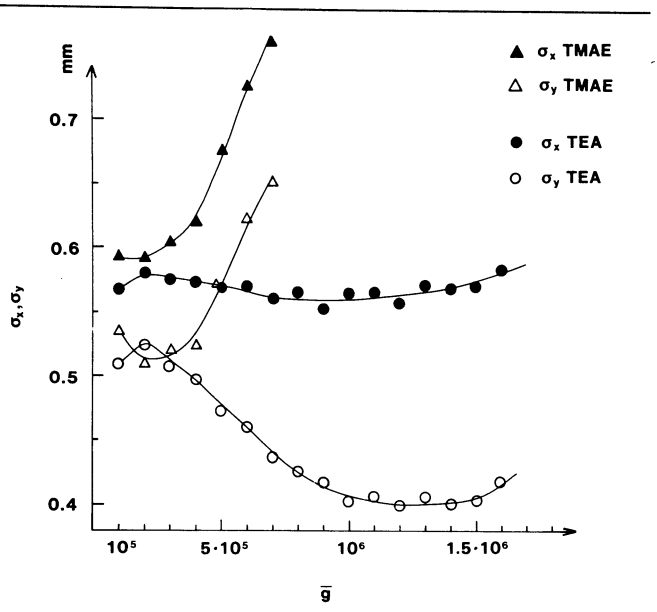


*Figure 30. The resolutions $\sigma_x$ and $\sigma_y$ ($y$ along the wire direction) as functions of the detector gain $\bar{g}$ when using TEA or TMAE.*

A comparison of the number $n_p$ of hit pads per cluster, for a detector operated at the same gain $\bar{g} = 5 \cdot 10^5$ with TEA and TMAE, is shown in figure 31. The distribution obtained with TMAE exhibits a narrow peak (64% probability for $n_p \leq 3$) of mean value $\bar{n}_p = 1.41$ and a broad distribution centred at $\bar{n}_p \approx 7$ (36% probability). With TEA one observes only a narrow distribution (97% probability for $n_p \leq 3$) of mean value $\bar{n}_p = 1.26$. This illustrates once more the advantage of using TEA instead of TMAE as the photoionizing molecule.

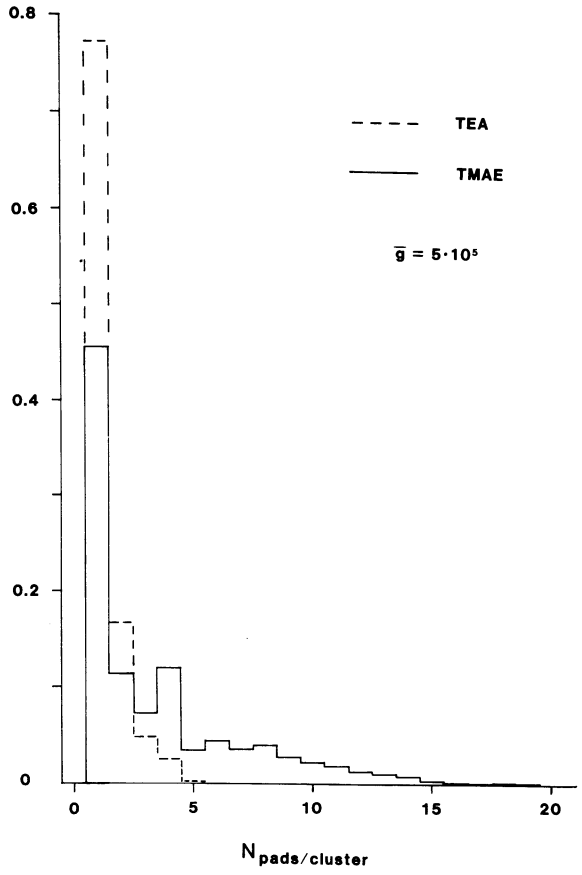


*Figure 31. The distributions of the number of hit pads per cluster for TEA and TMAE at detector gain $\bar{g}=5 \cdot 10^5$.*

## 7. Summary and conclusions.

An analysis has been made of early Cherenkov Ring Images observed with a drift-type single-photon detector, using TEA or TMAE as photoionizing vapours. The aim was to study the influence of feedback photoelectrons on the resolution and detector stability for both TEA and TMAE in a detector which does not have the optical screens between anode wires that are present in the current detectors of this type. These screens modify the influence of the feedback photoelectrons making the earlier data better suited for such studies. The experimental data has been compared with Monte-Carlo simulations.

During the avalanche process around the anode wires, excitation and rapid de-excitation of atomic levels in the detector gas result in isotropic emission of secondary U.V. photons. Photons from the three carbon lines, 6.42, 7.48 and 7.94 eV, can ionize the TMAE molecules in a Methane - TMAE mixture, while TEA can only be ionized by photons from the 7.94 eV line. The production of feedback photoelectrons causes an instability at high detector gain thus determining the attainable upper limit of the gain. It is found that the present detector can be operated at ~3 times higher gain with methane - TEA than with methane -TMAE.

The simulations show good agreement with the experimental data over more than one order of magnitude in detector gain ($1.5 \cdot 10^5$ - $1.9 \cdot 10^6$). To explain the data obtained with TEA a peak quantum efficiency of 60% had to be used. Although this quantum efficiency is in disagreement with a recent measurement by Holroyd et al [5] the value is compatible with other measurements as shown in a review of the properties of TEA and TMAE. From the experimental data we find that a merit factor $N_0$=58 $cm^{-1}$ for a detector operated with Methane - TEA can be achieved.

TEA and TMAE are compared as photosensitive agents for fast RICH detectors which can be used for particle identification in future high rate experiments where high multiplicity events demand high resolution detectors. The fast RICH detector consists of a thin multiwire detector, with pad readout, where the created photonelectrons drift perpendicular to the entrance window toward the anode wires. TEA has a short photon mean free path at NTP, giving a time dispersion for photoelectron collection of 6ns. TMAE has to be heated to 90 $^0$C to obtain such a short mean free path making the construction of the detector more difficult.

The Monte-Carlo simulations show that the larger production rate of feedback photoelectrons in TMAE deteriorates the resolution at gains necessary for full detection efficiency with presently available fast electronics. On the contrary the resolution with TEA is stable for gains of up to $1.5 \cdot 10^6$ illustrating the advantage of using TEA instead of TMAE in fast RICH detectors.

## References

[1] T. Ekelöf, J. Seguinot, J. Tocqueville and T. Ypsilantis. Physica Scripta 23 (1981) 718

[2] R. Arnold, P. Baillon, H.J. Besch, M. Bosteels, E. Christophel, M. Dracos, Y. Giomataris, J.L. Guyonnet, G. Passardi, P. Pétroff, J. Séguinot and T. Ypsilantis. NIM A270 (1988) 289

[3] Delphi Technical Proposal. Delphi 83-66, CERN, May 1983.

[4] SLD Design Report, SLAC report 274 (1984). See also M. Breidenback IEEE Trans. Nucl. Sci. NS-33 (1986) 46

[5] R. A. Holroyd, J. M. Preses, C. L. Woody and R. A. Johnson. NIM A261 (1987) 440.

[6] E. Barrelet, T. Ekelöf, B. Lund-Jensen, J. Séguinot, J. Tocqueville, M. Urban and T. Ypsilantis. ISABELLE, 1981 Summer workshop. Vol 4 page. 1378. B.N.L.-51443.

[7] D. Salomon and A.A. Scala. Jour. of Chem. Physics 62 (1975) 1469

[8] Proposal for an Electron Positron Collider for Heavy Flavour Particle Physics and Synchrotron Radiation. Paul Scherrer Institute, PR-8809, July 1988.

[9] H.D. Morgan and J.E. Mentall. Jour. of Chem. Physics 60 (1974) 4734.

[10] D.E. Donohue, J.A. Schiavone and R.S. Freund. Jour. of Chem. Physics 67 (1974) 759 and 769.

[11] L.O. Eek, T. Ekelöf, K. Fransson, A. Hallgren, P. Kostarakis, G. Lenzen, B. Lund-Jensen, J. Séguinot, J. Tocqueville and T. Ypsilantis. IEEE Trans. Nucl. Sci. NS-31 (1984) 949.

[12] R. Arnold, P. Baillon, J.D. Berst, H.J. Besch, M. Bosteels, E. Cristophel, Y. Giomataris, J.L. Guyonnet, G. Passardi, J. Séguinot, J. Tocqueville, D. Toet and T. Ypsilantis. NIM A252 (1986) 188

[13] G. Charpak and F. Sauli. Phys. Lett. 78B (1978) 523

[14] J. Séguinot and T. Ypsilantis. NIM 142 (1977) 377.

[15] J.H. Carver and P. Mitchell. Jour. Sci. Instr. 41 (1964) 555 and Jour. Opt. Soc. Amer. 57 (1967) 738.

[16] J.C. Person. Jour. Chem. Physics 47 (1965) 2553.

[17] National Bureau of Standards

[18] G. Charpak, S. Majewski, G. Melchart, F. Sauli and T. Ypsilantis. NIM 164 (1979) 419.

[19] B. Cetinkaya, G. H. King, S. S. Krishnamurthy, M. F. Lappert and J. B. Pedley. Chem. Comm. (1971) 1370.

Y. Nakato, M. Ozaki, A. Egawa and H. Tsubomura. Chem. Physics Letters 9 (1971) 615.

Y. Nakato, M. Ozaki and H. Tsubomura. Bull. Chem. Soc. Japan 45 (1972) 1299.

Y. Nakato, T. Chiyoda and H. Tsubomura. Bull. Chem. Soc. Japan 47 (1974) 3001.

[20] D. E. Anderson. NIM 178 (1980) 125 and I.E.E.E Trans. Nucl. Sci. NS-28 (1981) 842.

(TMAE was first used in a Gas Scintillator Proportional Counter by D. F. Anderson in 1980. Later in the same year it was used by us and the Charpak, Sauli group at CERN. TMBI was suggested to us by M. F. Lappert in a letter to T. Ekelöf. Dec. 1979).

[21] D. F. Anderson. NIM A270 (1988) 416.

[22] R. J. Apsimon, J. Cowell, P. S. Flower, K. A. Freeston, G. D. Hallewell, J. A. G. Morris, J. V. Morris, C. N. Paterson, P. H. Sharp, C. N. Uden, R. M. Young, M. Davenport, J. Eades, P. A. Coyle, S. Danaber, R. H. McClathey and L. F. Thompsom. NIM A421 (1985) 339.

[23] V. Ashford, T. Bienz, F. Bird, G. Crawford, M. Gaillard, G. Hallewell, D. Leith, Y. Kwon, D. McShurley, A. Nuttall, G. Oxoby, B. Ratcliff, R. Reif, D. Schultz, H. Shaw, S. Shapiro, E. Solodov, N. Toge, J. Va'Vra, S. Williams, D. Bauer, D. Caldwell, A. Lu, S. Yellin, M. Cavalli-Sforza, P. Coyle, D. Coyne, E. Spencer, R. Johnson, B. Meadows and M. Nussbaum. IEEE Trans. Nucl. Sci. NS-34 (1987) 499. (See figure 8).

[24] Y. Giomataris. Delphi 86-17 RICH 15. Feb 1986 CERN.

[25] J. Séguinot, J. Tocqueville and T. Ypsilantis. NIM 173 (1980) 283.

[26] G. Comby, Ph. Mangeot, J.L. Augueres, S. Claudet, J.F. Chalot, J. Tichit, H. Lignieres and A. Zadra. NIM 174 (1980) 93.

[27] S. Ekelin. Internal report, Royal Institute of Technology, Stockholm 1981, and K. Fransson internal group report, CRIG-16, 1981. The measurements were made in our laboratory by the Doctoral students S. Ekelin and K. Fransson. The data has been published in the below mentioned report by Barrelet et al [28].

[28] E. Barrelet, T. Ekelöf, B. Lund-Jensen, J. Séguinot, J. Tocqueville, M. Urban and T. Ypsilantis. NIM 200 (1982) 219.

[29] G. Charpak, A. Peissert, F. Sauli, A. Cavestro, M. Vascon and G. Zanella. NIM 180 (1981) 387.

[30] Ph. Mangeot, G. Coutrakon, J.R. Hubbard, J. Mullié, J. Tichit, A. Zadra, R. Bouclier, G. Charpak, J. Million, A. Peisert, J.C. Santiard, F. Sauli, C.N. Brown, D. Finley, H. Glass, J. Kirz and R.L. McCarthy. NIM 216 (1983) 79.

[31] J.J. Magenheimer and R.B. Timmons. Jour. Chem. Physics 52 (1970) 2790.

[32] H. Genz. NIM 112 (1973) 83 and references therein.

[33] R. Arnold, P. Baillon, H.J. Besch, M. Bosteels, E. Christophel, M. Dracos, Y. Giomataris, J.L. Guyonnet, G. Passardi, P. Pétroff, J. Séguinot, D. Toet, J. Tocqueville and T. Ypsilantis. NIM A270 (1988) 255

[34] H.D. Morgan and J.E. Mentall. Jour. of Chem. Physics 60 (1974) 4734.

[35] M. Dracos. Thése de Doctorat de l'Université Louis Pasteur, Strasbourg, CRN/HE-87-10.

[36] T. Ypsilantis. Physica Scripta 23 (1981) 371.

[37] P.W. Langhoff and M. Karplus. Jour. Opt. Soc. Amer. 59 (1969) 863

[38] D. Dresselhaus and R. Fohrmann. DESY 84-109.

[39] P. Fisher, A. Drees, P. Glässel, G. Lamade, H. Ries, A. Schön, H. Specht, A. Breskin, R. Chechik, Z. Fraenkel, D. Sauvage, V. Steiner, I. Tesrruya and R. Horisberger. IEEE Trans. Nucl. Sci. NS-35 (1987) 432.

# III

# THE TIME-PROJECTION RING IMAGING CHERENKOV (RICH) COUNTER — NEW EXPERIMENTAL RESULTS

The RICH Group

L. O. Eek[4], T. Ekelöf[1,4], K. Fransson[4], A. Hallgren[4], P. Kostarakis[1], G. Lenzen[5], B. Lund-Jensen[4], J. Séguinot[2], J. Tocqueville[2] and T. Ypsilantis[3]

CERN[1]-College de France[2]-Ecole Polytechnique[3]-Uppsala[4]-Wuppertal[5]

## Abstract

A TPC-type RICH-counter with a 200 × 200 mm$^2$ quartz window and a 1.27 mm wire pitch MWPC has been tested in a 10 GeV/c $\pi^-$ beam. The MWPC is equipped with optical screens (called "cloisons") between the anode wires, with the purpose of absorbing the secondary UV-photons emitted from the charge avalanches around the wires. The test results show that the cloisons effectively suppress the noise caused by the photon reemission, without affecting the detection efficiency for single photoelectrons in the MWPC.

## Introduction

In the present report we present results obtained with a new time-projection-type RICH counter in a 10 GeV $\pi^-$ test beam at the CERN PS. These new tests were performed only two weeks ago and although the progress made can be clearly demonstrated the details of the results reported here are preliminary. The off-line analysis is under way and new measurements will resume in a week.

Before describing the measurements, let us shortly outline the ultimate purpose of the present investigation which is to provide RICH counters for use in colliding beam experiments. Unlike the situation in fixed target experiments a counter in a colliding beam experiment usually is required to cover the full solid angle and, also, to be very compact. It has furthermore become clear that it is difficult to keep the inherent concentric-sphere geometry of the Cherenkov ring imaging counter when constructing a general purpose colliding-beam detector that should comprise, in addition to the RICH counter, a magnetic spectrometer and calorimeters. The solution to this problem for the gaseous radiator counter has been to divide the counter into spherical sectors, here called cupolas, which can be inserted in the experimental layout in a way that is compatible with the space requirements of the other detector components.[1] How this division is done in principle is illustrated in Fig. 1. The basic consideration in the decomposition of the spherical counter into cupolas is that the aperture of each cupola must be made sufficiently small so that the optical aberrations (which occure if the particle tracks do not pass through the center of curvature of the mirror) do not exceed the irreducible, chromatic errors in the system.[2]

The DELPHI detector[3] at LEP, shown in Fig. 2, is an example of how this decomposition can be done in practice (the heavy lines that delimit the cupolas in this figure are only drawn to indicate the apertures of the counters and do not correspond to physical walls between the gas volumes).

In Fig. 3 the UA2 experiment at the CERN proton-antiproton collider is shown equipped with a single RICH cupola in one of the endcap sectors.[4] It is planned to install this counter in summer 1984 with the aim of improving the $e/\pi$ separation capability in this sector for momenta up to about 10 GeV/c.

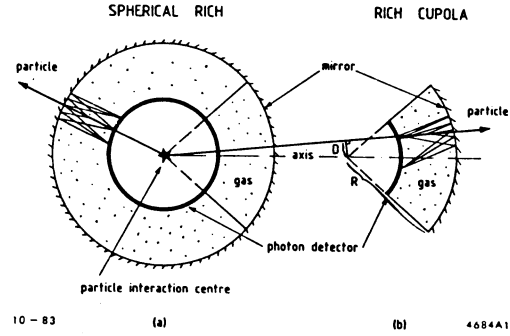


Fig. 1. (a) Ideal spherical ring imaging geometry and (b) RICH cupola geometry.

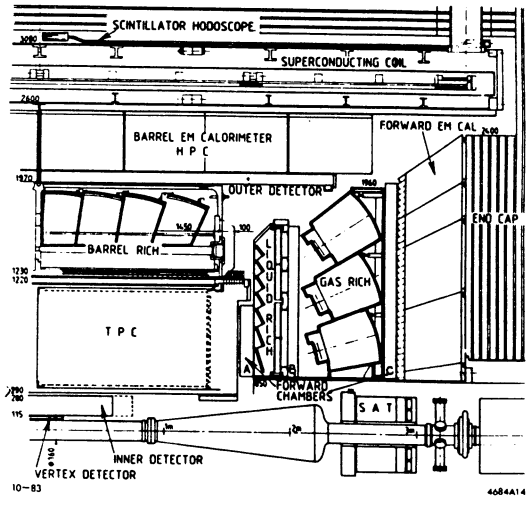


Fig. 2. Implementation of ring imaging detectors in the DELPHI spectrometer at LEP.

This paper was presented at the 1983 Nuclear Science Symposium, October 1983, San Francisco, CA.

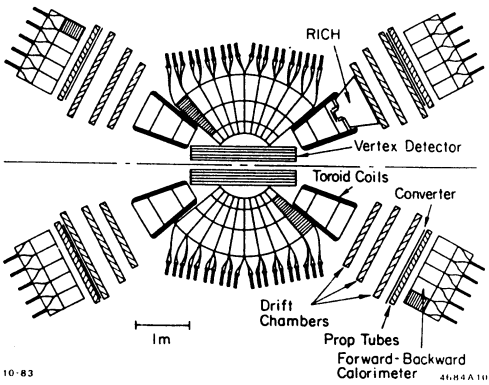


Fig. 3. Planned installation of RICH in the UA2 experiment at CERN.

The work reported here forms part of the development of RICH detectors to be used in these experiments. In particular the detector described in the present report corresponds to the short drift (20 cm), high spatial resolution detectors (wire pitch 1.27 mm) to be installed in the endcap sector in the UA2 detector and, later on, in the endcaps of the DELPHI detector.[5]

### Earlier Experience

The basic principle of the TPC-type single UV-photon position-detector as proposed and developed[6,7] by our group is illustrated in Fig. 4. The UV-photons are incident through a quartz window behind which they are absorbed, by a photoionizing vapor like TMAE (tetrakis dimethylamino-ethylene) mixed into a drift-chamber gas like $CH_4$ (80%)/iso-$C_4H_{10}$ (20%). The absorption is followed by emission of single-photoelectrons which drift in an electric field, directed parallel to the quartz window, up to a MWPC where they are detected. The drift time gives the x-coordinate and the wire address the y-coordinate.

In Fig. 5 is shown the construction of an earlier detector of this type. This detector contains two MWPC's and two drift regions, with the electron drift in opposite directions and with an insensitive slot in the middle. The drift field cage is made up of two potential wire layers, one on either side of the 5 mm thick quartz window, and a single wire layer inside the gas volume, 45 mm away from the quartz window and 100 mm away from the back wall of the drift-gas container. The maximum drift length in either of the two drift regions is about 120 mm and the MWPC has 224 wires, each with a pitch of 1.27 mm.

In Fig. 6 is shown the TPC-image, obtained from the on-line computer-display for 290 accumulated events, when operating the detector without TMAE, having the 10 GeV/c $\pi^-$ beam running through one of the two drift volumes in a direction perpendicular to the quartz window. The width of the beam spot is determined by the width of the triggered beam (5 mm diameter). The spurious tracks emerging sideways from the beam spot correspond to $\delta$-rays.

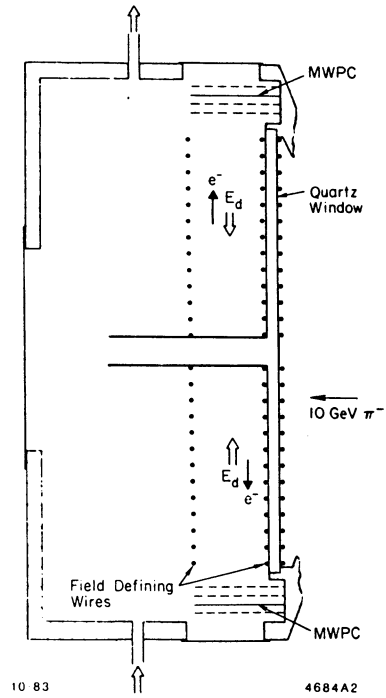


Fig. 5. Earlier TPC detector.

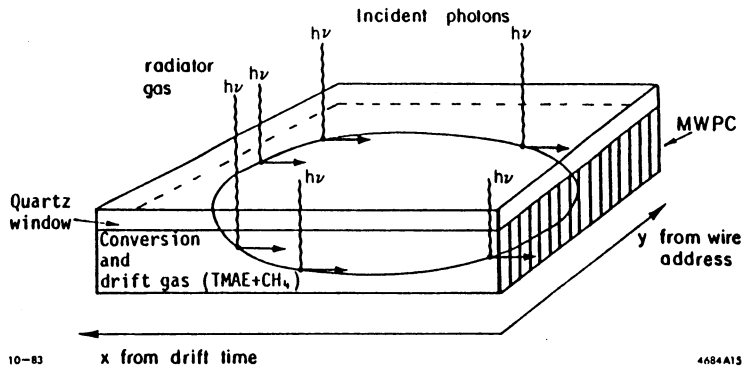


Fig. 4. The principle of TPC type photon detector.

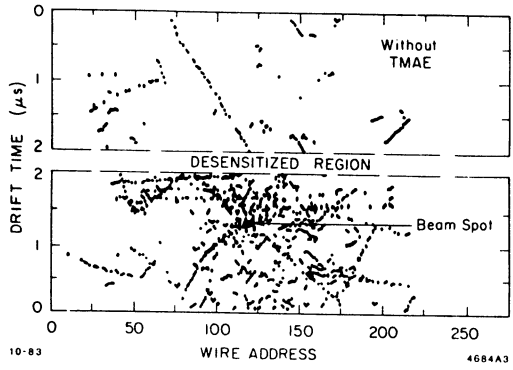


Fig. 6. Beam spot without TMAE in detector without cloisons.

In Fig. 7 the same type of data are shown, with the only difference that in this case the detector gas contained about 0.7 torr partial pressure of TMAE. A dramatic blow-up of the beam spot can be seen with a tendancy of forming a halo towards later arrival times. The explanation for this phenomenon is that when the ionization created by the passage of the charged particle reaches the anode wires UV-photons are emitted from the charge avalanche around the wires. These secondary UV-photons are then converted to electrons in case TMAE is present. The mean free path for UV-photon absorption in 0.7 torr of TMAE is about 12 mm and the background photoelectrons are therefore spread around, on average, by this distance and tend to arrive to the MWPC at a later time than the primary beam track ionization. On average there were about 20 background points per beam track created in this way. The beam track produced a dE/dx-charge of about 250 electrons over the 45 mm track length in the drift volume, and the probability for obtaining a background point through this mechanism is thus of the order of 8% per electron.

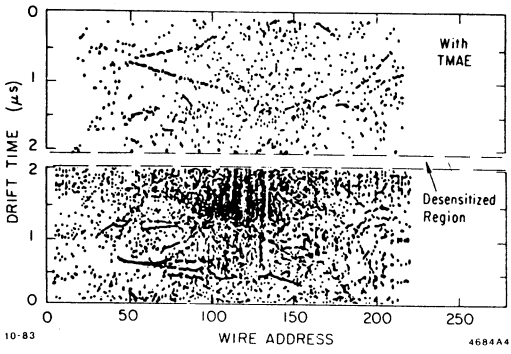


Fig. 7. Beam spot with TMAE in detector without cloisons.

In order to verify the understanding of this background and to seek for a solution how to suppress it, small UV-light-absorbing walls were installed between the anode wires in a small 2.54 mm wire pitch detector. In a first approach, in which the walls were made of insulating material, the detection efficiency of the chamber was drastically reduced, owing to field distortions around the anode wire. It was concluded that these distortions were due to charges being accumulated on the separating walls. Making the separating walls conductive by deposition of a thin layer of carbon did not solve the problem. The conclusion was that having insulating or equipotential separating walls did not lead to an efficient collection field around the anode wire, at least not in the particular geometry chosen which had a comparatively small angular opening (±23°) between the endpoints of the walls, as viewed from the anode wire (this angle should be small in order to minimize the solid angle over which reemitted photons are not absorbed by the walls).

The final solution tried was to use separating walls (cloisons), made of thin printed circuit boards with thin conductive lines running parallel to the anode wires along the two surfaces of the board. Equipping a limited region of the 2.54 mm pitch MWPC, it was found that the voltages on these lines could be tuned so to obtain a fully efficient charge collection in the MWPC from beam tracks.

### The New Detector

On the basis of this experience the detector shown in Fig. 8 was constructed. In this case the 5 mm thick quartz window is 200 × 200 mm$^2$. The thin back wall of the drift-gas container is mounted only 40 mm away from the quartz window and supports a layer of parallel printed circuit lines on either side of the wall. In Fig. 9 the drift box with flanges for the radiator container (down) and for the MWPC (front) is shown in perspective.

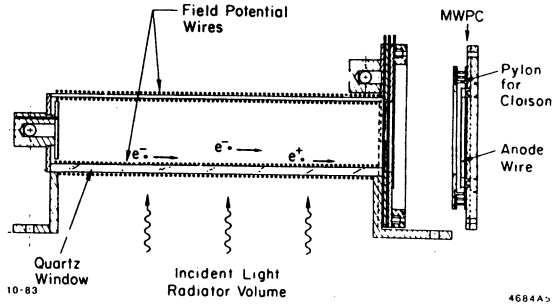


Fig. 8. The new detector with cloisons.

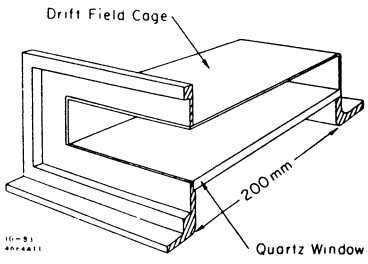


Fig. 9. Perspective view of drift box.

The MWPC has an anode wire pitch of 1.27 mm and is equipped with cloisons. Figure 10 shows in three views the construction of the support for the wires and the cloisons in the MWPC. The 10 $\mu$m diameter anode wires are soldered on 0.6 mm wide holders, consisting of copper-wire hooks, surrounded by plastic insulator. The signals are led through these hooks to the backside of the cathode plane on which the preamplifiers are mounted on small IC-sockets.

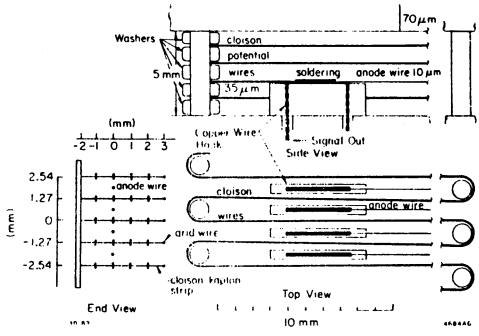


Fig. 10. Details of the cloison (blind) picket fence.

The cloisons consists of 5 mm wide and 30 $\mu$m thick Kepton strip, mounted between the anode wires. The potential on the surface of the Kepton strip is controlled by eight 35 $\mu$m diameter stainless-steel wires, running along the surface of each strip, four wires on either side, with a distance between adjacent wires on one side of 7 mm (see Fig. 10). The wires are stretched around small ceramic pylons and are kept in place by small washers. The pylons are mounted between two metallic frames outside the anode-wire holders with one pylon behind every second such holder allowing eight single potential wires of about 10 m length to be wound around the endpoints of the anode wires in a serpentine-like manner. The high voltages applied at the endpoints of these wires thus simultaneously control the electrostatic field around all anode wires in the MWPC. Mechanically the cloison strips are kept in place by the potential wires. Finally, a single wire grid is mounted on top of the MWPC, adding a 70 $\mu$m diameter wire on the top-edge of each cloison. The "cell" around one anode wire thus consists of five potential wires at a height of $-1$, 0, $+1$, $+2$ and $+3$ mm with regard to the anode and at a lateral distance of $\pm 0.6$ mm. A cathode plate is mounted at -2 mm, below the anode wire. The opening angle between the upper borders of the cloisons, as viewed from the anode wire, is $\pm 13°$, leaving only a very small solid angle over which the photons are not absorbed by the cloisons ($\sim 7\%$).

### Results of Beam Tests

In a first series of runs at the CERN PS, performed in the $\ell_9$ beam line in the East Area with 10 GeV/c negative particles, the homogeneity of the drift field inside the field-cage was investigated by recording straight beam tracks traversing the drift volume parallel to the quartz window. A single straight beam track is shown as recorded in Fig. 11. By placing the detector in a series of different positions in the beam, thus scanning the drift volume, it was found that the collection of the beam ionization was complete also in case when the beam was running close to the quartz window or near the back wall at the drift volume. This is illustrated in Fig. 12 in which it can be seen the number of wires hit per beam track is independent of beam position as long as the whole beam is inside the drift region. (The successive drop-off at the end of the distribution are due to the finite size, 5 mm diameter, of the beam. The small slope of a few percent seen in the drift direction scan is probably due to the electric field being directed slightly away from the side walls of the drift cage when approachig the MWPC.)

The square of the average residue distance of a point from the fitted straight line (Fig. 11) is shown in Fig. 13 as function of longitudinal drift distance from the MWPC. The residue is expressed in units of nanoseconds. With a drift velocity of 65 mm/$\mu$sec one may conclude that the residue per point increases from about 0.45 mm to about 0.6 mm when scanning over the drift region. This increase is compatible with being due to diffusion.

In a second series of runs the photon detector was mounted on the radiator gas vessel which was filled with isobutane (containing less than $5 \times 10^{-4}$ impurities, further purified through Oxisorb). The focussing mirror is a polished spherical glass mirror with a focal length of f = 500 mm, coated in vacuum with 90 nm A$\ell$ and 35 nm $MgF_2$. The detector gas (80% $CH_4$, 20% iso $C_4H_{10}$) was bubbled through TMAE at 28°C. The

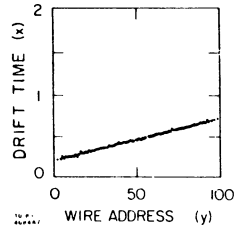


Fig. 11. Event with a single straight beam track.

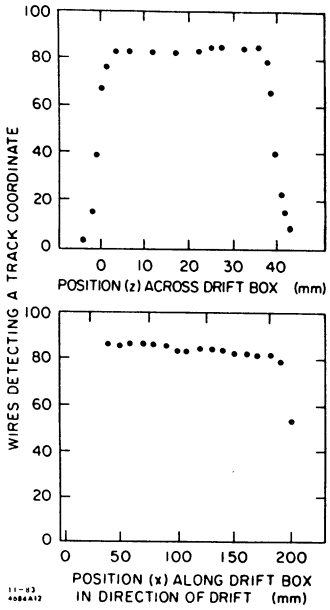


Fig. 12. Number of wires hit per beam track versus position.

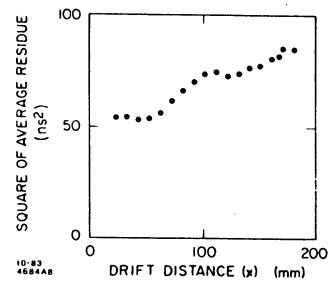


Fig. 13. Residual squared from straight line versus drift distance from MWPC.

beam was incident slightly off the optical axis of the system (impact parameter x = 0.05).

In Fig. 14 the on-line display of the first 300 events recorded is shown. The Cherenkov ring and the beam spot, limited to the size of the triggered beam (5 mm diameter), are clearly distinguished. Also seen are the $\delta$-ray background and some remaining ionization from early beam-tracks (vertical line down from the beam spot – the two circular lines are fiducial limits drawn by the computer).

In Fig. 15 three individual event-displays from the first run are shown. The beam spot is limited to about four adjacent wires. Moving the beam spot to the other side of the ring, close to the MWPC, reduced the size to about two wires. The number of photons per event was about six in this first run. After some further optimization of the MWPC high voltages an average of about 10 photons per event was obtained.

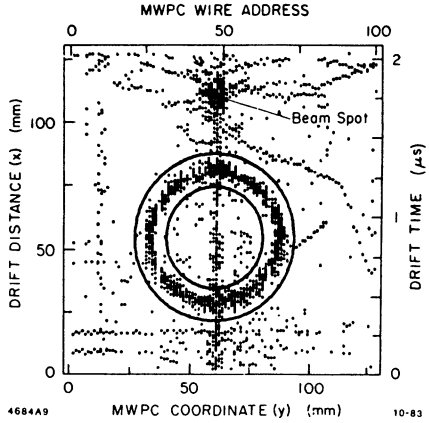


Fig. 14. Online display of first 300 events.

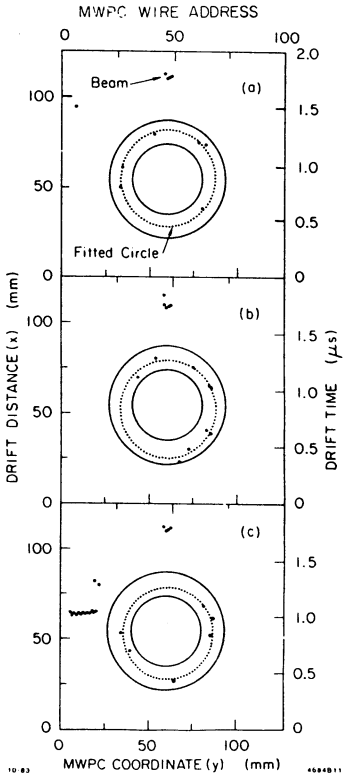


Fig. 15. Three individual events with the beam in the detector.

Figure 16 shows three individual events recorded under these conditions (in this case the beam had the same direction as in the first run but it had been moved out of the photon detector). With an effective radiator length of 47.5 cm and a Cherenkov angle of 54 mrad this corresponds to a $N_0$ value of about 72

$cm^{-1}$. Further optimization of $N_0$, as well as a detailed study of the Cherenkov angular resolution, will be carried out in future runs.

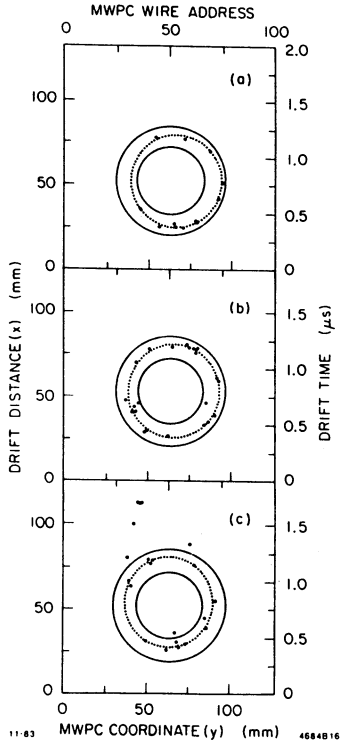


Fig. 16. Three events with the beam out of photon detector and a mean number of detected photons of 10 per event.

## Conclusions

The first test results obtained with the new TPC-type single-photon position-detector show that using thin dielectric walls (cloisons) with field-defining wires running along the surface to screen optically the anode wires from each other makes it possible to detect the charged particle ionization ($\sim$ 250 electrons) and the single photoelectrons simultaneously side by side. The measurements indicate no loss in the single-photoelectron detection efficiency. Furthermore, the drift cage consisting on all sides of thin dielectric walls with narrow field-defining strips or wires (the ratio of the strip or wire width to the pitch is smaller than 1:10) is found to produce a drift-field of satisfactory uniformity inside the whole volume.

## Acknowledgements

The new detector presented in this report has been designed in collaboration with and constructed by the EP Technical Assistance Group at CERN. For this we are in particular endebted to G. Muratori, D. Bérnier, J. Lecoultre and C. Rivoiron of this group. We also wish to thank G. Vismara who constructed the amplifying and discriminating electronics used in these measurements and R. Bouhot, our group technician, for unvaluable assistance at all phases of our experimental work. The work has been realized under the auspices of the EP Division at CERN, led by Professors E. Gabathuter and A. Wetherell.

## References

1. T. Ekelöf, "Applications of the RICH Technique," Proceedings of the EPS High Energy Physics Conference, Brighton, UK, 20-27 July 1983.
2. T. Ypsilantis, Phys. Scripta 23, 370 (1981).
3. The DELPHI Collaboration, DELPH Technical Proposal, CERN/LEPC/83-3, LEPC/P2, 17 May 1983, CERN, Geneva, Switzerland.
4. P. Baillon, L. O. Eek, T. Ekelöf, K. Fransson, A. Hallgren, A. Litke, B. Lund-Jensen, J. Tocqueville, J. Séguinot and T. Ypsilantis, "The Installation and Use of a Ring-Imaging Cherenkov Counter in the UA2 Experiment to Measure Inclusive Electron Production of Transverse Momenta Up to About 5 GeV/c," CERN/SPSC/82-55, SPSC/T24, 28 June 1982, CERN, Geneva, Switzerland.
5. D. Bernier, A. N. Diddens, L. O. Eek, T. Ekelöf, K. Fransson, A. Hallgran, B. Koene, B. Lund-Jensen, G. Muratori, C. Rivoiron, J. Séguinot, J. Tocqueville and T. Ypsilantis, "The DELPHI end-cap RICH counters, COLLEPS 82-23, May 1982, CERN, Geneva, Switzerland.
6. T. Ekelöf, J. Séguinot, J. Tocqueville, M. Urban and T. Ypsilantis, Phys. Scripta 23, 718 (1981).
7. E. Barrelet, T. Ekelöf, B. Lund-Jensen, J. Séguinot, J. Tocqueville, M. Urban and T. Ypsilantis, Nucl. Instrum. Methods 200, 219 (1982).

# IV

Nuclear Instruments and Methods in Physics Research A252 (1986) 418–422
North-Holland, Amsterdam

# OPERATION OF RICH SINGLE-PHOTON DETECTORS WITH OPTICALLY SHIELDED WIRES IN TRANSVERSE MAGNETIC FIELDS

W. DULINSKI [2,3], L.O. EEK [4], T. EKELÖF [4], K. FRANSSON [4], A. HALLGREN [4], P. KOSTARAKIS [1], G. LENZEN [5], P. LORENZ [5], B. LUND-JENSEN [4], J. MICHALOWSKI [2] and M. TURALA [2]

[1] *CERN, Geneva, Switzerland*
[2] *Institute of Nuclear Physics, Cracow, Poland*
[3] *Centre de Recherches Nucleaires, Strasbourg, France*
[4] *University of Uppsala, Uppsala, Sweden*
[5] *University of Wuppertal, FRG*

The operation of TPC-type photon detectors with optical shields between the sense wires has been investigated in magnetic fields up to 1.4 T. The field was applied perpendicularly to the drift direction. Three types of MWPCs with different optical shield designs were tested. Ethane and iso-butane were used as drift gases. TMAE vapour was added to obtain photon sensitivity.

The results show that MWPCs with printed circuit board shields can be operated without loss of efficiency even at high magnetic fields. The MWPC with tubular cathode shows losses already at low fields.

## 1. Introduction

TPC-type photon detectors (fig. 1) are used in Ring-Imaging-Cherenkov counters [1–4]. An economically feasible design implies the use of quartz for the UV transparent window. Due to the quartz cutoff at 7.6 eV one needs a photo-sensitive agent with low photo-ionization threshold and high quantum efficiency. A possible choice is tetrakis–(dimethylamine)–ethylene (TMAE) with a threshold of 5.4 eV. However, since TMAE has a relatively long mean free path for UV-photon absorption (12 mm at typical operating conditions) the creation of secondary photons in the charge avalanche around a wire leads to background signals with a consequently large spread. In ethane one expects around 40 background signals from this process over a typical 4 cm track length when a charged particle traverses the drift volume. This should be compared to a typical Cherenkov signal of about 10 photo-electrons. Such background has indeed been seen [5].

A solution to the background problem is optical shields between the wires [3,5]. This leads to several possible MWPC designs. We have tested
- a tubular cathode structure (fig. 2)
- printed-circuit (PC-) board shields (fig. 3)

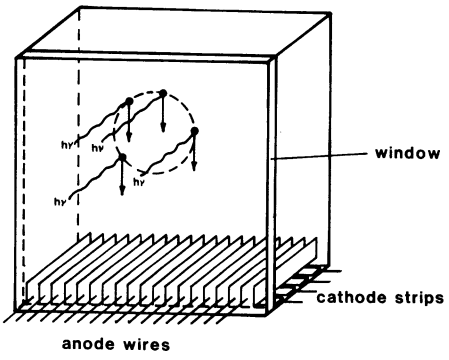


Fig. 1. Principle of RICH TPC-type photon detector.

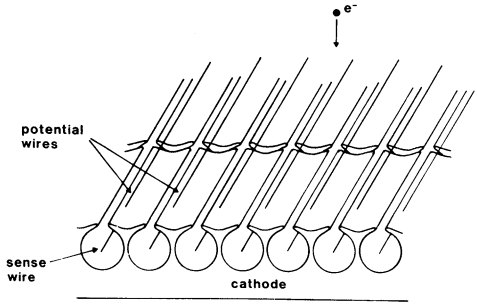


Fig. 2. Tubular-cathode MWPC.

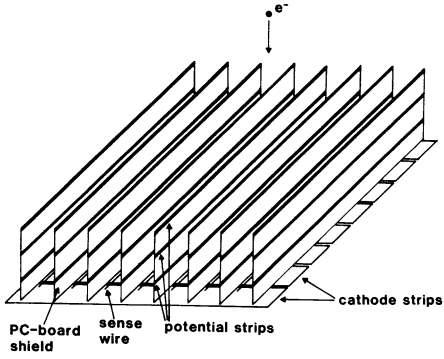


Fig. 3. MWPC with PC-board shields.

and built operational single photon detectors, with reduced background, of both types.

This solution, however, may create problems when such MWPCs are to be operated in high transverse magnetic fields, such as foreseen for the Forward RICH in the DELPHI detector at LEP: Photo-electrons could be lost drifting into the optical shields.

We have therefore measured the collection efficiency for single photo-electrons with magnetic fields up to 1.4 T for the two above mentioned MWPC types. We also tested a different MWPC with PC-board shields, where the wires (and shields) were turned 90°.

## 2. Test setup

The test setup is schematically shown in fig. 4. The photon detector consists of a $20 \times 20 \times 4$ cm drift volume with Kapton * covered epoxy walls and a UV-transparent window. The electrical drift field is defined by potential wires around the window and copper strips on the Kapton foil. Photo-electrons drift into a MWPC where two of the coordinates are defined by the wire number and the drift time. The third coordinate can be obtained from the induced cathode pulse. The gas for the photon detector bubbled through a TMAE bath at room temperature ($(18 \pm 2)$°C), giving $(0.3 \pm 0.05)$ Torr of TMAE vapour pressure. This corresponds to $(27 \pm 4)$ mm mean free path [6]. The MWPC of the photon detector was easily replaceable allowing several types to be tested.

The photon detector was placed inside a magnet with the magnetic field perpendicular to the quartz window. The calibration of the field was made using a

* Kapton is a registered trade-mark of DuPont de Nemours.

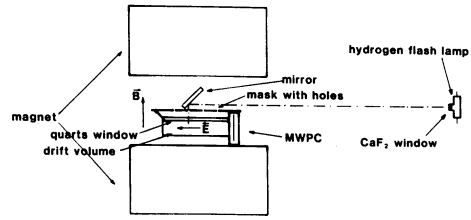


Fig. 4. Test setup.

Hall probe. A hydrogen flash lamp, placed 5 m away, shone through a mask with 1 mm diameter holes placed 2 cm away from the quartz. The light intensity of the lamp was such that in each hole on average 2 out of 5 flashes gave a detectable photo-electron. A pickup circuit on the lamp discharge-capacitor gave trigger signals to the time-digitizing system and the read-out computer. Software cuts, around the hole images, were used in the analysis to reduce background. Wire and time distributions for typical images are shown in fig. 5.

The photon-detection efficiency was defined as the number of triggers with at least one detected signal within the hole divided by the total number of triggers. This efficiency was normalized to 1 at zero magnetic field. In order to select operating voltages for each gas mixture and MWPC the efficiency at zero magnetic

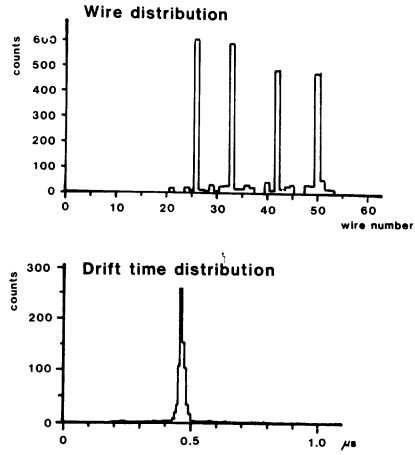


Fig. 5. Typical wire and time distributions before software cuts. These distributions were obtained with four open holes in the mask. The holes had the same drift time coordinate but different wire coordinates, thus giving four peaks in the wire distribution. The distributions correspond to 2000 triggers.

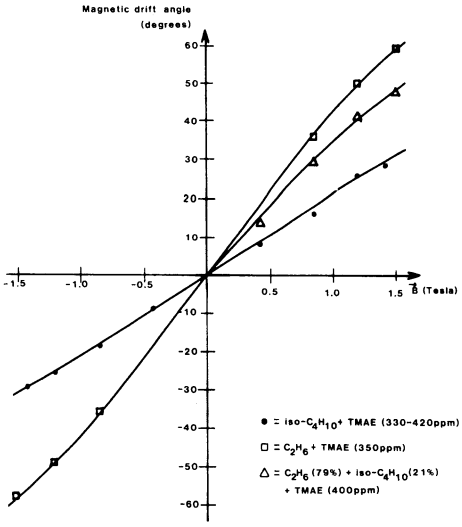


Fig. 6. Drift angle ($\alpha$) as a function of magnetic field. Lines, being guides for the eye, are least square fits of tan($\alpha$) as a linear function of B and $B^3$.

field was measured as a function of the applied voltages.

Throughout the measurements an electric drift-field of 1.0 kV/cm was used.

### 2.1. *Drift velocities and magnetic drift angles*

For these measurements two of the 1 mm holes, 2 cm apart along the drift-time coordinate, were open. The drift velocities were given from the drift-time difference over the 2 cm at zero magnetic field. The following results were obtained for the gas mixtures used:

$C_2H_6$ + TMAE (350 ppm) : 5.3 cm/$\mu$s,

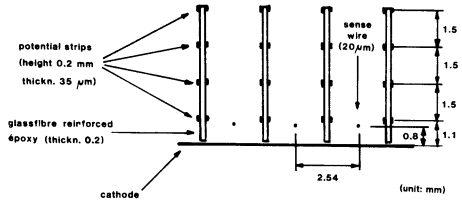


Fig. 7. Cell layout for the MWPC with PC-board shields parallel to the magnetic field.

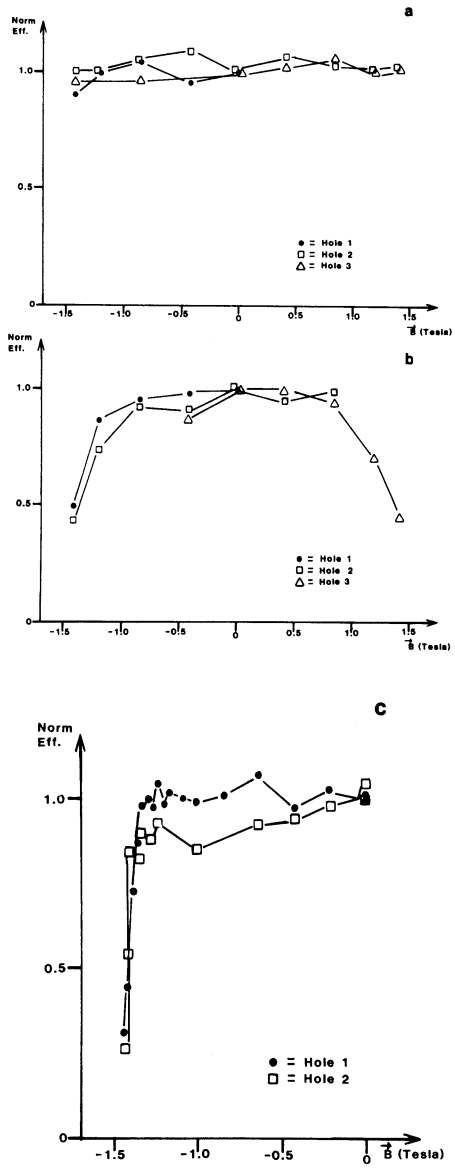


Fig. 8. Detection efficiency as a function of magnetic field for the MWPC with PC-board shields parallel to the field (lines between points are guides for the eye only): (a) With iso-$C_4H_{10}$ + TMAE. Potential step between strips is 600 V. (b) With $C_2H_6$ + TMAE. Potential step between strips is 600 V. (c) With $C_2H_6$ + TMAE. Optimized voltages.

$C_2H_6$ (79%) + iso-$C_4H_{10}$ (21%) + TMAE (400 ppm) :4.9 cm/$\mu$s,
iso-$C_4H_{10}$ + TMAE (330 – 420 ppm) :3.4 cm/$\mu$s.

When a magnetic field is applied, the images of the holes move to different wire-coordinates. The split of the two coordinates compared to the 2 cm gives the drift angle. Measured drift angles as a function of the magnetic field for the three gas mixtures are shown in fig. 6.

### 2.2. MWPC with PC-board shields parallel to the magnetic field

The design is shown in fig. 7. Between the sense wires are PC-board shields of glassfibre reinforced epoxy with copper strips. The four strips on each side of the shield run parallel with the sense wires.

The chamber was tested with iso-butane and ethane, using a 600 V step between strips. With iso-butane and −2.1 kV on the cathode and the strip closest to the sense wire, no loss in the detection efficiency caused by the magnetic field was seen (fig. 8a). With ethane and −1.75 kV, losses for high magnetic fields were observed (fig. 8b). The voltages were then optimized at 1.3 T and the following settings were obtained: cathode at −1.45 kV, strips from the one closest to the wire to the one on top of the shield at −1.95 kV, −2.85 kV, −3.7 kV and −4.1 kV, respectively, Fully efficient operation was then maintained up to this magnetic field (fig. 8c). At higher fields the efficiency drops rapidly.

### 2.3. MWPC with PC-board shields perpendicular to the magnetic field

In this MWPC (fig. 9) [7] the coordinate, which in the previously described MWPC was given by the wire

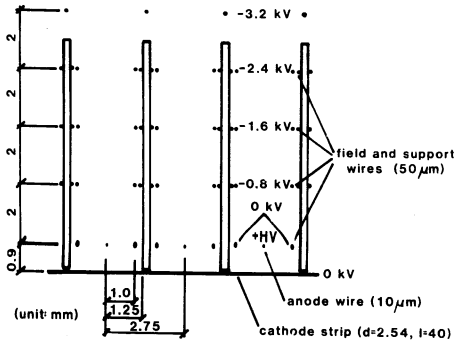


Fig. 9. Cell layout for the MWPC with PC-board shields perpendicular to the magnetic field.

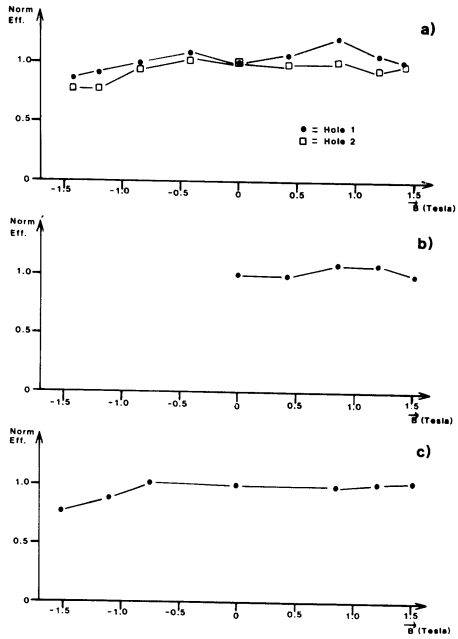


Fig. 10. Detection efficiency as a function of magnetic field for the MWPC with PC-board shields perpendicular to the field (lines between points are guides for the eye only): (a) With iso-$C_4H_{10}$ + TMAE. (b) With $C_2H_6$ (79%) + iso-$C_4H_{10}$ (21%) + TMAE. (c) With $C_2H_6$ + TMAE.

number, is now given by the cathode strip number. Measurements in magnetic fields were made for three different drift gases: ethane, iso-butane and a mixture of 79% ethane, 21% iso-butane (figs. 10c, 10a, 10b). As expected for this configuration, no significant losses in detection efficiency were seen.

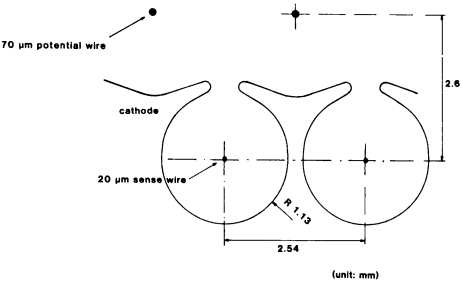


Fig. 11. Cell layout for the tubular cathode MWPC.

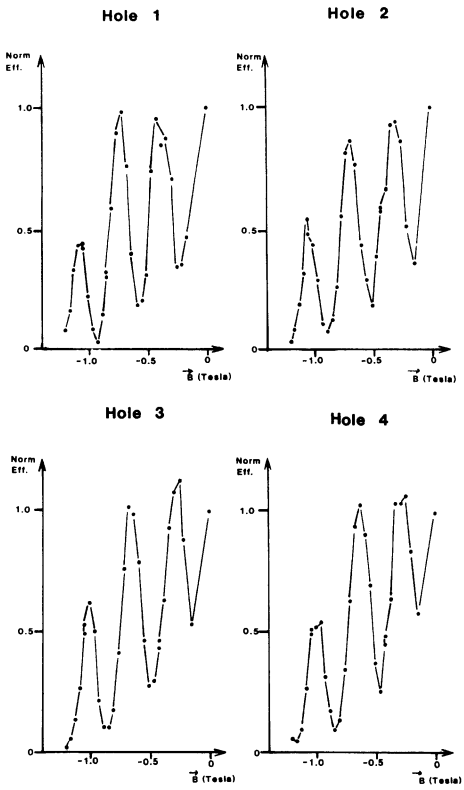


Fig. 12. Detection efficiency as function of magnetic field for the MWPC with tubular cathode. Measurements were done using four different holes in the mask. Lines between points are guides for the eye only.

### 2.4. *MWPC with tubular cathode*

The cathode consists of eight 5 mm wide stainless steel bars, where the tubular structure is cut out by electro-erosion. Potential wires are placed above the cathode in order to focus the drift of electrons through the slits (fig. 11). The measurements were made using iso-butane. Voltages were: cathode at −2.0 kV and potential wires at −3.3 kV. Losses were observed already at 0.15 T (fig. 12). The periodicity reflects the wire pitch. Changing the focusing potential in the range −2.7 kV to −3.9 kV did not change the detection efficiency. Previous tests (at zero magnetic field) had shown that the detection efficiency does not depend on the position of the hole with respect to the wires.

## 3. Conclusions

We have tested three types of MWPCs with different types of optical shields, using ethane or iso-butane as well as mixtures thereof. The MWPCs with PC-board shields have been successfully operated in transverse magnetic fields larger than the 1.2 T foreseen for the Forward RICH in the DELPHI detector at LEP.

The MWPC with tubular cathode could, in the tested configuration, not in an efficient way be operated in strong transverse magnetic fields. However, we plan to test a version of this type of MWPC with the wires perpendicular to both the electric and magnetic fields. We believe that such a MWPC could be made operational.

## Acknowledgements

We wish to acknowledge the aid and encouragement of Dr G. Damgaard and Dr O. Botner of the Niels Bohr Institute and the fruitful discussions with Dr H.J. Besch, Dr J. Séguinot and Dr T. Ypsilantis of College de France. The technical assistance of R. Bouhot, P. Dam and the Institute workshop in Uppsala, under L. Mattsson, was very important in this work, and to them we express our thanks.

## References

[1] T. Ekelöf, J. Séguinot, J. Tocqueville and T. Ypsilantis, Phys. Scripta 23 (1981) 718.
[2] E. Barrelet, T. Ekelöf, B. Lund-Jensen, J. Séguinot, J. Tocqueville, M. Urban and T. Ypsilantis, Nucl. Instr. and Meth. 200 (1982) 219.
[3] L.O. Eek, T. Ekelöf, K. Fransson, A. Hallgren, P. Kostarakis, G. Lenzen, B. Lund-Jensen, J. Séguinot, J. Tocqueville and T. Ypsilantis, IEEE Trans. Nucl. Sci. NS-31 (1984) 949.
[4] R.J. Apsimon et al., Rutherford lab. int. rep., RAL-84-131.
[5] J. Séguinot, "RICH counters", Academic training program, CERN 1982-1983.
[6] D.F. Anderson, IEEE Trans. Nucl. Sci. NS-28 (1981) 842.
[7] W. Dulinski, L.O. Eek, T. Ekelöf, K. Fransson, A. Hallgren, P. Kostarakis, G. Lenzen, P. Lorenz, B. Lund-Jensen, J. Michalowski, G. Polok and M. Turala, to be published.

# V

Nuclear Instruments and Methods in Physics Research A257 (1987) 580–586
North-Holland, Amsterdam

*Section III. Particle identification*

# PRELIMINARY ANALYSIS OF THE PERFORMANCE OF A RICH COUNTER FOR LOW-$p_T$ ELECTRON IDENTIFICATION AT THE CERN $p\bar{p}$ COLLIDER

O. BOTNER [2], L.O. EEK [2], T. EKELÖF [1,2], K. FRANSSON [2], A. HALLGREN [1,2], P. KOSTARAKIS [1,3], G. LENZEN [4] and B. LUND-JENSEN [2]

[1] *CERN, Geneva, Switzerland*
[2] *Gustaf Werner Institute, University of Uppsala, Sweden*
[3] *Nuclear Research Centre Demokritos (NRCD), Athens, Greece*
[4] *University of Wuppertal, Wuppertal, FRG*

A ring-imaging Cherenkov (RICH) counter with a 60 cm long freon ($C_2F_6$) gas radiator has been used inside the UA2 detector at the CERN SPS $p\bar{p}$ Collider, the aim being to measure the amount of promptly produced electrons in the $p_T$ region 1–3 GeV/$c$. About 800000 events were recorded and the analysis is in progress. Results from a first analysis of a limited event-sample indicate that it will be possible to reach an $e/\pi$ rejection power of at least $10^{-4}$ with the RICH counter.

## 1. Introduction

The yield of prompt electrons in hadron–hadron collisions in the transverse momentum ($p_T$) region of one to several GeV/$c$ has been extensively measured at ISR energies [1]. The magnitude of the measured yield is compatible with the origin of the prompt electrons being predominantly due to heavy-quark production. This fact is illustrated in fig. 1, which shows results from measurements of the ratio of prompt electrons to charged pions as a function of $p_T$ obtained in five different ISR experiments. The data are compared with the electron yields expected from different sources, including charm and beauty decays.

Here we report on an experiment designed to measure the prompt-electron yield at SPS $p\bar{p}$ energies in the

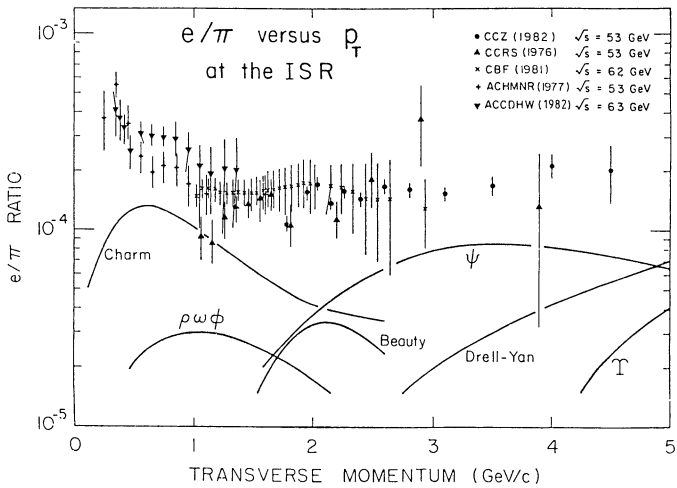


Fig. 1. Data on prompt electron production, normalized to the $\pi$ yield, from five different ISR experiments (see ref. [1]). The curves represent estimates of the contribution of different sources to the prompt electron yield.

0168-9002/87/$03.50 

$p_T$ region 1–3 GeV/$c$. For the identification of the electrons we have used a gaseous-radiator ring-imaging Cherenkov (RICH) counter [2], developed by us. This is the first time that a RICH counter has been used in a collider experiment. The main data-taking run was carried out in November–December 1985, and the data analysis is in progress. In the present paper we give a short description of the experimental apparatus and a preliminary report on its performance evaluated through a first analysis of a limited sample of the collected data.

## 2. Experimental setup

The measurements were carried out using, in conjunction, the RICH counter and the UA2 detector [3] at the CERN $p\bar{p}$ Collider. Fig. 2 shows a cross-section of the experimental layout, with the RICH counter installed in one of the 12 azimuthal sectors of the proton downstream end-cap in UA2. The outgoing line in the figure illustrates the trajectory of an electron produced at the beam collision centre. The electron traverses, in succession, a cylindrical vertex chamber (drift chambers and MWPCs), a silicon (Si) semiconductor array and two scintillator hodoscopes for $dE/dx$ measurements, a toroidal magnetic field, the RICH counter, three planar drift chambers (three coordinates measured in each chamber), a lead converter, a MWPC (tubes), and finally hits an electromagnetic calorimeter.

A closer view of the RICH counter is shown in fig. 3, which also illustrates how the photons radiated by the traversing electron are reflected from the spherical mirror to form a ring-image just behind the window of the TPC-type single-photon position detector. The radiator volume between the photon detector and the mirror is filled with a freon gas, $C_2F_6$, at atmospheric pressure. The contamination of oxygen and water in this gas was continuously monitored and was found to be at most 20 ppm $O_2$ and 5 ppm $H_2O$. The refractive index of the radiator is $n = 1.0008$ in the VUV region, implying a $\pi$ threshold momentum of 3.5 GeV/$c$ and a Cherenkov angle of 40 mrad for fully relativistic particles. The spherical mirror, which has a radius of curvature of 1.2 m, is fabricated from 3 mm thick slumped and polished glass; this glass is coated, by vacuum evaporation, with 80 nm Al and 35 nm $MgF_2$. The detector window is made of 5 mm thick $CaF_2$. The TPC volume behind the window is 4 cm deep, and is filled with $CH_4$ containing an admixture of 0.6‰ TMAE $\{C_2[N(CH_3)_2]_4\}$.

Pure $C_2F_6$, $CaF_2$, and $CH_4$ are all transparent up to photon energies of 8.6 eV (cut-off set by $CH_4$), and the photoionization threshold of TMAE is at 5.4 eV. The counter is thus designed to be sensitive for photons in the range 5.4–8.6 eV, corresponding to the wavelength region 145–230 nm.

The essential features of the TPC single-photon position detector are illustrated in fig. 4a. The UV photons enter through the $20 \times 20$ cm$^2$ $CaF_2$ window and ionize

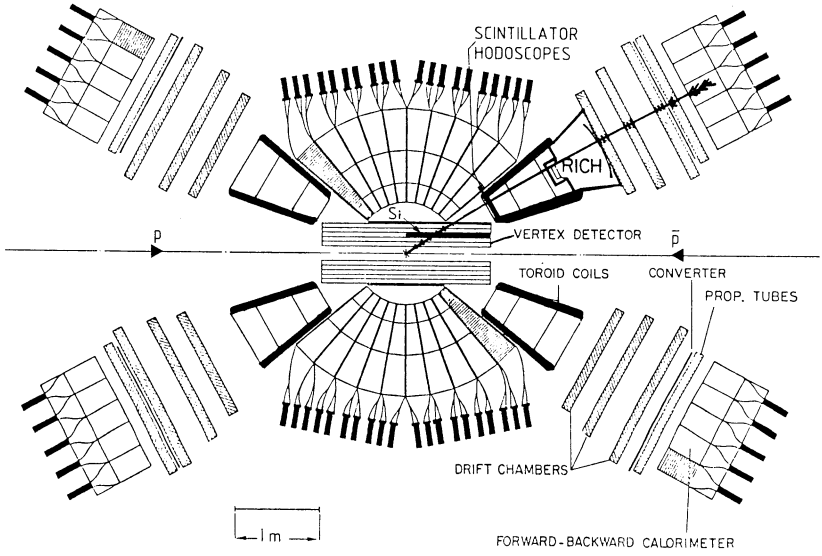


Fig. 2. Layout of the UA2 experiment at the CERN $p\bar{p}$ Collider showing the position of the RICH counter.

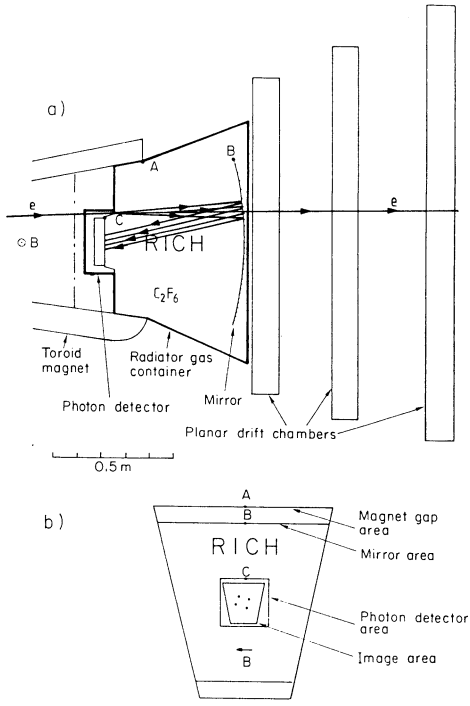


Fig. 3. (a) Cross-section of the RICH counter in UA2 showing the photon detector, the spherical mirror, and the radiator-gas container. (b) A cross-section of the RICH aperture as viewed from the $p\bar{p}$ collision point with four photon hits indicated.

TMAE molecules in the detector gas (photon mean free path about 12 mm). Owing to an electric gradient of about 0.5 kV/cm generated in the TPC volume by a surrounding field-wire cage, the liberated photoelectrons drift parallel to the window, with a speed of about 9.5 cm/$\mu$s, up to a MWPC.

Fig. 4b shows a schematic picture of the MWPC in two projections. The anode wires, which are directed perpendicularly to the $CaF_2$, are surrounded by the tubular cathodes that have 0.5 mm wide slits through which the electrons drift, guided by potential wires positioned on both sides of a slit. There are 80 anode wire of 20 $\mu$m diameter, mounted at 2.54 mm pitch. The block of tubular cathodes is sliced up into eight separate bars, each 5 mm wide, which are directed perpendicularly to the anode wires. Both the anode wires and the cathode bars are connected to a readout chain comprising a sensitive preamplifier (Philips NE 592 D) mounted directly on the MWPC, an amplifying–discriminating circuit, and time-to-digital converter (CERN Drift Time Recorder). The two coordinates in the window plane, of the point at which the photoionization occurs, are obtained from the anode-wire address and from the measured drift time, respectively. The third coordinate is obtained from the cathode-bar address and is associated with the corresponding anode-wire coordinate by requiring the drift times on the anode and the cathode to be equal.

## 3. Performance requirements

As the $e/\pi$ ratio at SPS $p\bar{p}$ Collider energies might very well be as low as $10^{-4}$ (see fig. 1), we need to achieve an $e/\pi$ rejection power of the RICH counter such that the probability of mistaking a pion for an electron is less than $10^{-4}$. As the absence of a signal in the RICH counter could only lead to an electron being mistaken for a pion, the requirement for the efficiency of the counter is a less critical parameter.

Most electrons detected by the RICH counter are not produced from the decay of heavy flavours but from conversion of $\pi^0$-decay gammas or from Dalitz decay. Such electrons appear in electron–positron pairs, and will be suppressed in the off-line analysis using the $dE/dx$ signals from the two scintillator hodoscopes and from the Si counter array upstream of the magnetic field, as well as by the observation of no hits in the first planes of the vertex detector and the detection of coplanar tracks in the drift chambers downstream from the magnetic field.

## 4. First analysis of a limited data sample

Of the order of 800 000 events were collected with the UA2 RICH setup using a trigger that required signals in both scintillator hodoscopes and in the RICH counter, and at least 1 GeV transverse energy deposited in the electromagnetic calorimeter. All signals from the RICH counter and from the whole of the UA2 detector were recorded for each event. A preliminary analysis of a limited event-sample has been performed as follows.

For each event the signals in the UA2 drift chambers were used to reconstruct the charged-particle trajectories going through the RICH counter. If any such trajectory was found to traverse the $20 \times 20$ cm$^2$ active area of the RICH photon detector, all hits registered by this detector within an area of $8 \times 5.5$ cm$^2$ around the track were considered as being caused by the charged-particle ionization in the photon detector gas. Such hits were disregarded in the subsequent analysis.

### 4.1. Cherenkov angular resolution

From the information on the direction of the charged-particle track through the RICH counter, an

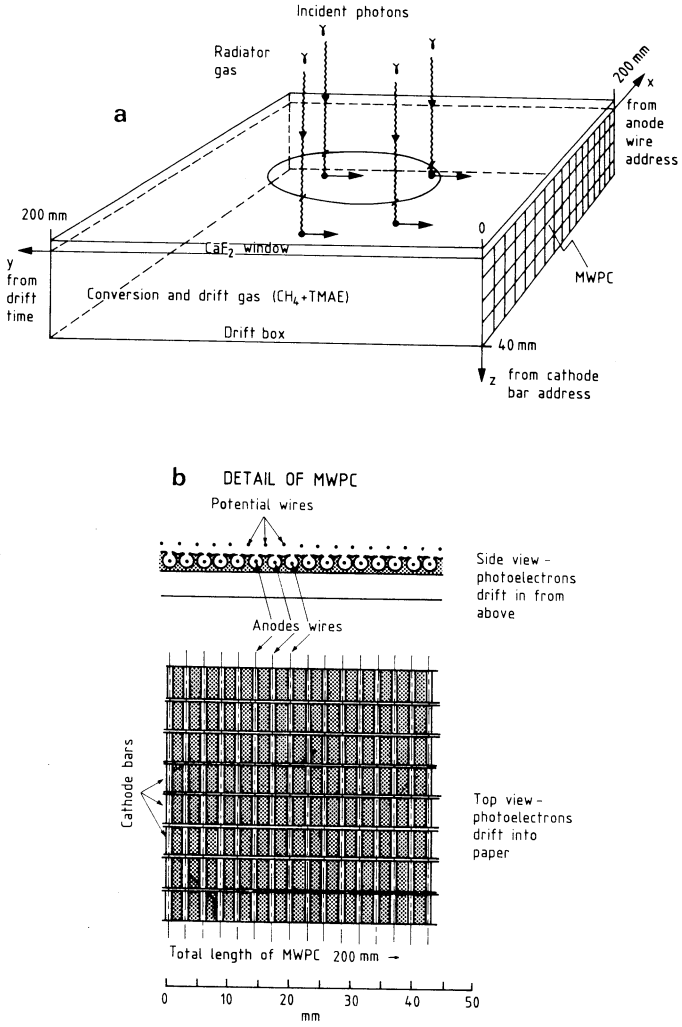


Fig. 4. (a) Schematic drawing of the single-photon position detector showing the $200 \times 200$ mm$^2$ $CaF_2$ window, the 40 mm deep photoionization and electron-drift volume, and the MWPC with the direction of the anode wires and cathode bars indicated. (b) Drawing of the structure of the MWPC in two projections.

expected Cherenkov-ring centre was reconstructed in the photon detector image-plane. For each hit recorded in the photon detector, the distance $r$ of the hit from the expected image centre was calculated.

A histogram of this distance $r$ for about 12000 tracks is shown in fig. 5a. There is a broad (fwhm = 17 mm) peak at $r = 24$ mm, corresponding to a Cherenkov angle of $\theta = 40$ mrad ($\theta = r/f$; $f$ = focal length of the mirror = 600 mm) as expected for electrons. This peak is caused by the relatively abundant conversion electrons, which were enhanced in the data by the trigger condition used. The detectors upstream of the RICH counter represent about 10% of a radiation length, and the amount of charged pions with momentum above the

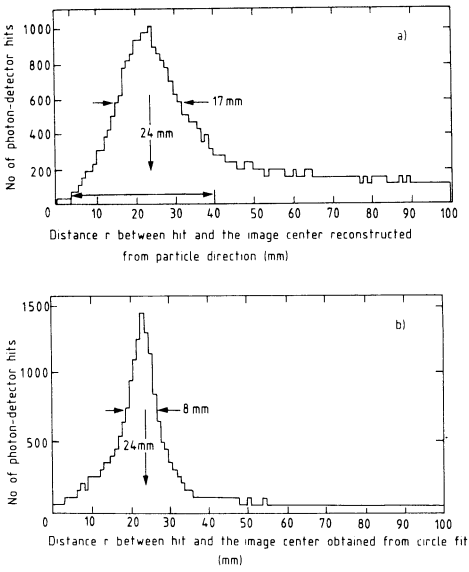


Fig. 5. Plot of the distance $r$ of a photon-detector hit from the expected image centre for 12000 tracks. In (a) the image centre has been reconstructed, for each track, from the optics of the RICH counter, using the measurement of the particle direction in the external drift chambers. In (b) the image centre has been reconstructed as the centre obtained from a circle fit to the photon-detector hits inside the range $5 < r < 40$ mm in (a).

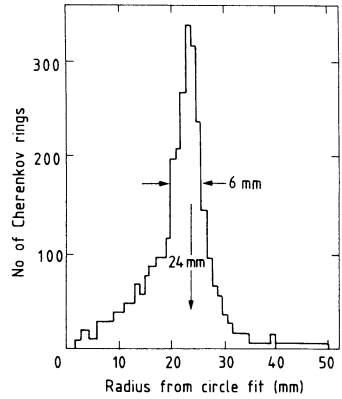


Fig. 6. Distribution of circle radii $R$ obtained from circle fits to the photon-detector hits inside the range $5 < r < 40$ mm in fig. 5a for each track.

threshold of 3.5 GeV/$c$, i.e. above $p_T = 1.75$ GeV/$c$ at 30° to the beam, is therefore negligible compared with the amount of conversion electrons.

The photon detector sits in the fringe field of the UA2 toroidal magnet, and the drift paths of the photoelectrons in the TPC are therefore distorted with regard to the electric drift-field, resulting, to first order, in a displacement of the cherenkov ring by approximately 10 mm. Without including any information on the magnetic field, a first-order correction to this displacement was made in the following way. All hits in the photon detector within 5–40 mm distance from the expected image centre were used to fit a circle. The $r$-distribution was then replotted using, as the predicted image centre, the centre of the fitted circle. The resulting $r$-distribution, displayed in fig. 5b, shows that the peak is still at 24 mm radius but is of significantly smaller width (fwhm = 8 mm). The distribution of radii from the circle fits is displayed in fig. 6, showing a peak at 24 mm of 6 mm fwhm. However, a further decrease in this width can be expected, as a number of corrections still remain to be introduced in the analysis. These corrections include a precise alignment of all detectors, a detailed evaluation of distortions due to the magnetic field, using a measured field map, and compensation of parallax effect in the photon detector using the measured depth coordinate of the point at which the photoionization occurred.

### 4.2. Efficiency

For each circle-fit with radius inside a range $18 < R < 27$ mm, the number $N$ of hits was counted. Fig. 7 shows a frequency distribution for $N$ with normalized Poisson curves superimposed. The curve with a mean value of 4.5 seems to represent the data best. With a radiator length of 60 cm and a Cherenkov angle of $\theta = 40$ mrad, this implies an $N_0$ value of

$$N_0 = \frac{N}{L}\sin^{-2}\theta = 47\ \mathrm{cm}^{-1}.$$

In view of the large wavelength region, 145–230 nm, over which the photon detector is expected to be sensitive this $N_0$ value is lower than anticipated. It is also lower than $N_0$ values obtained in the earlier measurements made in a test beam with the same RICH counter. One possible reason for the low $N_0$ value is that the surface of either the mirror or the window may have been contaminated, thereby reducing the wavelength region of detector sensitivity. In future we intend to verify this point by measuring the mirror reflectivity and the window transparency in the VUV, using a monochromator.

For an event sample having a Poisson-distributed hit frequency with a mean of 4.5, the probability of having two hits or less is 17%. Consequently, if three hits or more will be needed for reliable identification of an

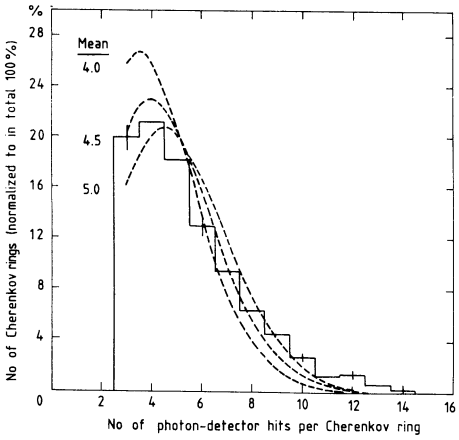


Fig. 7. Frequency distribution of photon-detector hits per fitted Cherenkov ring. Note, that the fit demands at least three hits. The three dashed curves correspond to Poisson curves with mean values of 4, 4.5, and 5, respectively. All distributions are normalized so that the total number of events is 100%. Some representative error bars are shown.

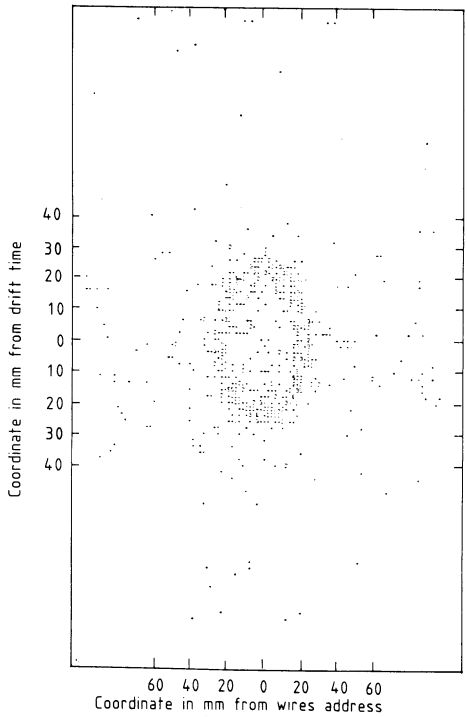


Fig. 8. Accumulated $x-y$ plot of photon-detector hits from 100 conversion-electrons. For each image the expected image-centre has been moved to the centre of the plot. Note the difference in scale of the two axes.

electron, this will imply a contribution of 17% to the detection inefficiency.

The above analysis was repeated for a sample of track pairs, which had been selected as being due to conversion electrons on the basis of the pulse-height information in the scintillator hodoscope and the criteria of track coplanarity downstream from the magnetic field. Because of this preselection, the statistics of this sample was greatly reduced. The results of the analysis of the preselected conversion-electron sample were, however, compatible with the results obtained with the nonpreselected sample. In fig. 8 are shown the accumulated photon-detector images in the window plane from 100 selected conversion-electrons. Each image has been shifted so that the expected image-centre falls on the mid-point of the plot.

### 4.3. Electron-to-pion rejection

A pion with momentum below threshold ($< 3.5$ GeV/$c$) can be wrongly identified as an electron if background signals appear within the fiducial ring-area, around the expected image centre defined by the pion track.

It was observed in the data that a limited fraction of the events contained several noise signals spread over the whole photon-detector area. The origin of this kind of background is not fully understood. However, in order to identify these disturbed events a check was made to see if all detected hits in an event could be assigned to either a charged particle or to a Cherenkov ring. If more than two hits were found unassigned, the event was rejected. This removed on the average 15% of the events.

In order to determine to what extent, in the remaining event sample, other spurious background signals could lead to a pion being wrongly identified as an electron, a large number of faked "image centres" were Monte-Carlo-generated in real data, and fiducial ring-areas were constructed around these generated centres. Cherenkov photon signals originating from other tracks were excluded by disregarding all signals in overlapping fiducial areas. If three or more spurious background signals were found inside the remaining fiducial area, a circle-fit was performed. From hits with $15 < r < 30$ a fitted radius inside $18 < R < 27$ mm was found in about one of 10000 generated events, indicating, already at

this preliminary stage of the data analysis, that an $e/\pi$ rejection of the order $10^{-4}$ is achievable with the RICH counter.

## 5. Summary and outlook

We have reported on some indicative results obtained from a first analysis of a limited data sample. The results are: (i) with the RICH counter the electron Cherenkov ring can be clearly observed with the expected ring radius of 24 mm and with a width not larger than 6 mm; (ii) the $N_0$ of the RICH is found to be of the order of 47 $cm^{-1}$; and (iii) the $e/\pi$ rejection of the RICH obtained so far is of the order of $10^{-4}$. There are several additional steps to be taken in the analysis (alignment of detectors, use of magnetic field-map data, involvement of depth coordinate readout), from which a significant improvement in the Cherenkov angular resolution – and therefore in the rejection – can be expected. Measurements of the VUV transparency of the window and the VUV reflectivity of the mirror will be done in order to seek an explanation for the unexpectedly low $N_0$ value found. We are also planning to verify, by direct measurement, the $e/\pi$ rejection of the RICH at very high statistics in a $\pi^-$ beam from the CERN PS by independent identification of the $\pi$ using two threshold Cherenkov counters, of about 5 m length each, in the incident beam.

From the results obtained we conclude that the goal of our experiment, which is to measure the $e/\pi$ ratio at SPS $p\bar{p}$ energies, should be within reach.

## Acknowledgements

We express our gratitude to the UA2 Collaboration for having put the UA2 detector and the associated software at our disposal. In particular we wish to thank P. Darriulat, O. Gildemeister, J.R. Hansen and A. Sigrist of UA2 for their very helpful cooperation. The RICH counter was designed and built in collaboration with the EP Technical Assistance Group at CERN and the GWI Technical Workshop of the University of Uppsala. We thank especially D. Bérnier, R. Bouhot, P. Dam, G. Muratori, C. Rivoiron and G. Vismara at CERN, and L.O. Andersson, E. Lindholm, L. Lindqvist and L. Mattsson at GWI, for their crucial technical assistance with the project. The active participation of A. Litke in the conceptual stage of this experiment is gratefullly acknowledged.

## References

[1] F.W. Büsser et al. (CCRS Collab.), Nucl. Phys. B113 (1976) 189;
M. Barone et al. (ACHMNR Collab.), Nucl. Phys. B132 (1978) 29;
M. Basile et al. (CBF Collab.), Nuovo Cimento 65A (1981) 421;
P. Perez et al. (CCZ Collab.), Phys. Lett. 112B (1982) 260;
W.M. Geist et al. (ACCDHW Collab.), Proc. 2nd Moriond Workshop on New Flavours, Les Arcs, 1982 (Editions Frontières, Gif-sur-Yvette, 1982) p. 407.

[2] J. Séguinot and T. Ypsilantis, Nucl. Instr. and Meth. 142 (1977) 377.
T. Ekelöf et al., Phys. Scripta 23 (1981) 718;
E. Barrelet et al., Nucl. Instr. and Meth. 200 (1982) 219;
L.O. Eek et al., IEEE Trans. Nucl. Sci. NS-31 (1984) 949;
T. Ekelöf, Proc. SLAC Summer Institute on Particle Physics, Stanford, 1984, ed., P.M. McDonough (Nat. Tech. Info. Service, Springfield, VA, 1985) p. 244.

[3] B. Mansoulié, Proc. 3rd Moriond Workshop on $p\bar{p}$ Physics and the W. Discovery, La Plagne, 1983 (Editions Frontières, Gif-sur-Yvette, 1983) p. 609;
M. Dialinas et al., Orsay report LAL-RT/83-14 (1983);
A. Beer et al., Nucl. Instr. and Meth. 224 (1984) 360;
C. Conta et al. Nucl. Instr. and Meth. 224 (1984) 65;
K. Borer et al., Nucl. Instr. and Meth. 227 (1984) 29.